AN ABSTRACT OF THE THESIS OF

Eric Edwalds for the degree of Master of Science in Atmospheric Sciences presented on September 1, 1987.

Title: A Numerical Study of Sulfur and Nitrogen Scavenging in a Mesoscale Rainband Observed in the GALE Experiment

Abstract approved: Redacted for Privacy
Steven A. Rutledge

A two-dimensional kinematic cloud chemistry model has been employed to study the scavenging of sulfur and nitrogen compounds that occurred in a mesoscale rainband observed during the GALE (Genisis of Atlantic Lows Experiment) project on 6 March 1986.

The results of the model simulations indicate that precipitation was generated in a manner similar to the seeder-feeder mechanism observed in wide cold-frontal rainbands. Direct comparisons of model results to *in situ* observations were made. Cloudwater contents predicted by the model (.01-.1g kg^{-1}) were significantly less than measured values (.5-1.2g kg^{-1}). However, model-generated precipitation rates were in good agreement with surface measurements.

In-solution oxidation of SO_2, primarily by H_2O_2, contributed up to 67% of the sulfate deposited. The sulfate concentrations predicted by the model corresponded well to the available measurements. Nitrate deposition was only affected by microphysical processes as a result of insignificant dissolution of

PAN and the lack of initial gas-phase HNO_3. The lack of an in-cloud reaction pathway of NO_x for nitrate production in the model resulted in underprediction of nitrate concentrations. Discrepancies between model results and available observations are discussed.

A Numerical Study of Sulfur and Nitrogen Scavenging in a Mesoscale Rainband Observed in the GALE Experiment

by

Eric Edwalds

A THESIS

submitted to

Oregon State University

in partial fulfillment of
the requirements for the
degree of

Master of Science

Completed September 1, 1987

Commencement June, 1988

APPROVED:

Redacted for Privacy

Professor of Atmospheric Sciences in charge of major

Redacted for Privacy

Chairman of Department of Atmospheric Sciences

Redacted for Privacy

Dean of Graduate School

Date thesis is presented September 1, 1987

Presented by Eric Edwalds

ACKNOWLEDGEMENTS

I would like to thank my Major Professor, Dr. Steven A. Rutledge, for his help and guidance given to me during the preparation of this thesis. Also I appreciate the comments by members of my thesis committee Drs. Michael Schuyler, Jeffrey Barnes, and Terence Brown. Special thanks are in order for Professor Dean Hegg of the University of Wahington for his help in the chemical analysis and data preparation.

I would like to thank Dean A. Vickers for his assistance in running the simulations and insights in regards to the model computations.

This research was supported by the Electric Power Research Institute and the University of Washington under Contract No. 264335. Computing resources were provided by the National Center for Atmospheric Resaerch.

TABLE OF CONTENTS

		Page
1.	INTRODUCTION	1
	1.1 General Background	1
	1.2 Thesis Organization	4
2.	THE GALE PROJECT	6
	2.1 Experimental Purpose	6
	2.2 Experimental Design	8
	2.3 Synoptic Discussion	10
3.	MODEL DESCRIPTION	14
	3.1 Cloud Physics Component	14
	3.1.1 Size distributions	15
	3.1.2 Continuity equations	17
	3.2 Chemistry Component	18
4.	MODEL INPUTS	23
	4.1 Kinematic Structure	23
	4.2 Thermodynamic Structure	25
	4.3 Chemistry Inputs	27
5.	DISCUSSION OF BACKGROUND SIMULATION	30
	5.1 Results From the Cloud Component of the Model	30
	5.2 Results From the Chemical Component of the Model	36
	5.2.1 Sulfate, nitrate, and hydrogen peroxide	39
	5.2.2 Cloud acid generation	52
	5.2.3 Deposition and transport	54
6.	SENSITIVITY STUDIES AND COMPARISONS WITH OBSERVATIONS	60
	6.1 Sensitivity Studies	60
	6.2 Comparisons of Model Results to Observations	89
	6.2.1 Microphysical comparisons	89
	6.2.2 Chemistry comparisons	91
7.	CONCLUSIONS	97
	7.1 Conclusions and Model Evaluation	97
	7.2 Suggestions for Further Research	98
	REFERENCES	100

LIST OF FIGURES

		Page
2.1	Schematic depiction of the types of mesoscale rainbands observed in extratropical cyclones. (Adapted from Rutledge, 1983.)	7
2.2	GALE special surface-based observational facilities. (Adapted from GALE Experiment Design, 1985).	9
2.3	GALE Doppler radar areal coverage. (Adapted from GALE Experiment Design, 1985).	11
2.4	NWS surface analysis for 1800 GMT on 6 March 1986. Black areas are composite radar echoes from nine WSR-57 radars. (Adapted from Hobbs, 1987).	12
3.1	Schematic showing the cloud model variables and microphysical processes for the 2-D kinematic model. (Adapted from Rutledge *et al.* 1986).	16
3.2	Schematic showing the sulfate scavenging processes for the 2-D kinematic model. (Adapted from Rutledge *et al.* 1986).	20
3.3	Schematic showing the nitrate scavenging processes for the 2-D kinematic model. (Adapted from Rutledge *et al.* 1986).	21
4.1	Horizontal band-relative airflow (m s^{-1}), shaded area corresponds to left-to-right motion.	24
4.2	Vertical airflow (cm s^{-1}), dark shading corresponds to downdrafts, light shading areas are w=0.	24
4.3	Reflectivity in dBZ, dashed box indicates model domain.	24
4.4	Sounding from Wilmington N.C. at 1730 GMT on 6 March 1986.	26
4.5	Initial profile of H_2O_2. Units are 10^{-9}g g^{-1}.	29

		Page
4.6	Initial profile of PAN. Units are 10^{-10}g g^{-1}.	29
5.1	Equilibrium field for the cloudwater mixing ratio. Units are g kg^{-1}.	31
5.2	Equilibrium field for the snow mixing ratio. Units are g kg^{-1}.	32
5.3	Equilibrium field for the rain mixing ratio. Units are g kg^{-1}.	33
5.4	Precipitation rate. Units are mm hr^{-1}.	37
5.5	Model calculated reflectivity (dBZ). Values greater than 30 are shaded.	38
5.6	Mixing ratio of particulate sulfate for the background simulation. Units are 10^{-9} g g^{-1}.	40
5.7	Mixing ratio of particulate nitrate for the background simulation. Units are 10^{-10} g g^{-1}.	41
5.8	Mixing ratio of gaseous H_2O_2 for the background simulation. Units are 10^{-9} g g^{-1}.	42
5.9	Mixing ratio of sulfate-in-cloudwater for the background simulation. Units are 10^{-9} g g^{-1}.	43
5.10	Mixing ratio of nitrate-in-cloudwater for the background simulation. Units are 10^{-10} g g^{-1}.	44
5.11	Mixing ratio of H_2O_2-in-cloudwater for the background simulation. Units are 10^{-9} g g^{-1}.	45
5.12	Mixing ratio of sulfate-in-snow for the background simulation. Units are 10^{-9} g g^{-1}.	46

		Page
5.13	Mixing ratio of nitrate-in-snow for the background simulation. Units are 10^{-10} g g^{-1}.	47
5.14	Mixing ratio of H_2O_2-in-snow for the background simulation. Units are 10^{-9} g g^{-1}.	48
5.15	Mixing ratio of sulfate-in-rain for the background simulation. Units are 10^{-9} g g^{-1}.	49
5.16	Mixing ratio of nitrate-in-rain for the background simulation. Units are 10^{-10} g g^{-1}.	50
5.17	Mixing ratio of H_2O_2-in-rain for the background simulation. Units are 10^{-9} g g^{-1}.	51
5.18	pH of liquid hydrometeors for the background simulation. Shaded areas are pH greater than 4.5.	53
5.19	Mixing ratio of SO_2 for the background simulation. Units are 10^{-9} g g^{-1}.	55
5.20	Mixing ratio of PAN for the background simulation. Units are 10^{-10} g g^{-1}.	56
5.21	Wet deposition rates for sulfate (SUL), nitrate (NIT), and H_2O_2 (PER) with the precipitation rate (RR) included. Units for sulfate, g hr^{-1} cm^{-1}(transverse to the direction of propagation); nitrate and H_2O_2,10^{-1} g hr^{-1} cm^{-1}. Precipitation rate is in cm hr^{-1}.	57
5.22	Vertical profiles of chemical species at initialization (solid line) and at equilibrium (dashed line) for the background simulation, a) SO_2, b) particulate sulfate, c) particulate nitrate, and d) H_2O_2.Units are 10^{-9} g g^{-1}.	59
6.1	Mixing ratio of particulate sulfate for the case 2 simulation. Units are 10^{-9}g g^{-1}.	62
6.2	Mixing ratio of SO_2 for the case 2 simulation. Units are 10^{-9}g g^{-1}.	63

		Page
6.3	Mixing ratio of sulfate-in-cloudwater for the case 2 simulation. Units are 10^{-9}g g^{-1}.	64
6.4	Mixing ratio of sulfate-in-snow for the case 2 simulation. Units are 10^{-9}g g^{-1}.	66
6.5	Mixing ratio of sulfate-in-rain for the case 2 simulation. Units are 10^{-9}g g^{-1}.	67
6.6	Mixing ratio of particulate sulfate for the case 3 simulation. Units are 10^{-9}g g^{-1}.	68
6.7	Mixing ratio of SO_2 for the case 3 simulation. Units are 10^{-9}g g^{-1}.	69
6.8	pH for the case 3 simulation. Areas greater than 4.5 are shaded.	70
6.9	Mixing ratio of sulfate-in-cloudwater for the case 3 simulation. Units are 10^{-9}g g^{-1}.	71
6.10	Mixing ratio of sulfate-in-snow for the case 3 simulation. Units are 10^{-9}g g^{-1}.	72
6.11	Mixing ratio of sulfate-in-rain for the case 3 simulation. Units are 10^{-9}g g^{-1}.	73
6.12	Mixing ratio of particulate sulfate for the case 4 simulation. Units are 10^{-9}g g^{-1}.	75
6.13	Mixing ratio of SO_2 for the case 4 simulation. Units are 10^{-9}g g^{-1}.	76
6.14	Mixing ratio of sulfate-in-cloudwater for the case 4 simulation. Units are 10^{-9}g g^{-1}.	77
6.15	Mixing ratio of sulfate-in-snow for the case 4 simulation. Units are 10^{-9}g g^{-1}.	78

Page

6.16 Mixing ratio of sulfate-in-rain for the case 4 simulation. Units are 10^{-9}g g^{-1}. 79

6.17 Nucleation scavenging in the background simulation. Units are 10^{-12}g $g^{-1}s^{-1}$. 81

6.18 Mixing ratio of particulate sulfate for the case 5 simulation. Units are 10^{-9}g g^{-1}. 82

6.19 Mixing ratio of SO_2 for the case 5 simulation. Units are 10^{-9}g g^{-1}. 83

6.20 Mixing ratio of sulfate-in-cloudwater for the case 5 simulation. Units are 10^{-9}g g^{-1}. 84

6.21 Mixing ratio of sulfate-in-snow for the case 5 simulation. Units are 10^{-9}g g^{-1}. 85

6.22 Mixing ratio of sulfate-in-rain for the case 5 simulation. Units are 10^{-9}g g^{-1}. 86

6.23 Sulfate deposition rates for the 5 simulations. Units are g $cm^{-1}hr^{-1}$. 88

6.24 Comparison of *in situ* measurements of SO_2 to model results. Solid line is the initial SO_2 profile, thinly dashed line is model domain average, broadly dashed line is the 10 km average. Measurements are denoted with circles and error bars. Units are 10^{-9}g g^{-1}. 92

6.25 Comparison of *in situ* measurements of sulfate to model results. Solid line is the initial sulfate profile, thinly dashed line is model domain average, broadly dashed line is the 10 km average. Measurements are denoted with circles and error bars. Units are 10^{-9}g g^{-1}. 94

6.26 Comparison of *in situ* measurements of nitrate to model results. Solid line is the initial nitrate profile, thinly dashed line is model domain average, broadly dashed line is the 10 km average. Measurements are denoted with circles and error bars. Units are 10^{-9}g g^{-1}. 95

LIST OF TABLES

		Page
4.1	Values of $q_i(0)$ and H_i for the chemical species included in the model.	28
5.1	Comparison between model derived hydrometeor production terms.	35
6.1	Model simulations discussed in this paper.	61

A NUMERICAL STUDY OF SULFUR AND NITROGEN SCAVENGING IN A MESOSCALE RAINBAND OBSERVED IN THE GALE EXPERIMENT

1. INTRODUCTION

1.1 General Background

Acid deposition, primarily from sulfates and nitrates, continues to be a problem in many parts of the world, especially in (and downwind of) the industrial regions of Canada, Europe, and the United States. The need to decrease these deposition amounts is made obvious through evaluation of the damage already done to the environment. Many lakes in Canada, Sweden, and the Northeast U.S. can no longer support aquatic life resulting from increased acidity levels of the water. The famed Black Forest of Germany has experienced dramatic tree death as a result of acid deposition from the highly industrialized Ruhr Valley. However, before any concrete steps to alleviate these problems are made, the mechanisms of acid deposition must be understood in order that the preventive measures taken are effective. For example, there is evidence that the amount of sulfuric acid produced from oxidation of sulfur dioxide is dependent on the amount of oxidants present in the atmosphere, not the amount of sulfur dioxide (Chamberlain *et al.* 1985). Hence a reduction of sulfur dioxide emitted by coal-fired power plants (e.g. through installation of efficient stack scrubbers) may not necessarily reduce the total acid deposited.

Both wet and dry deposition are important in terms of total acid deposited, but wet deposition (more commonly known as "acid rain") appears to have more harmful effects. Wet deposition results when pollutants are

incorporated into clouds and fall to the surface in precipitation, either in the form of liquid drops or ice particles. Generally dry deposition, the fallout of pollutants without the aid of clouds, remains relatively inert to its environment until there is a precipitation event. The pollutants then make their way through the ecosystem via groundwater and runoff causing varying (and largely unquantified) amounts of damage. (Acidified fogs, which are neither truly wet nor dry deposition, have been seen to be the most acidic deposition event and can be very harmful to forests, buildings, etc...). It is not yet clear how much of the wet deposition problem results from the incorporation of acids (and acid precursors) present from dry deposition periods and how much results from the acidic precipitation itself.

It is well known that clouds and precipitation are very important in the removal and redistribution of atmospheric pollutants such as sulfur dioxide, sulfate, nitric acid and various forms of nitrate. Field studies have quantified pollutant concentrations in air, clouds, and precipitation for many different meteorological situations (e.g. Huebert *et al.*1980,1983; Radke *et al.*1980; Daum *et al.*1984; Hegg *et al.*1984a; Sperber and Hameed 1986). Still, the precise physical mechanisms that affect pollutants in clouds and precipitating systems have remained more elusive to researchers. Field studies alone are insufficient because they cannot control the parameters necessary to elucidate the dominant physical processes. Laboratory studies are valuable, especially for physiochemical studies (e.g. Martin and Damschen 1981; Holdren *et al.* 1984; Chang 1984), but they lack the ability to accurately simulate atmospheric conditions. Numerical models, formed by the merger of cloud and chemical models, used in conjunction with field and laboratory work, have proven to be

effective tools for understanding complex pollutant, cloud, and precipitation interactions (e.g.Scott 1978,1982; Levine and Schwartz 1982; Hegg *et al.* 1984b,1986; Tremblay and Leighton 1984,1985; Lee and Shannon 1985; Chaummerliac *et al.* 1987).

Tremblay and Leighton (1985) employed a time variant, three-dimensional model with parameterized microphysics to explore the spatial and temporal redistribution of sulfur and nitrogen compounds in shallow cumuli. More recently, Chaummerliac *et al.* (1987) investigated sulfur scavenging differences between orographically induced continental and maritime clouds using quasi-spectral microphysics. They found significant differences between the cloud types: continental clouds were more efficient at in-cloud scavenging but precipitating maritime clouds removed more particles. They emphasized the need for models to include cloud condensation nuclei and cloud droplet spectra to more realistically determine the scavenging capabilities of clouds and precipitation. In a related vein, Barrie (1985) mentions that bulk scavenging coefficients should be used cautiously because of the varied efficiencies observed. More importantly, some precipitating cloud systems may have high precipitation efficiencies (defined as the ratio of precipitation amounts to the in-cloud condensation amounts) but relatively low pollutant removal efficiencies, e.g. a cloud system dominated by growth by vapor deposition such that little to no liquid water is available for nucleation scavenging and in-solution sulfate production.

Most of the modeling studies undertaken, while informative, are not necessarily realistic from a microphysical or synoptic standpoint. The work of Hegg *et al.* (1984b,1986) has studied the removal of sulfur and nitrogen

species in different types of mesoscale rainbands associated with extratropical cyclonic storms. In their work, chemistry parameterizations were coupled with a kinematic cloud model developed by Rutledge and Hobbs (1983,1984) as described in Rutledge *et al.* (1986). This model has the advantage of more detailed microphysics compared to previous studies, and relies on validated field data for various model inputs. The present study employs the cloud chemistry model of Rutledge *et al.* (1986) to examine pollutant removal in a mesoscale rainband associated with an east coast winter cyclonic storm. This study is unique in the sense that simultaneous *in situ* observations of the cloud microphysics, aerosols and trace gas concentrations were made in conjunction with dual-Doppler radar observations of the rainband airflow field. These observations allow validation of the model predicted chemical and microphysical fields. It is the first application of this model to storms outside the U.S. Pacific Northwest.

1.2 Thesis Organization

The data set used here was obtained from the Genesis of Atlantic Lows Experiment (GALE). Hence a description of the GALE project will be given in Chapter 2. The remainder of the thesis will be organized as follows. Chapter 3 will describe the model used in this study, giving brief descriptions of both the cloud and chemistry components. Chapter 4 will describe model inputs such as the thermodynamic and kinematic fields as well as chemical parameters. Chapter 5 will discuss a background simulation and Chapter 6 will focus on the sensitivity studies and comparisons of model outputs with available field measurements. The focus of this work involves interpreting the model results

via sensitivity studies to determine the dominant pollutant removal mechanisms present, and comparing them with observations. By doing so a more thorough understanding of the physical and chemical processes in this rainband can be acheived. In Chapter 7 the model results will be summarized and suggestions for future research will be given.

2. THE GALE PROJECT

2.1 Experimental Purpose

GALE was designed as a comprehensive study of winter weather systems along the eastern seaboard of the United States. During this season rapid cyclogenesis can occur east of the Appalachian mountains along the mid-Atlantic seaboard. This phenomenon is poorly predicted by current numerical forecasting models as a result of our relatively poor understanding of mesoscale, boundary layer, and ocean-atmosphere energy exchanges with synoptic-scale weather systems. As such, the primary purpose of the experiment was to collect as complete a data base as possible of mesoscale and synoptic scale measurements that could be used in future diagnostic and numerical modeling studies. A piggyback experiment in GALE was a special experiment conducted by the University of Washington to collect airborne *in situ* chemistry data. In conjunction with this experiment, a special attempt was made to collect simultaneous chemistry and Doppler data to allow a study with the Rutledge *et al.* (1986) model. This thesis describes the results of this modeling study.

The CYCLES (CYCLonic Extratropical Storms) project carried out by the University of Washington has described the mesoscale structure of cyclonic storms in the Pacific Northwest via extensive mesoscale measurements (e.g., Hobbs *et al.*, 1980; Herzegh and Hobbs, 1980, 1981; Houze *et al.*, 1981). Fig. 2.1 shows an idealized classification of the various types of rainbands that have been identified in extratropical cyclones. Similar rainbands have been observed in the United Kingdom as well (e.g., Browning *et al.*, 1974). A secondary objective of GALE was, through the collection and analyzation of

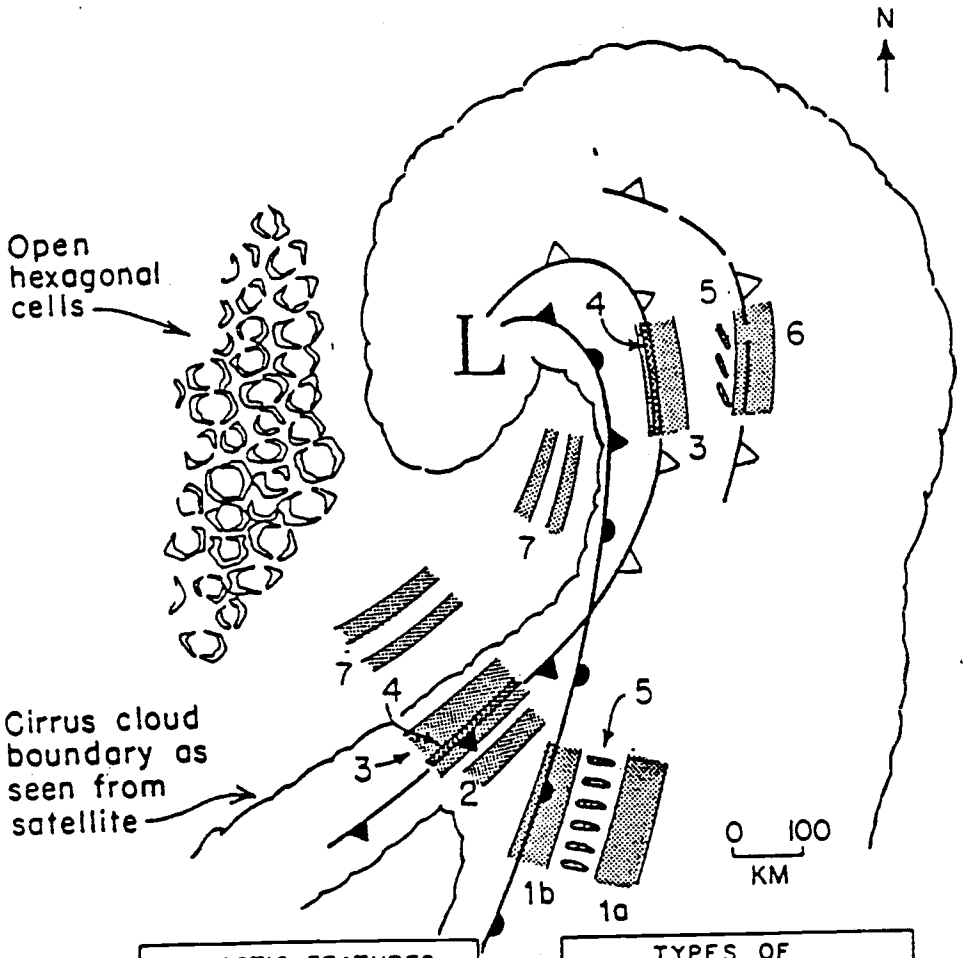

SYNOPTIC FEATURES	
L	SURFACE LOW-PRESSURE CENTER
	SURFACE COLD FRONT
	SURFACE WARM FRONT
	SURFACE WARM OCCLUDED FRONT
	COLD FRONT ALOFT
	PREFRONTAL COLD SURGE ALOFT

TYPES OF MESOSCALE RAINBANDS
1. WARM-FRONTAL
2. WARM-SECTOR
3. WIDE COLD-FRONTAL
4. NARROW COLD-FRONTAL
5. WAVE-LIKE
6. PREFRONTAL COLD SURGE
7. POSTFRONTAL

Fig. 2.1 Schematic depiction of the types of mesoscale rainbands observed in extratropical cyclones. (Adapted from Rutledge, 1983).

mesoscale data sets, to determine if east coast cyclones exhibit the same type of structures as their west coast counterparts.

The seven rainband types listed in Fig. 2.1 are warm-frontal, warm-sector, wide cold-frontal, narrow cold-frontal, wave-like, prefrontal cold surge, and postfrontal. There are basically two types of precipitation mechanisms present. In warm-frontal, wide cold-frontal, and to a lesser extent in prefrontal cold surge rainbands, precipitation is formed by the release of potential instability in the form of generating cells above a region of mesoscale lifting (~10-100 cm s^{-1}). Hydrometeor growth occurs primarily through vapor deposition, light riming and aggregation. This is the "seeder-feeder" mechanism described by Herzegh and Hobbs (1980), Matejka *et al.* (1980), and Houze *et al.* (1981) among others.

Warm-sector and narrow cold-frontal rainbands are driven by surface convergence which produces moderate to vigorous convection. Precipitation growth is characterized by heavy riming resulting from high liquid water contents (~1 g m^{-3}) and heavy graupel showers are not uncommon (Houze and Hobbs, 1982). Convective processes are also responsible for precipitation development in postfrontal and wave-like rainbands.

2.2 Experimental Design

GALE was centered at Cape Hatteras, North Carolina. In order to collect the needed data a surface mesonet, shown in Fig. 2.2, was created. Some of the mesonet features included 5 Doppler radars and 50 PAM II (Portable Automated Mesonet) stations. The PAM stations provided high time resolution (5-minute average values) of the standard meteorological variables of

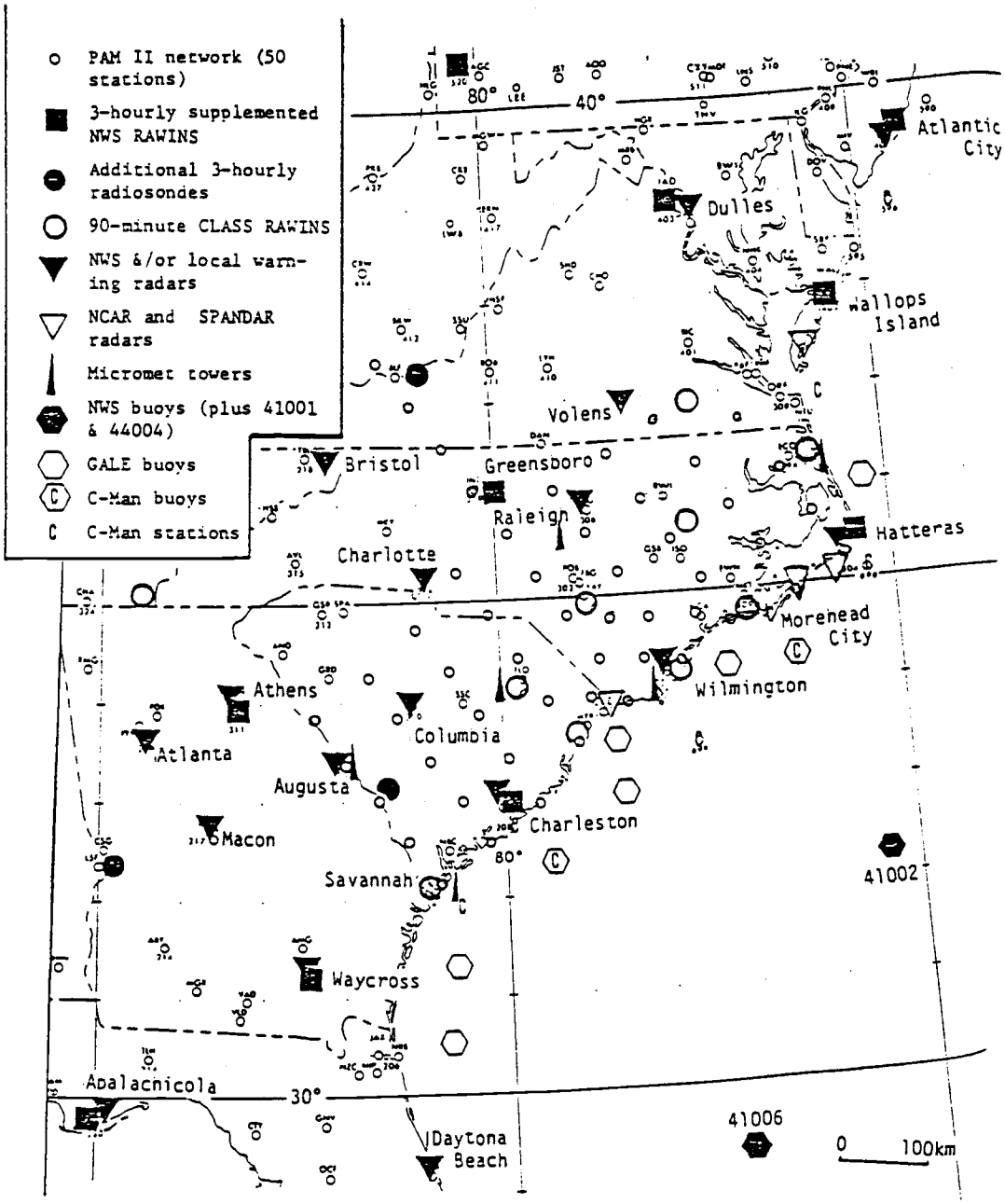

Fig. 2.2 GALE special surface-based observational facilities. (Adapted from GALE Experiment Design, 1985).

pressure, temperature, dewpoint, wind velocity and precipitation. The Doppler radars were used to determine the airflow and dynamics in the precipitating systems. The areas of single and dual-Doppler radar coverage are given in Fig. 2.3. Along with these surface observations 10 research aircraft were available for *in situ* measurements. The University of Washington's C-131A aircraft collected all of the chemistry data and most of the microphysical data used in this study.

The GALE observation period lasted from 15 January - 15 March 1986. The data for this study was collected on 6 March 1986 during the period from 1300 to 2300 GMT.

2.3 Synoptic Discussion

The National Weather Service (NWS) surface analysis at 1800 GMT 6 March 1986, shown in Fig. 2.4, showed a low pressure center of 993 mb over western New York state with the corresponding cold front extending through the Carolinas into the Gulf of Mexico. Approximately 50 km to the east of the cold front a pressure trough, corresponding to an upper-level cold front, was analyzed from Virginia to Florida. The passage of the first trough was characterized by a cyclonic wind shift and a pressure check whereas the passage of the surface cold front produced a greater cyclonic wind shift, a drop in dewpoint, and a pressure increase. Precipitation associated with this system, as observed from NWS WSR-57 radars, extended from New Jersey into South Carolina. Warm southerly airflow preceded the upper-level cold front supplying the requisite moisture for precipitation. The rainband modeled in this study, labelled R1 in Fig. 2.4, generated its precipitation in the convergent zone

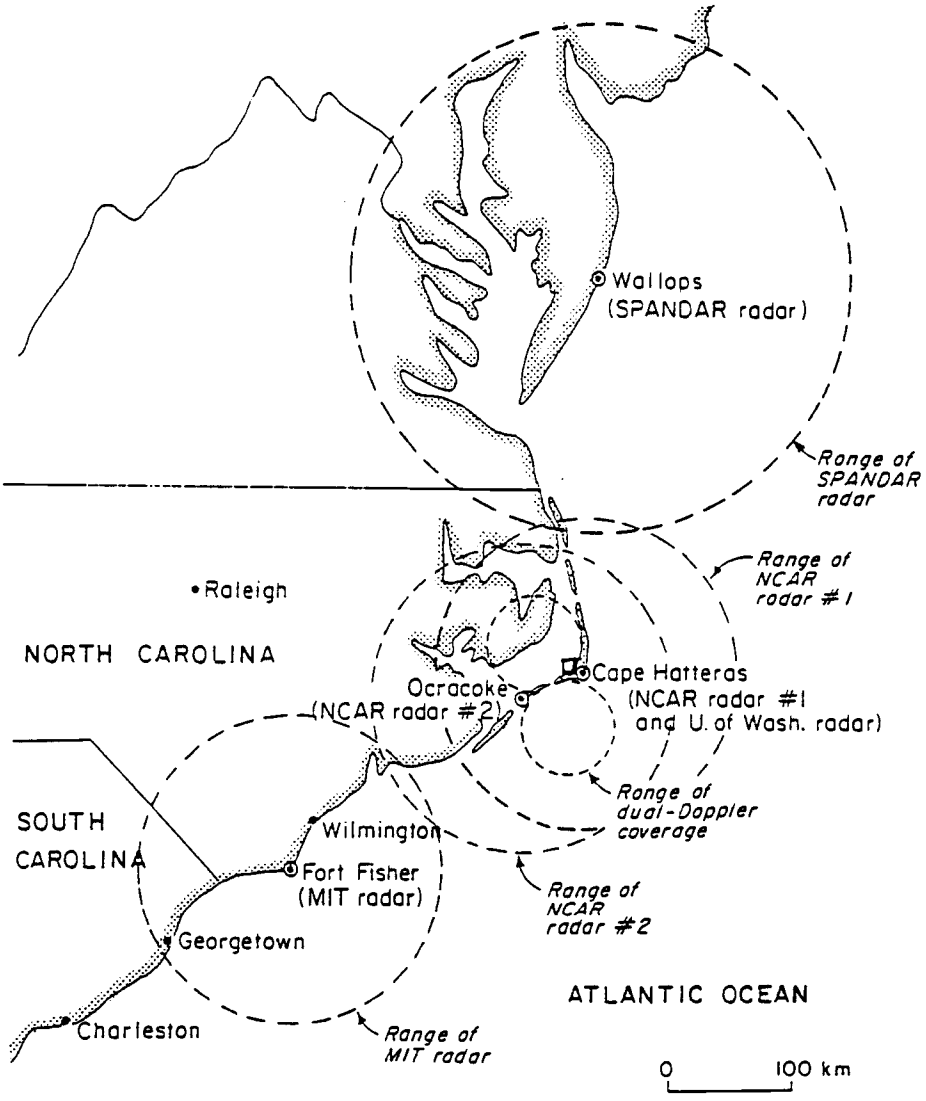

Fig. 2.3 GALE Doppler radar areal coverage. (Adapted from GALE Experiment Design, 1985).

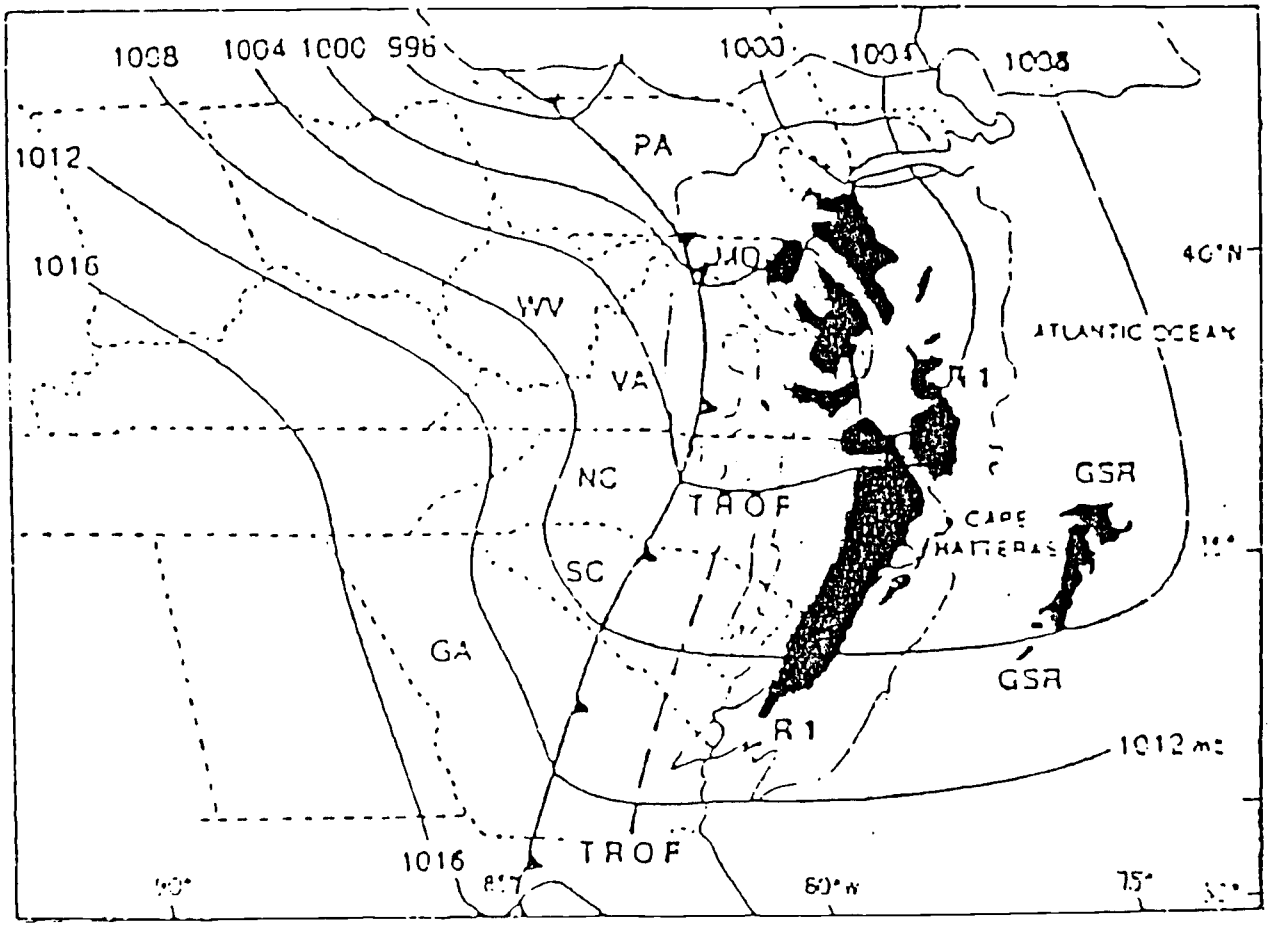

Fig. 2.4 NWS surface analysis for 1800 GMT on 6 March 1986. Black areas are composite radar echoes from nine WSR-57 radars. (Adapted from Hobbs, 1987).

associated with the upper-level cold front and the southerly airflow.

3. MODEL DESCRIPTION

As previously mentioned, the cloud-chemistry model employed in this study has been discussed in detail by Rutledge *et al.* (1986). The reader is referred to that source for a detailed explanation of the model. A perfunctory explanation will be given here.

3.1 Cloud Physics Component

The cloud component of this model has been previously discussed by Rutledge and Hobbs (1983,1984). The model is kinematic and diagnostic. Kinematic implies no prediction of the cloud dynamics since the air motion pattern is fixed throughout the integration. Hence the water continuity fields are those in equilibrium with the specified air motion pattern. The air motion pattern consists of horizontal band-relative winds and the corresponding diagnosed vertical motion. Fundamental to this technique is that the air motion pattern is essentially steady-state over the course of the model integration. This is a valid assumption for the case described herein.

In this study we employ a two-dimensional version of the Rutledge and Hobbs model with the x-axis oriented perpendicular to the length of the rainband and z the height coordinate. The grid spacing we used for all simulations was 1 km in the horizontal and 0.4 km in the vertical.

In addition to the airflow field the model requires that the temperature, pressure, and water vapor mixing ratio be specified. These variables were obtained from a pre-band sounding and are assumed to be horizontally homogeneous at the beginning of the model simulation.

The microphysical processes that are included in the model are shown

schematically in Fig. 3.1. They include collection, condensation, deposition, evaporation, freezing, melting, and riming. The output variables are temperature and the mass mixing ratios of water vapor (QV), cloud water (QCW), cloud ice (QCI), snow (QS), rain (QR), and graupel (QG). Water vapor, cloud water, and cloud ice are advected with the airflow but rain, snow and graupel fall relative to the updraft based on their mass-weighted fall speeds. Formulations for the mass-weighted fallspeeds can be found in Rutledge and Hobbs (1983,1984).

3.1.1 Size Distributions

Some of the assumptions made about hydrometeor size distributions are very important in terms of model results. In this study the raindrop size distribution given by Marshall and Palmer (1948) is employed and is expressed as:

$$N_{DR} = N_{0R} \exp(-\lambda_R D_R)\, dD_R \qquad (3.1)$$

where $N_{DR}(m^{-3})$ is the number of raindrops per cubic meter whose diameters lie between D_R and D_R+dD_R, $N_{0R}(8 \times 10^6 m^{-4})$ is the slope intercept value, and $\lambda_R(m^{-1})$ is the distribution slope. The value of λ_R is given by,

$$\lambda_R = \left[\frac{\pi \rho_L N_{0R}}{\rho Q_R} \right]^{0.25} \qquad (3.2)$$

where ρ_L is the density of water and ρ is the air density.

The size distributions for snow and graupel are also inverse exponential distributions and are formulated as for rain but with the subscripts changed to S

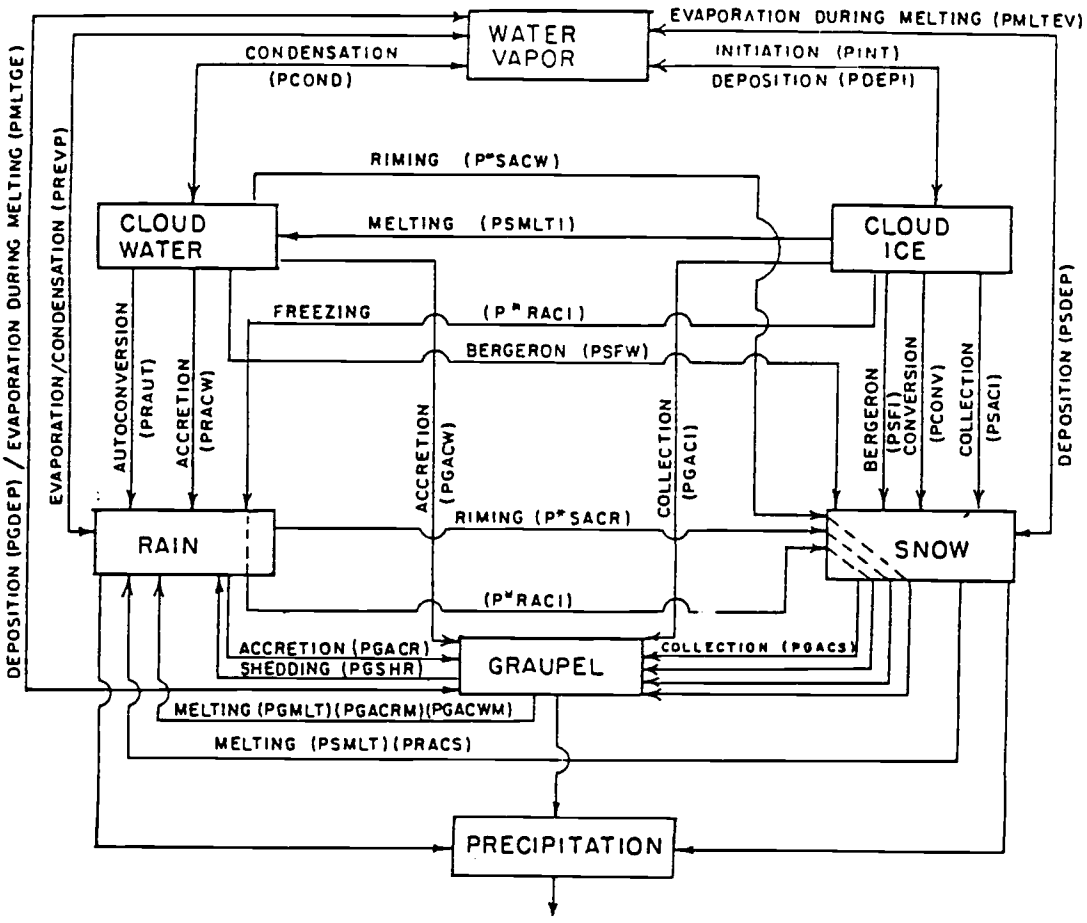

Fig. 3.1 Schematic showing the cloud model variables and microphysical processes for the 2-D kinematic model. (Adapted from Rutledge *et al.* 1986).

and G respectively. Specifically,

$$N_{DS} = N_{0S} \exp(-\lambda_S D_S)\, dD_S \tag{3.3}$$

and,

$$N_{DG} = N_{0G} \exp(-\lambda_G D_G)\, dD_G \tag{3.4}$$

The distribution slopes λ_S and λ_G are of the same form as that for rain. The slope intercept values for snow and graupel are equivalent in this study and given by

$$N_{0S} = N_{0G} = 14 \times 10^6\ m^{-4}. \tag{3.5}$$

3.1.2 Continuity Equations

The two-dimensional continuity equations for water vapor (QV), cloud water (QCW) and cloud ice (QI) are of the form:

$$\frac{\partial q}{\partial t} = - u\frac{\partial q}{\partial x} - w\frac{\partial q}{\partial z} + \frac{S_0}{\rho} \tag{3.6}$$

where u and w are the horizontal and vertical winds respectively.

The continuity equations for the precipitating fields of rain, snow, and graupel are of the form:

$$\frac{\partial q}{\partial t} = - u\frac{\partial q}{\partial x} - (w + \overline{V})\frac{\partial q}{\partial z} - q\frac{\partial \overline{V}}{\partial z} + \frac{S_0}{\rho} \tag{3.7}$$

with the term S_0 representing sources and sinks for the field q. $\overline{V}$ represents the mass-weighted fall speed of the mixing ratio field q.

The thermodynamic equation for temperature T is of the form,

$$\frac{\partial T}{\partial t} = - u\frac{\partial T}{\partial x} - w(\frac{\partial T}{\partial z} + \Gamma_d) + \frac{S_h}{\rho} \qquad (3.8)$$

where S_h is the diabatic heating contribution to T.

3.2 Chemistry Component

The chemistry parameterization is essentially the same as that discussed by Rutledge *et al.* 1986. Some of the more important features of that model will be discussed here as well as particular changes from the Rutledge *et al.* 1986 study.

The chemical species of the model are incorporated into the various hydrometeors by impaction, nucleation scavenging, absorption, coagulation and diffusion. Scavenging by inertial impaction is considered for rain, snow, and graupel, which fall relative to the chemical species. The continuous collection equation is used to represent this process (see Rutledge *et al.* 1986).

Nucleation scavenging is the predominant mechanism for in-cloud incorporation of the particulate chemical species (i.e. the particulate chemical species act as cloud condensation nuclei). This term is activated when the cloud water mixing ratio is greater than .01 g kg^{-1} or when the supersaturation exceeds 0.04% as this corresponds to the supersaturation necessary to nucleate particles in the .01 - .1 mm range, where most sulfate and nitrate containing aerosols are situated. This term is represented by:

$$\varepsilon q_{di}/\Delta t \qquad (3.9)$$

where ε is the scavenging efficiency for the particulate species (q_{di}) and Δt is

the integration time step. In this study ε for sulfate and ammonium was 0.5 and for nitrate ε was 0.9.

Absorption is considered for the gaseous species of sulfur dioxide, nitric acid, hydrogen peroxide (H_2O_2), and peroxyacetylnitrate (PAN) . This process is assumed to follow Henry's Law equilibrium between the gas and liquid phases in the cloud. Diffusion and coagulation are included to represent Brownian capture by cloud water and cloud ice.

The in-solution chemistry parameterized by the model includes oxidation of S(IV) to sulfate via reactions with ozone and hydrogen peroxide. Hydrogen peroxide is carried as a dependent variable in the model and becomes depleted through this reaction. Ozone, on the other hand, is assumed to be of constant concentration throughout the model simulation. Decomposition of PAN to nitrate is also included and is a source term for nitrate. Neither photochemical reactions nor oxidation of nitrate to nitric acid are included in the model.

Once incorporated, the chemical components can be transferred between hydrometeor fields by microphysical processes (e.g. nitrate in snow to nitrate in rain as a result of melting) or undergo chemical reactions (e.g. oxidation of SO_2 in cloud water to sulfate in cloud water). A schematic representation of the sulfur and nitrogen chemistry is given in Figs. 3.2 and 3.3. Each chemical component in each hydrometeor field is represented by a differential equation of mass continuity. This is formulated as follows:

$$\frac{dq_{ij}}{dt} = S_{ij} - L_{ij} \qquad (3.10)$$

where q_{ij} is the mass mixing ratio of species i in the jth reservoir (e.g. sulfate in

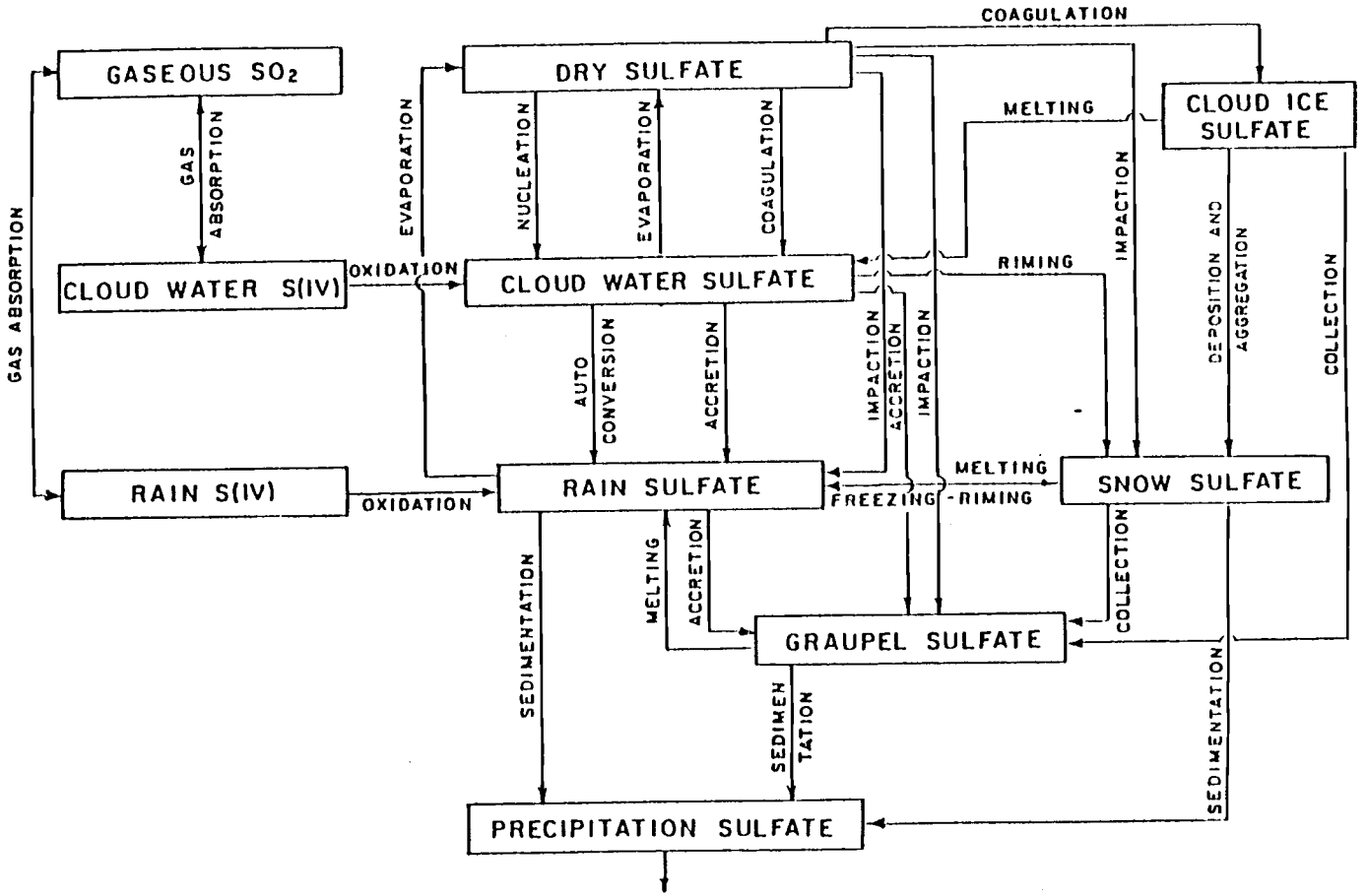

Fig. 3.2 Schematic showing the sulfate scavenging processes for the 2-D kinematic model. (Adapted from Rutledge *et al.* 1986).

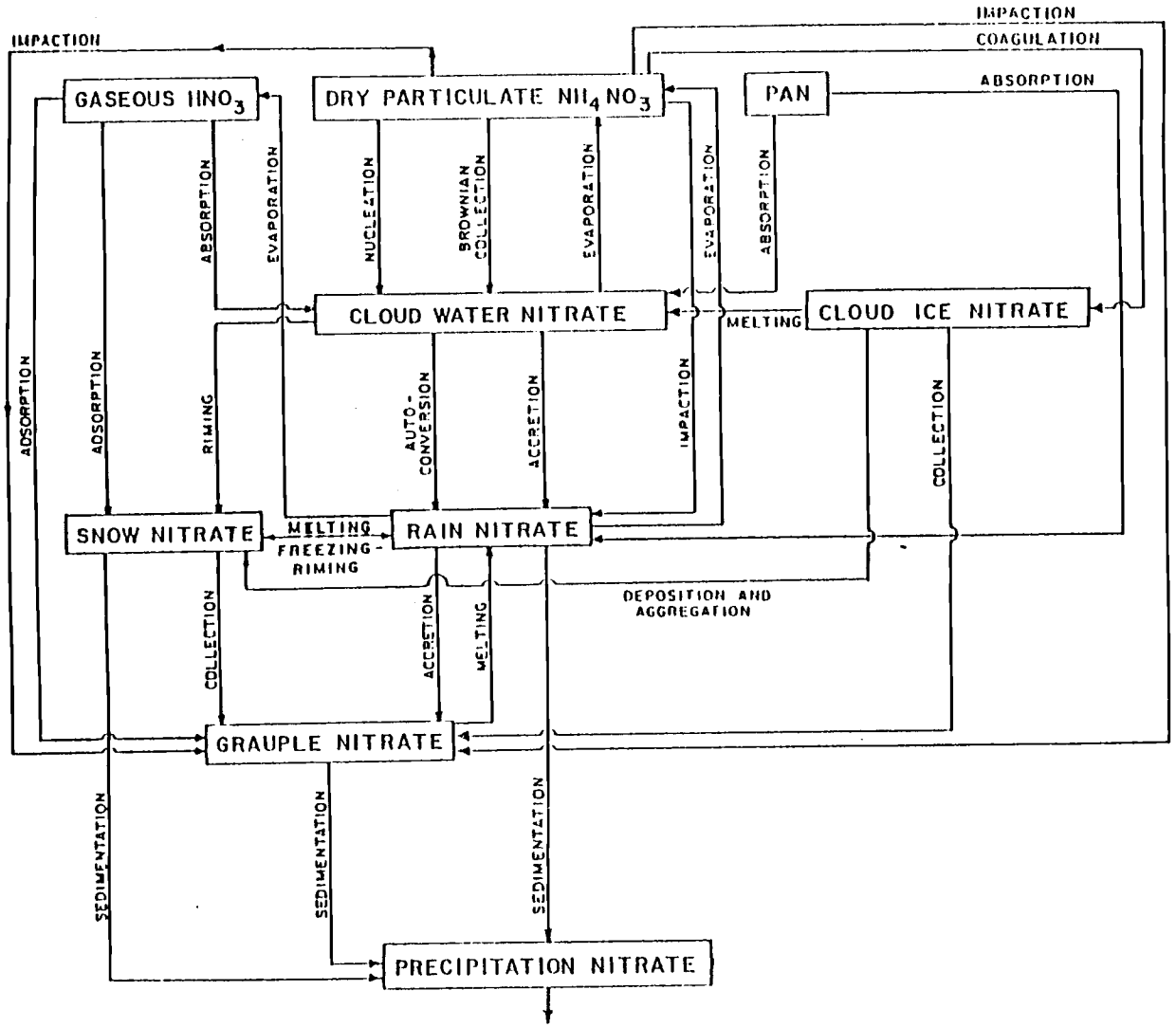

Fig. 3.3 Schematic showing the nitrate scavenging processes for the 2-D kinematic model. (Adapted from Rutledge *et al.* 1986).

cloud water) and S_{ij} (L_{ij}) represents sources (sinks) for the ith constituent in the jth reservoir. The source and sink terms represent either the transfer of a chemical species from one microphysical field to another or a chemical reaction, as described above.

The model requires a vertical profile of each chemical constituent which is assumed to be homogeneous in the horizontal at model initialization. The formulation for this profile is given by :

$$q_i(z) = q_i(0) \exp(-z/H_i) \qquad (3.11)$$

where $q_i(0)$ is the mass mixing ratio at the surface for species i, H_i is the scale height for species i, and z is height above the surface. Hydrogen peroxide and PAN concentrations were prescribed at each level in the vertical based upon observations made aboard the University of Washington's C-131A research aircraft. Gaseous nitric acid, which is readily incorporated into all hydrometeors and is generally an important component in acid rain, was not considered in this study since airborne observations did not detect this species. As a result the nitrogen chemistry is relatively uninteresting. This will be discussed in more detail in Chapter 5.

The output variables for the chemistry component of the model are the equilibrium mass mixing ratios of the various chemical species in the model (e.g. SO_2, sulfate in snow, nitrate in cloud water).

4. MODEL INPUTS

4.1 Kinematic Structure

The air motion pattern used in this study was derived from the 6 March 1986, 1940 GMT dual-Doppler radar synthesis done at the University of Washington. The radial velocity data from each radar (CP-3 and CP-4) were first unfolded interactively using the RDSS (Research Data Support System) software developed at NCAR. This step is necessary to correct those velocities that are outside of the Nyquist velocity of the radar (± 14 m s^{-1} for GALE). The unfolded velocity data from each radar were then interpolated to a common cartesian coordinate system at which point the CEDRIC software (also developed at NCAR) was invoked to solve for the horizontal wind components using an iterative procedure. The vertical motion field was then derived from the divergence field by application of the continuity equation in anelastic form. The horizontal band-relative flow (found by subtracting 15 m s^{-1} from the cross-band derived winds) is shown in Fig. 4.1. The airflow is characterized by right to left motion at all levels (front-to-rear flow in a band relative sense) with the exception of a shallow layer of rear-to-front flow near the 4 km level corresponding to the observed upper level cold front. The diagnosed vertical motion is shown in Fig. 4.2. The maxima aloft indicate regions of convergence ahead of the upper-level cold front. The downdrafts located at lower levels are likely associated with evaporative cooling as precipitation fell into lower subsaturated layers. The observed radar reflectivity associated with the rainband is shown in Fig. 4.3. The precipitation from the rainband occupies a fairly narrow zone, spanning some 35 km in width. A narrow bright band was

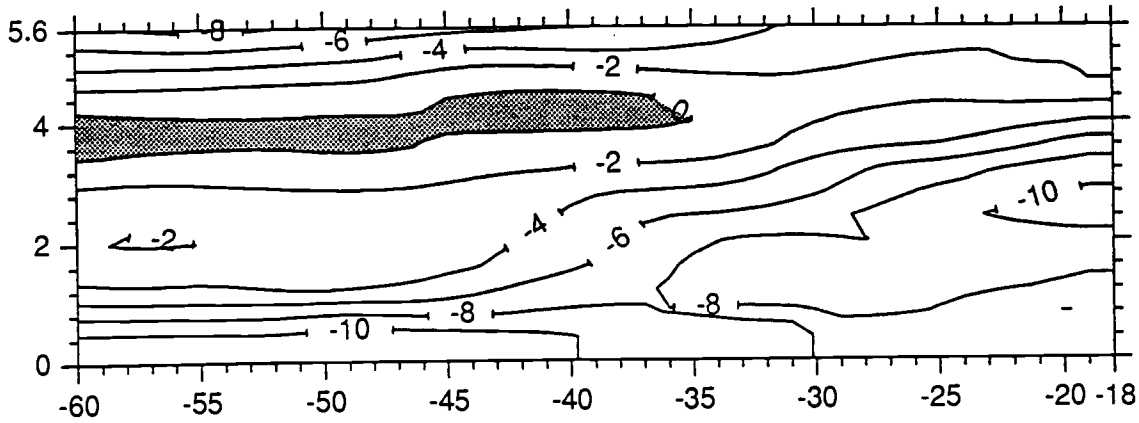

Fig. 4.1 Horizontal band-relative airflow (m s^{-1}), shaded area corresponds to left-to-right motion.

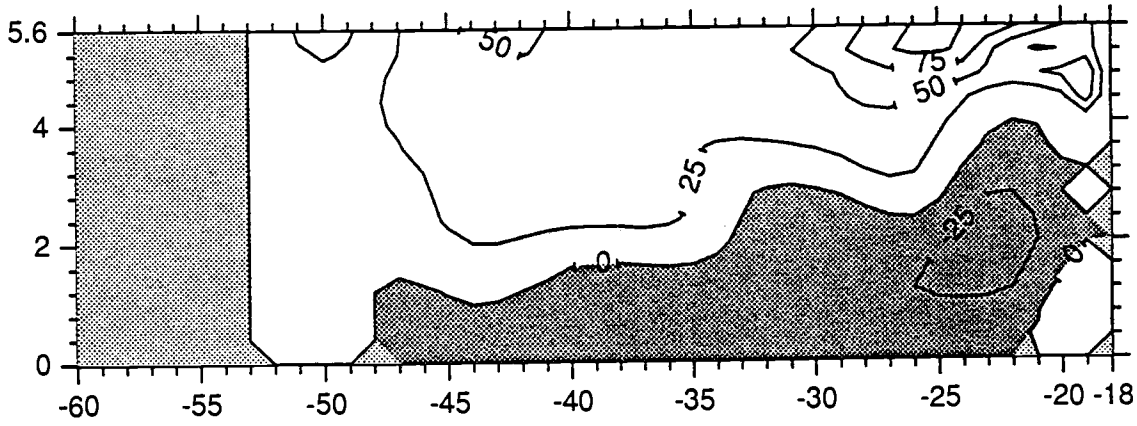

Fig. 4.2 Vertical airflow (cm s^{-1}), dark shading corresponds to downdrafts, light shading areas are w=0.

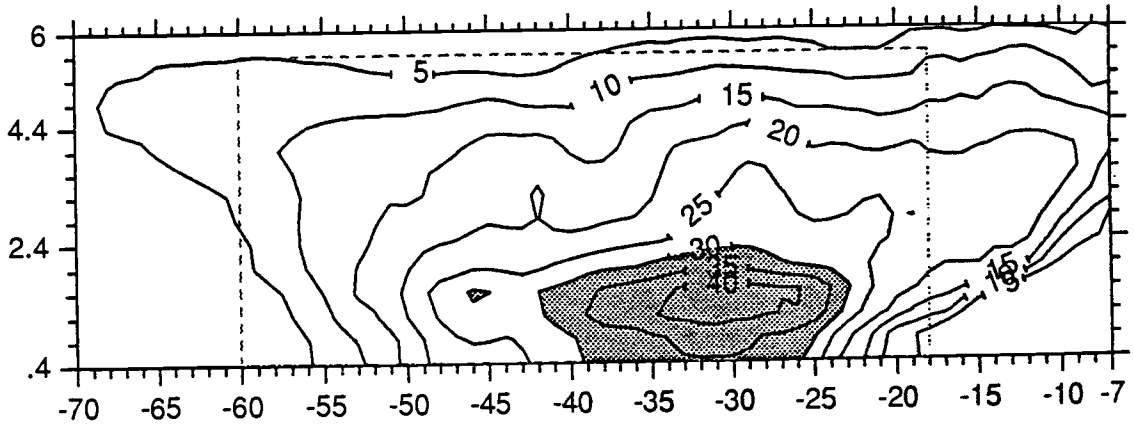

Fig. 4.3 Reflectivity in dBZ, dashed box indicates model domain.

present near z=1.6 km.

The kinematic patterns in Figs. 4.1 and 4.2 were found by averaging the synthesis data along a 40 km segment parallel to the rainband. This was done to eliminate noise introduced in the synthesis and to smooth out scales of motion below the model resolvable grid. The reflectivity profile (Fig 4.3) was also averaged along the same 40 km segment.

Because data were only available above z=0.4 km the horizontal flow was persisted to the surface and the vertical motion was set to zero. The model grid was extended for 7 km in the horizontal (with w=0 at all levels) in order to center the simulated cloud in the analysis domain. This will be discussed in greater detail in Chapter 5.

4.2 Thermodynamic Structure

The pre-band sounding was obtained from a rawinsonde launched from Wilmington, N.C. at 1735 GMT. The sounding obtained is shown in Fig. 4.4. Significant drying occurs below 850 mb. This has important consequences for the evaporative effects observed and the subsidence at low levels (cf. Fig. 4.2). Above 850 mb the sounding is generally saturated.

It should be noted that Locatelli *et al.* (1987) have done an extensive analysis of the 1900 GMT synoptic situation. The kinematic and thermodynamic inputs used in this study are in good agreement with the synoptic situation described in that paper. The model-simulated precipitation mechanisms (discussed in Chapter 5) also concur with their findings. The detailed analysis of Locatelli *et al.* treats this system as a warm occlusion with similarities to a katafront (as described by Browning and Monk, 1982). The precipitation

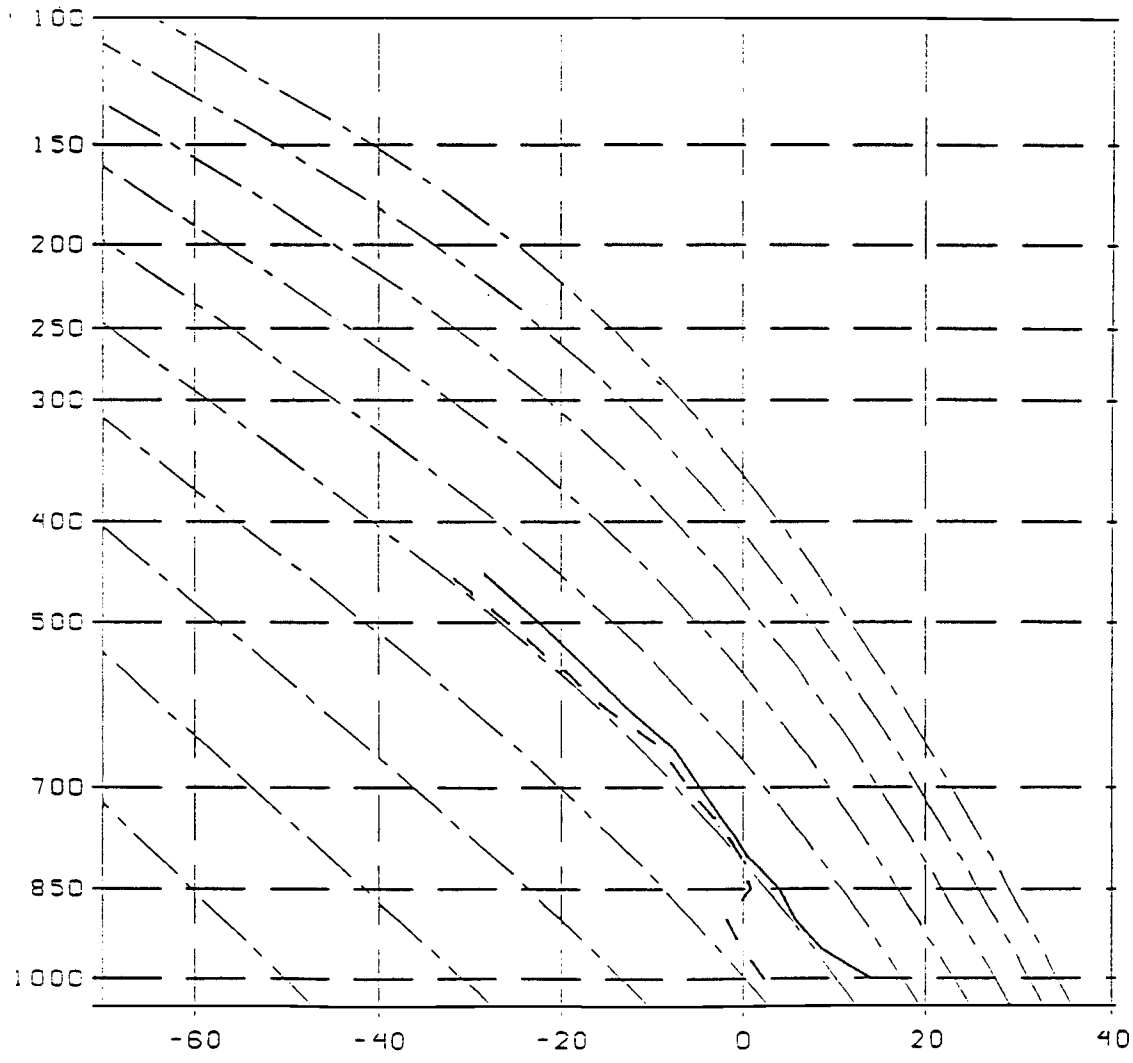

Fig. 4.4 Sounding from Wilmington N.C. at 1730 GMT on 6 March 1986.

classification for this rainband is considered to be wide cold-frontal (cf. Fig. 2.1).

4.3 Chemistry Inputs

Table 4.1 lists the chemical species, mass-mixing ratio at the surface, and the scale height as required for model input. As mentioned previously, the concentrations of H_2O_2 and PAN were prescribed at each vertical level and their initial profiles are shown in Figs. 4.5 and 4.6, respectively. All input chemistry values were determined by aircraft measurements ahead of the band.

The background ozone condition is taken to be 100 ppb. This has changed the ozone oxidation parameterization in cloud water to:

$$9.451 \times 10^{-19} \exp(6.778 \times 10^{3}/T)/(HQC)^{0.9} \qquad (4.1)$$

The formulation of equation (4.1) is identical for oxidation in rain except that HQC (the hydrogen ion content in cloud water) is replaced by HQR (the hydrogen ion content in rain).

Table 4.1. Values of $q_i(0)$ and H_i for the chemical species included in the model.

Chemical Species	$q_i(0)$ (g kg^{-1})	H_i (km)
SO_2	3.7×10^{-6}	2.0
$SO_4^=$	1.4×10^{-6}	3.5
NH_4^+	2.6×10^{-7}	3.5
NO_3^-	1.6×10^{-7}	2.0

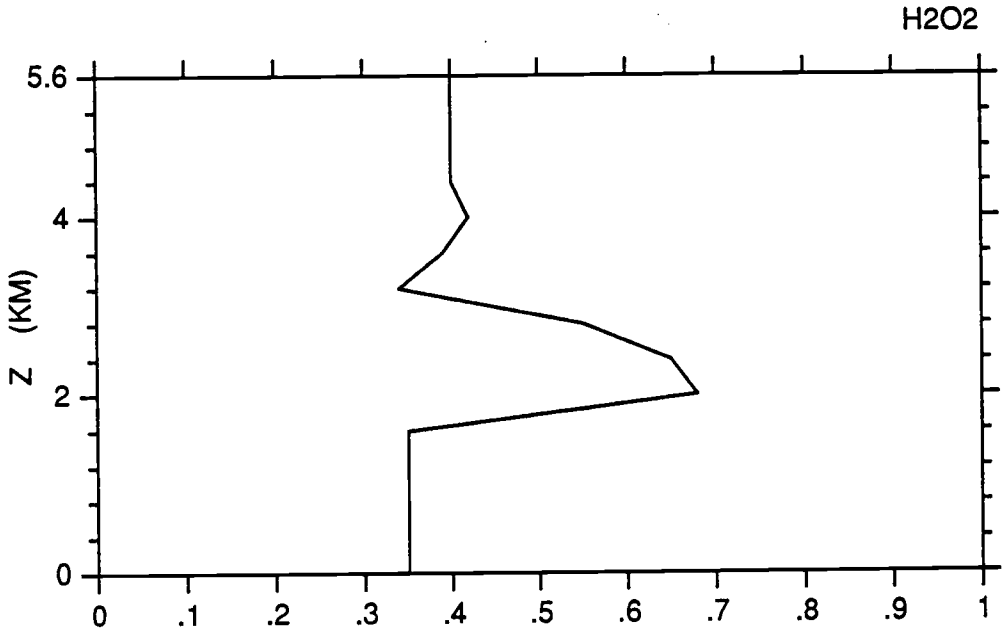

Fig. 4.5 Initial profile for H_2O_2. Units are 10^{-9}g g^{-1}.

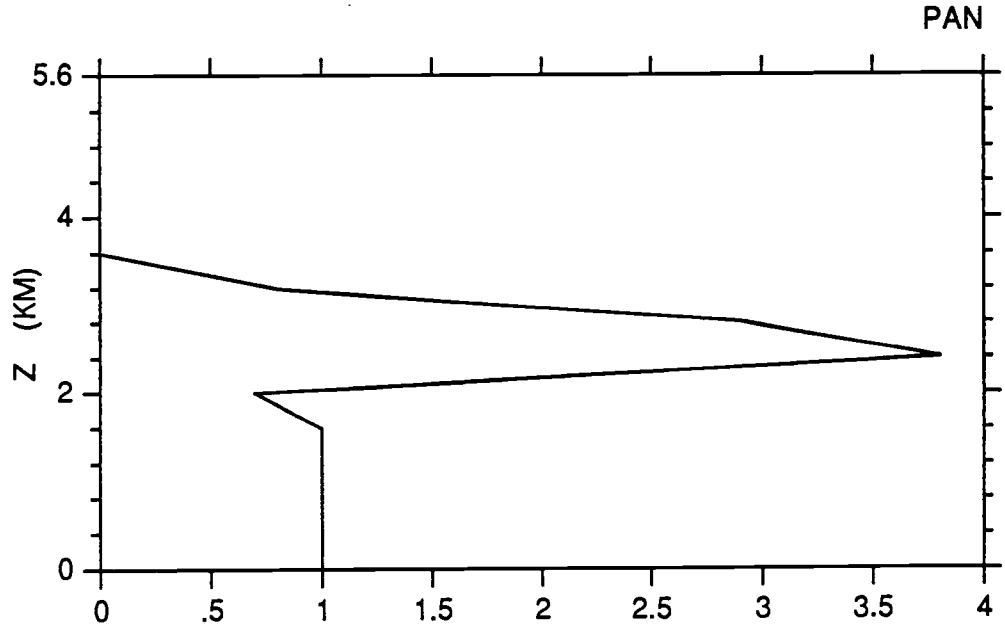

Fig. 4.6 Initial profile for PAN. Units are 10^{-10}g g^{-1}.

5. DISCUSSION OF BACKGROUND SIMULATION

In this chapter model results for a background simulation, i.e. a simulation using the observed conditions for model input, will be discussed. The features of both the model-generated cloud and cloud chemistry will be described but comparisons to observations and details of pollutant scavenging mechanisms will be delayed until Chapter 6. All fields shown are equilibrium fields which occurred after 10,000 s of integration time. All simulations were run on the CRAY-XMP at the National Center for Atmospheric Research. As a reminder, the acronyms used below for the cloud microphysical processes are shown schematically in Fig. 3.1. A complete list of the acronyms used can be found in Rutledge *et al.* (1986).

5.1 Results from the cloud component of the model

The model output microphysical fields of cloudwater (QCW), snow (QS), and rain (QR) are shown in Figs. 5.1-5.3 respectively. Their features will be addressed in the context of the precipitation and hydrometeor growth mechanisms present.

Ice particles were generated aloft by the activation of ice nuclei (PINT) in the regions of updraft maxima. After initiation they grew by vapor deposition (PDEPI) until being converted to snow (PCONV). The growth of snow occurred initially through deposition (PSDEP) and then through both deposition and riming (PSACW), giving QS its quasi two-cell structure (cf. Fig.5.2). Depositional growth predominated in the first cell (located between -21 and -37 km) whereas in the second region of high QS (located between -37 and -47 km), both riming and depositional growth took place. Both of these mechanisms

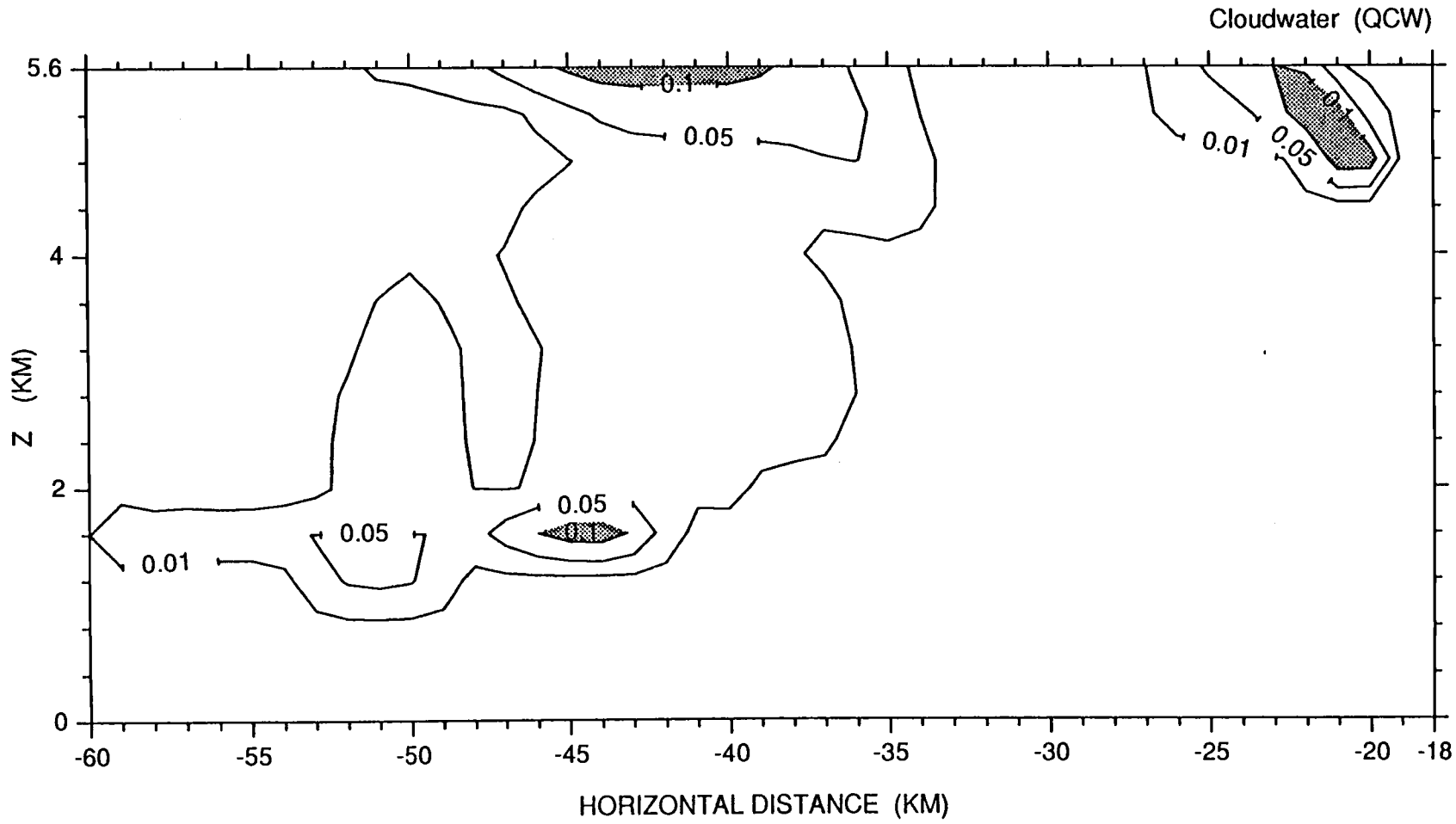

Fig. 5.1 Equilibrium field for the cloudwater mixing ratio. Units are g kg^{-1}.

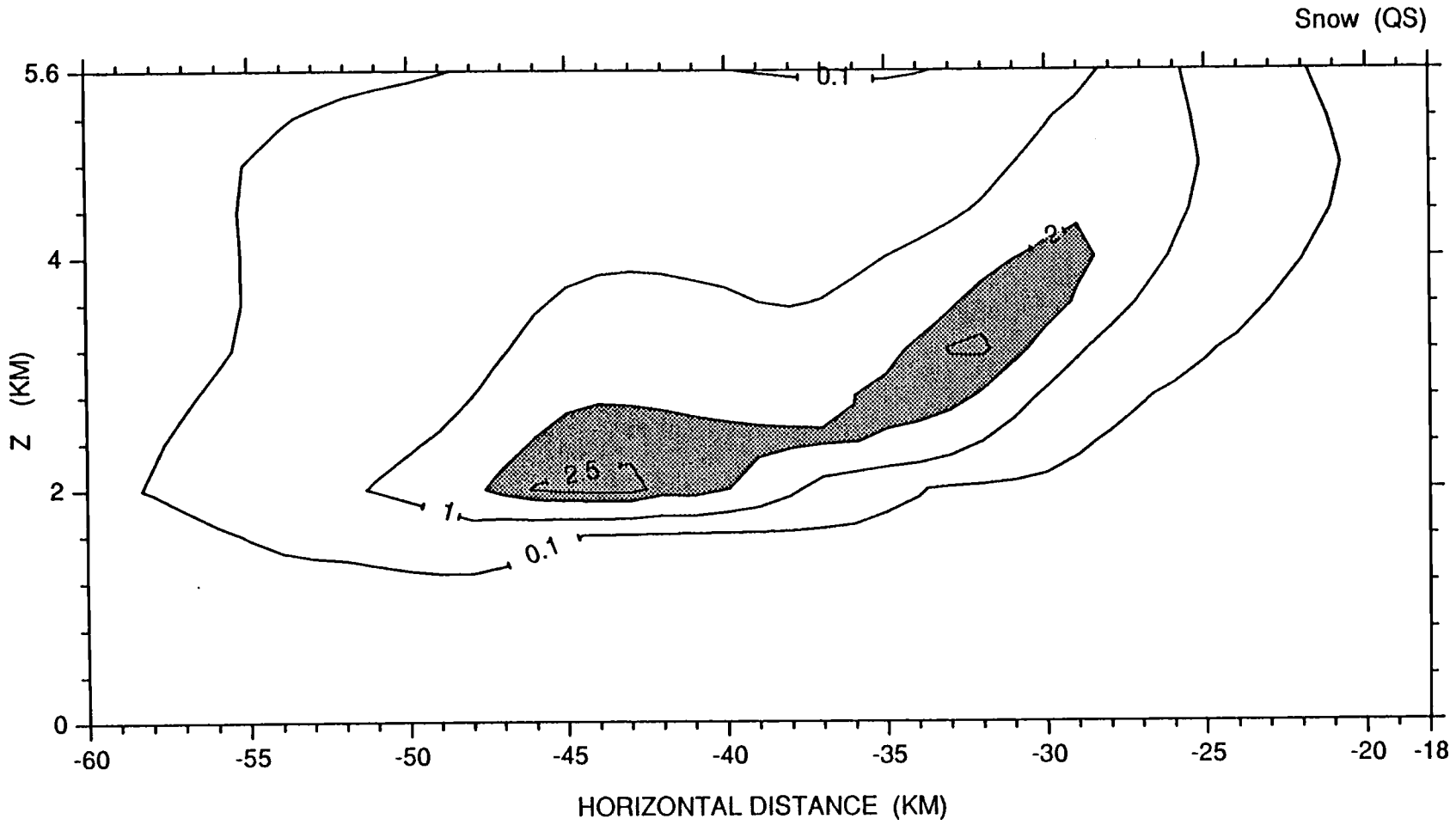

Fig. 5.2 Equilibrium field for the snow mixing ratio. Units are g kg^{-1}.

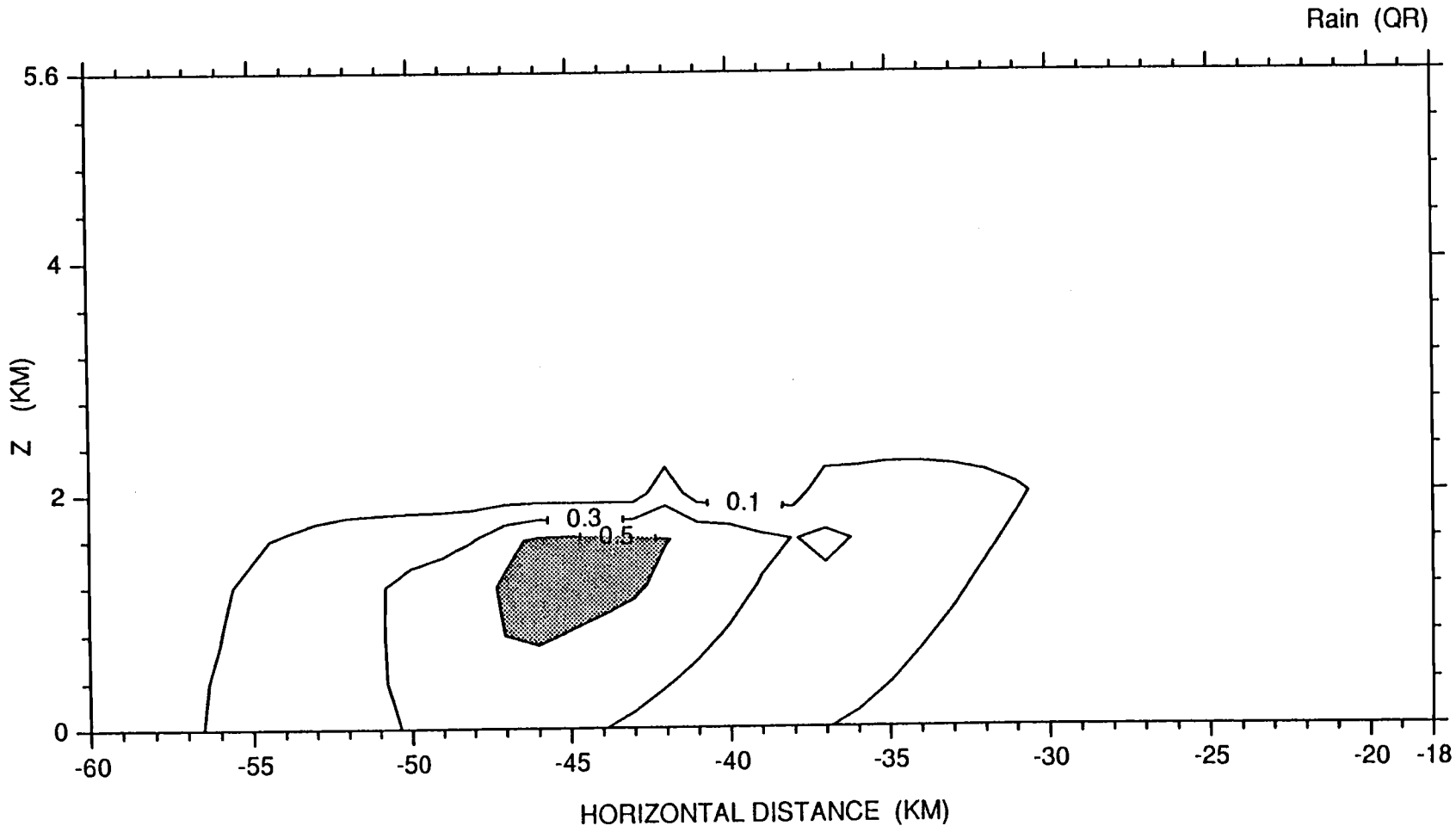

Fig. 5.3 Equilibrium field for the rain mixing ratio. Units are g kg^{-1}.

were responsible for the relatively low (~.05-.1 g kg^{-1}) cloudwater content (cf.Fig 5.1) and the relatively high (~.5-2.5 g kg^{-1}) snow mixing ratios. Cloudwater was produced by condensation (PCOND) in the center of the cloud with maxima at the upper-level updrafts and at the melting level when additional saturation was afforded by the cooling associated with melting. Cloudwater was noticeably absent below the upper-level generating cell, this being due to the large quantity of ice particles produced in the 1 m s^{-1} updraft, which then used all the available water for condensation via depositional growth. Rain was produced entirely from the melting of snow (PSMLT). There was some growth of rain associated with the collection of cloudwater (PRACW), but this term was less than the amount of rain that evaporated (PREVP). The values of the various microphysical terms are listed in Table 5.1. It should be noted that the rates of snow conversion (PCONV) and riming (PSACW) corresponded directly to the rates of depositional growth of ice (PDEPI) and condensation (PCOND), respectively (i.e. the riming rate was limited by the rate of cloudwater production and similarly the rate of snow generation was controlled by the depositional growth of ice). This entire cloud process is similar to the "seeder-feeder" mechanism described in Chapter 2, except that in our case the feeder zone is not well-defined (i.e. snow and ice particles were falling through a subsaturated region ahead of the surface precipitation area). Low-level evaporation and sublimation have been observed in other wide cold-frontal rainbands by Hobbs *et al.* (1980).

The evaporative effects mentioned in Chapter 4 are seen in the shape of both QS and QR. The snow field is sloped primarily from the subsidence beneath the generating cell region (cf.Fig.4.2). In this region PSDEP is

Table 5.1. Comparison between model derived hydrometeor production terms.

	Magnitude ($g\ kg^{-1}\ s^{-1}$)	
Source	Peak value	Average value
PINT	1.9×10^{-6}	2.6×10^{-7}
PDEPI	8.0×10^{-5}	1.0×10^{-5}
PCONV	6.4×10^{-4}	7.6×10^{-5}
PSDEP	6.9×10^{-4}	1.4×10^{-4}
PSACW	4.6×10^{-4}	6.1×10^{-5}
PRACW	3.7×10^{-4}	1.3×10^{-5}
PCOND	6.7×10^{-4}	6.3×10^{-5}
PSMLT	$-\ 6.2 \times 10^{-3}$	$-\ 4.0 \times 10^{-4}$
PREVP	$-\ 8.4 \times 10^{-4}$	$-\ 1.3 \times 10^{-4}$

negative, indicating sublimation. However, the trajectories of the snow particles resulting from the band-relative airflow also define the shape of QS. The rainwater field also shows the effects of evaporation (PREVP) with its maximum value near the 0°C level and a sloping leading edge (cf.Fig.5.3).

The model diagnosed fields of precipitation rate and reflectivity are shown in Figs. 5.4 and 5.5 respectively. The precipitation rate at the surface reached a maximum of 8.4 mm hr^{-1} with an in-cloud maximum of 12.5 mm hr^{-1}. The model generated reflectivity has very high values throughout the cloud due primarily to the high snow content. These will be discussed in terms of observations in Chapter 6.

5.2 Results from the chemical component of the model

In the following discussion of the cloud chemistry, the ammonium fields will not be directly addressed as they qualitatively imitate the nitrate fields. Ammonium has no sources in the model outside of its initial profile and its sinks are due entirely to microphysical processes. It is qualitatively the same as nitrate because the sources for nitrate in the model (outside of the initial profile) were negligible or non-existent. More specifically, the dissolution of PAN was unimportant and adsorption of gaseous nitric acid onto snow was not present (since nitric acid was not observed in the region of the rainband and consequently not used as model input). Therefore the nitrate profiles were only affected by microphysical processes as well.

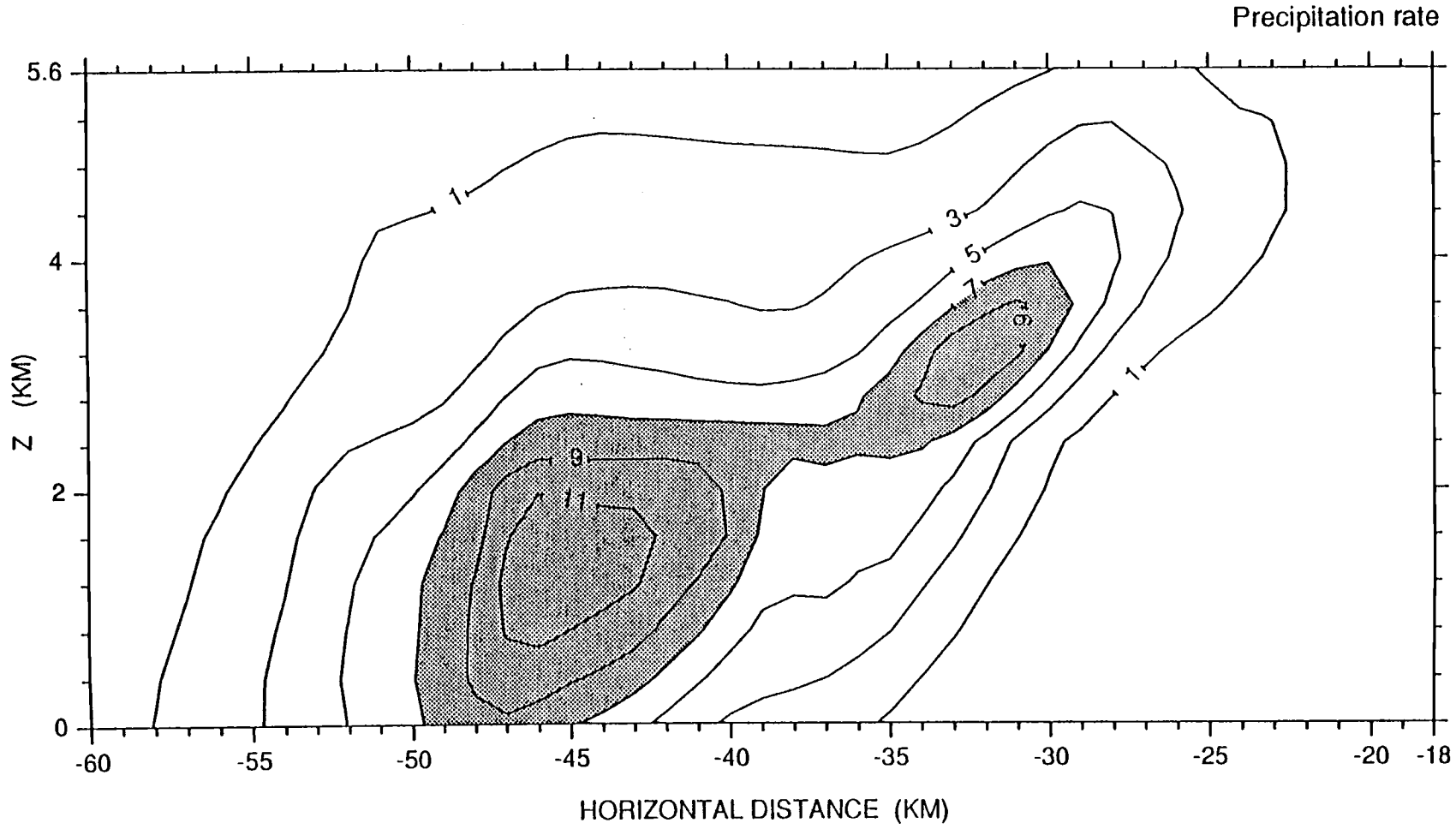

Fig. 5.4 Precipitation rate. Units are mm hr^{-1}.

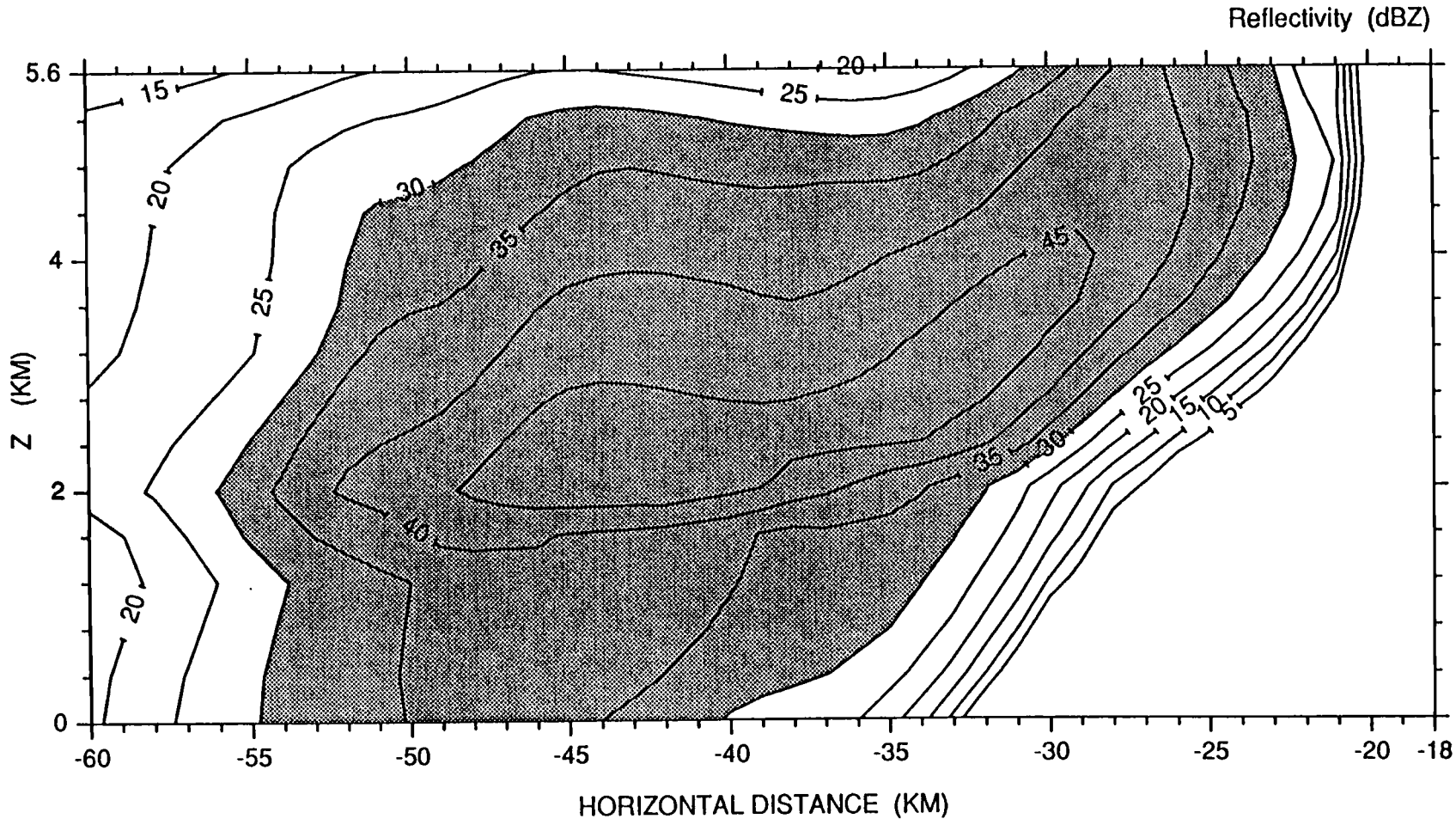

Fig. 5.5 Model calculated reflectivity (dBZ). Values greater than 30 are shaded.

5.2.1 Sulfate, nitrate, and hydrogen peroxide

The output fields for particulate sulfate (QDS), particulate nitrate (QDA), and gaseous H_2O_2 are given in Figs. 5.6-5.8 respectively. All of these fields show significant depletion at the edge of the cloudwater field (cf. Fig. 5.1). In the case of sulfate and nitrate this is due to nucleation scavenging, for H_2O_2 absorption into cloud water is the active scavenging mechanism. The increase of particulate sulfate at lower levels (to the left of x=-40) is due to evaporative effects of rainwater. The sulfate in rainwater is transferred back to the particulate phase upon evaporation. This effect is also seen in the peroxide (H_2O_2) and nitrate (QDA) fields, but to a lesser extent. The upper-level maxima for these fields (in the vicinity of x=-34) is primarily due to the stagnant band-relative airflow (cf. Fig 4.1) which creates a collection area for the chemical species. This will be discussed more fully in Chapter 6.

The sulfate, nitrate, and H_2O_2 in hydrometeor fields (cloudwater, snow and rain) are shown in Figs. 5.9 - 5.17. As these figures illustrate, the chemical species-in-hydrometeor fields tend to mimic their parent hydrometeor field, but with some exceptions. The fields of nitrate-in-cloudwater (Fig. 5.10) and H_2O_2-in-cloudwater (Fig.5.11) differ from QCW in that the chemical species are not uniformly distributed but concentrated in the leading edge of the cloud. However, this is just a reflection of the efficiency of nucleation scavenging and hydrogen peroxide absorption. Sulfate-in-cloudwater (Fig 5.9) more fully reflects the parent cloudwater field because of in-solution oxidation of SO_2 which takes place in the cloud interior. This oxidation of SO_2 is a source for cloudwater sulfate. The chemical species-in-snow fields (Figs.5.12-5.14) also show some differences from the QS field, primarily in the relative

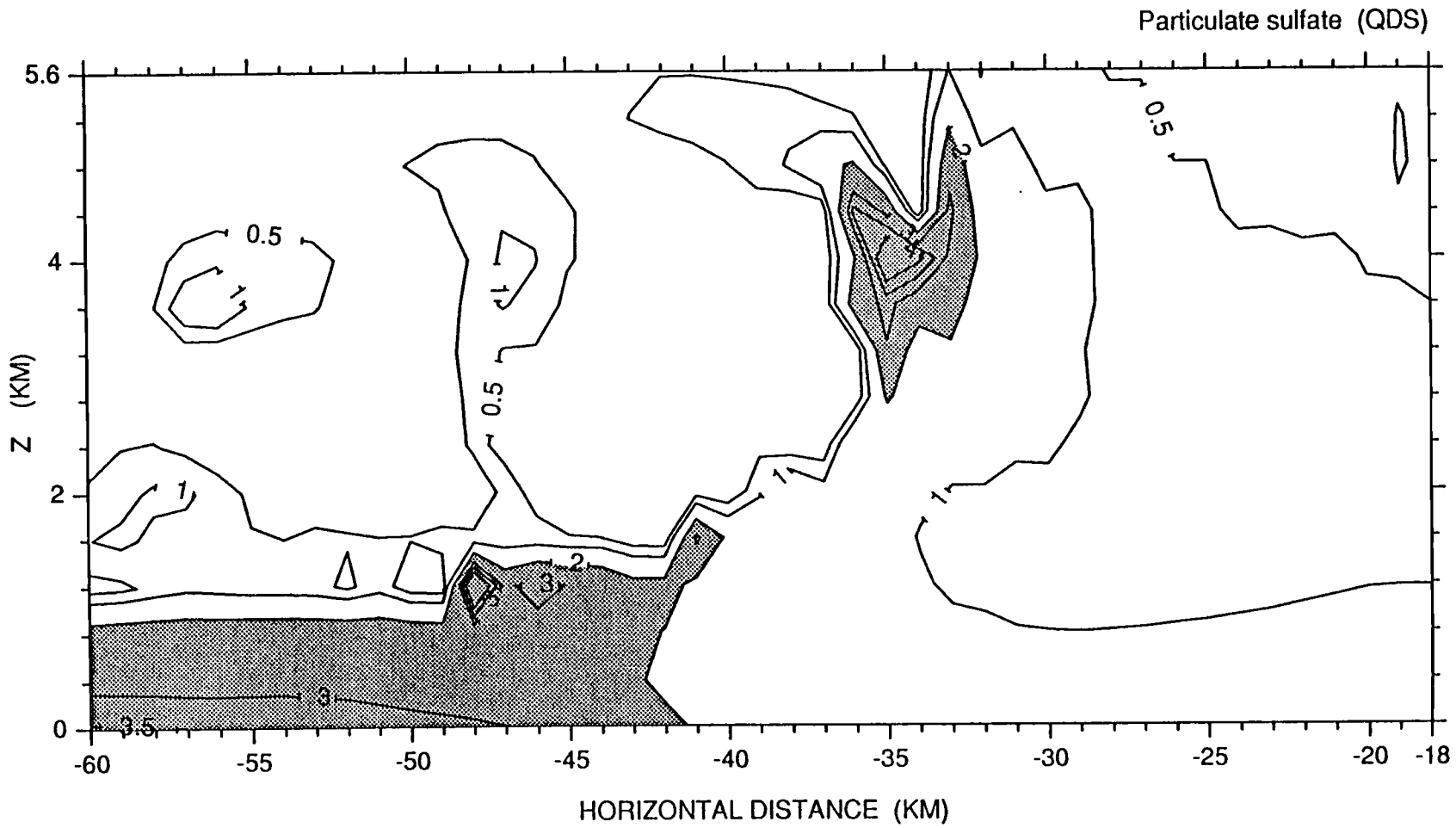

Fig. 5.6 Mixing ratio of particulate sulfate for the background simulation. Units are 10^{-9} g g^{-1}.

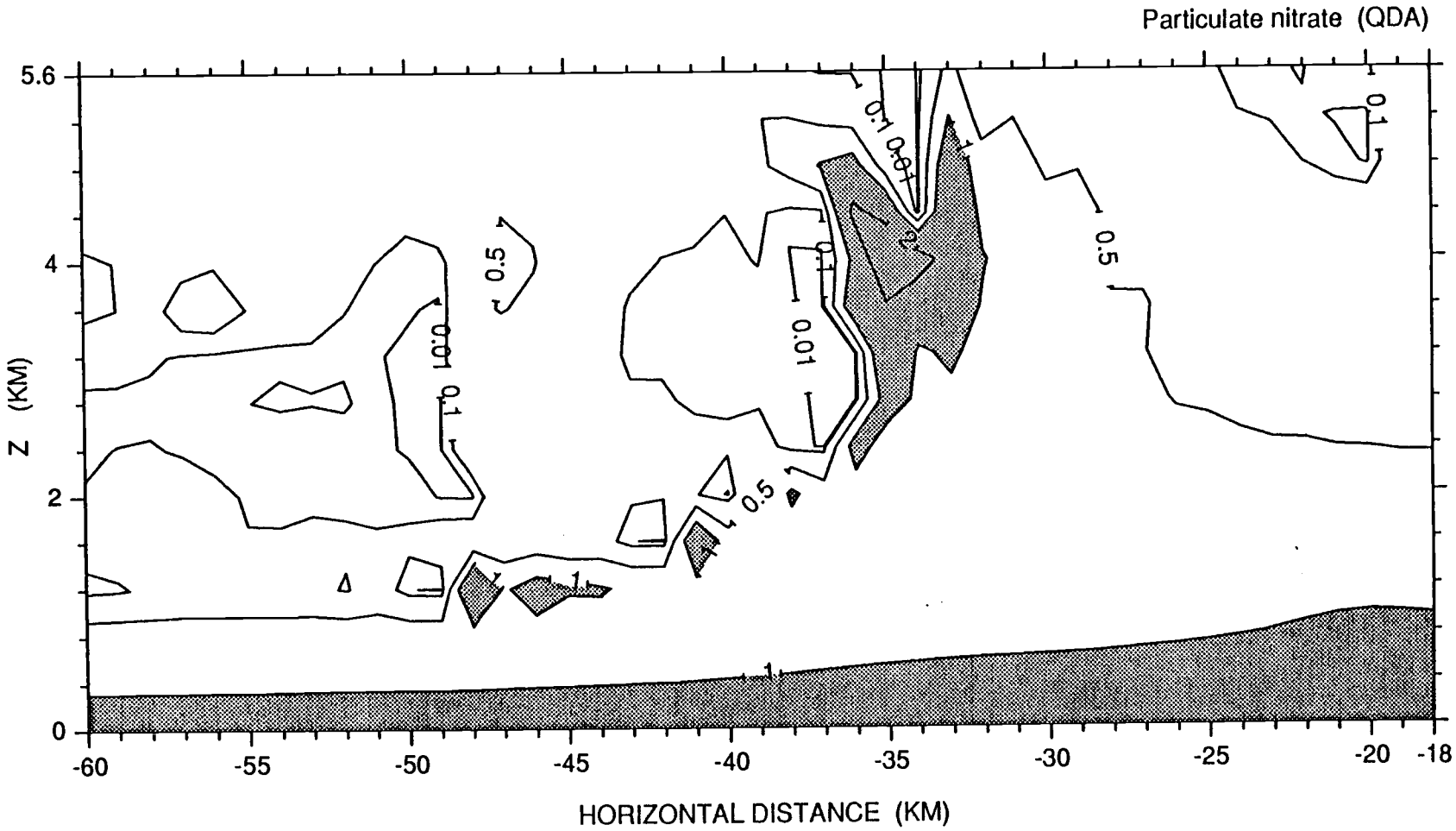

Fig. 5.7 Mixing ratio of particulate nitrate for the background simulation. Units are 10^{-10} g g^{-1}.

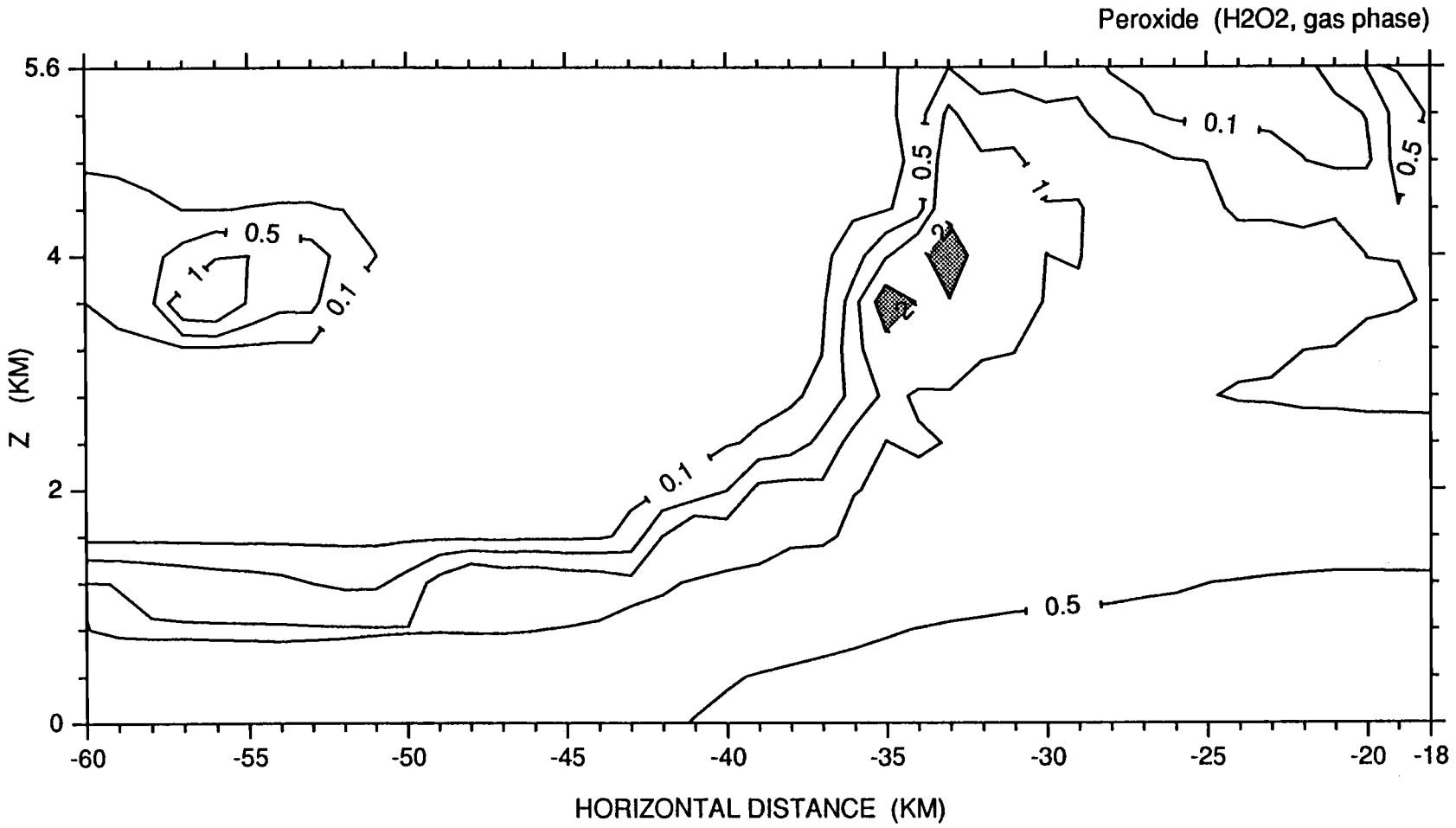

Fig. 5.8 Mixing ratio of gaseous H_2O_2 for the background simulation. Units are 10^{-9} g g^{-1}.

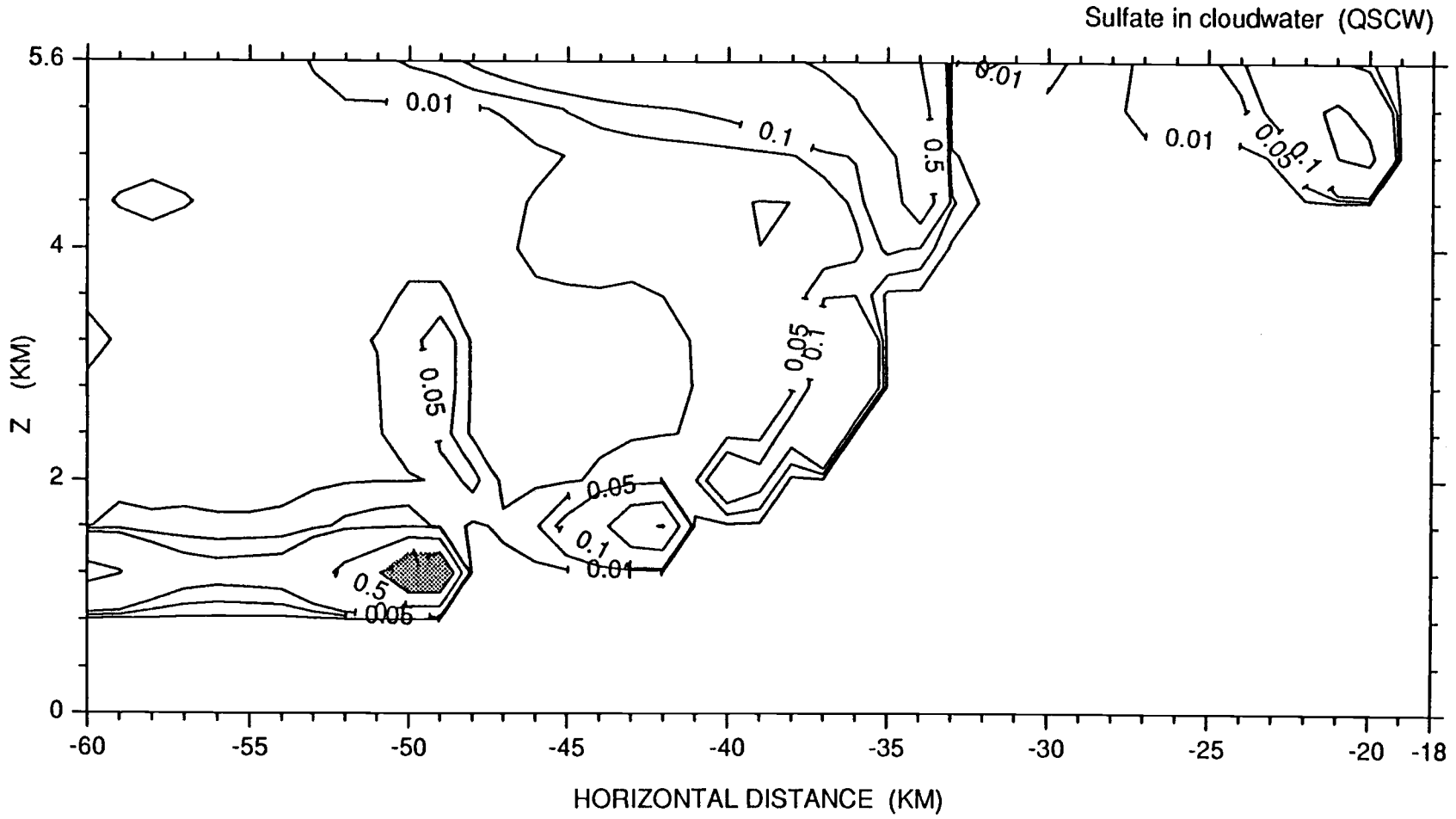

Fig. 5.9 Mixing ratio of sulfate-in-cloudwater for the background simulation. Units are 10^{-9} g g^{-1}.

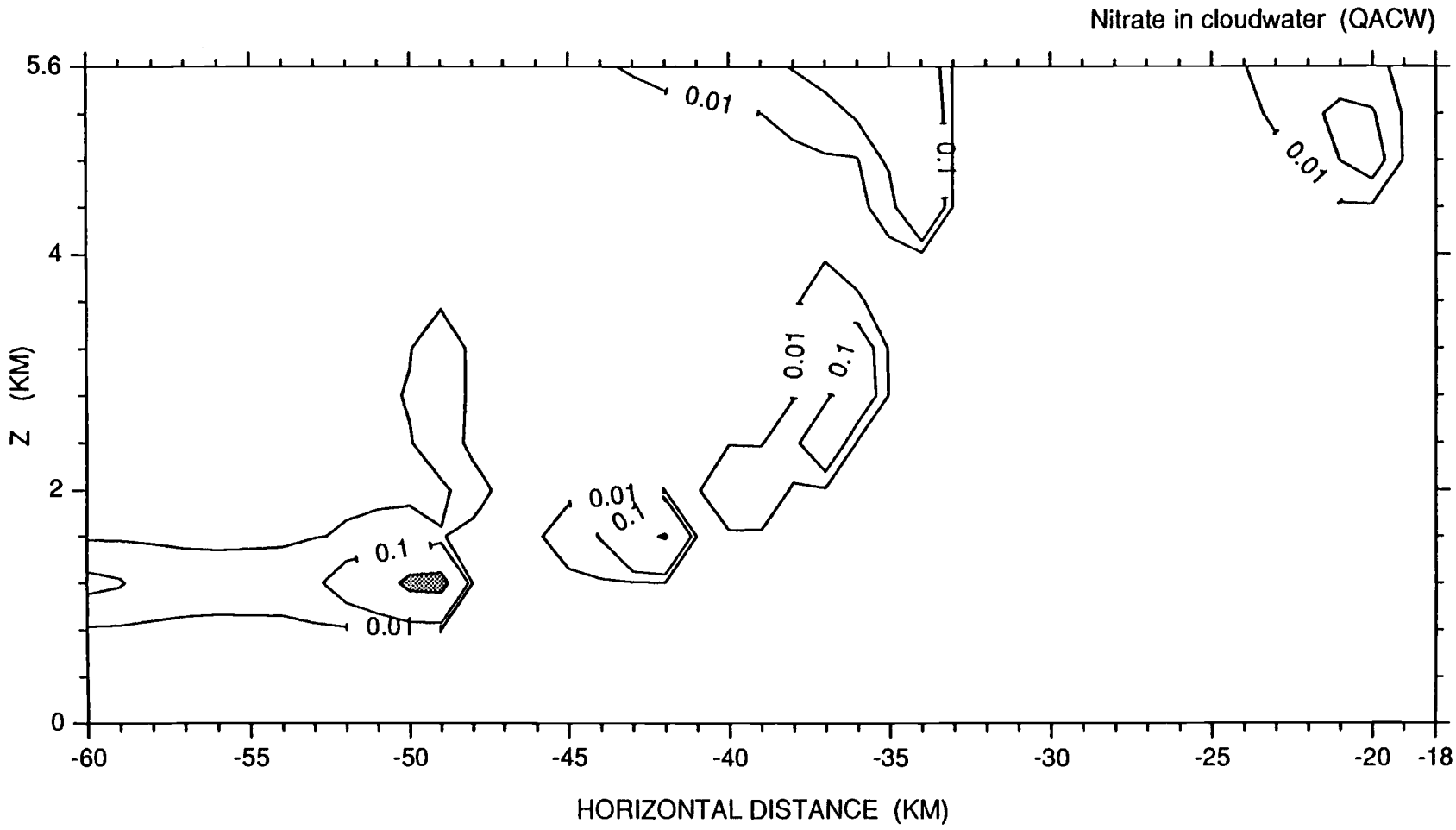

Fig. 5.10 Mixing ratio of nitrate-in-cloudwater for the background simulation. Units are 10^{-10} g g^{-1}.

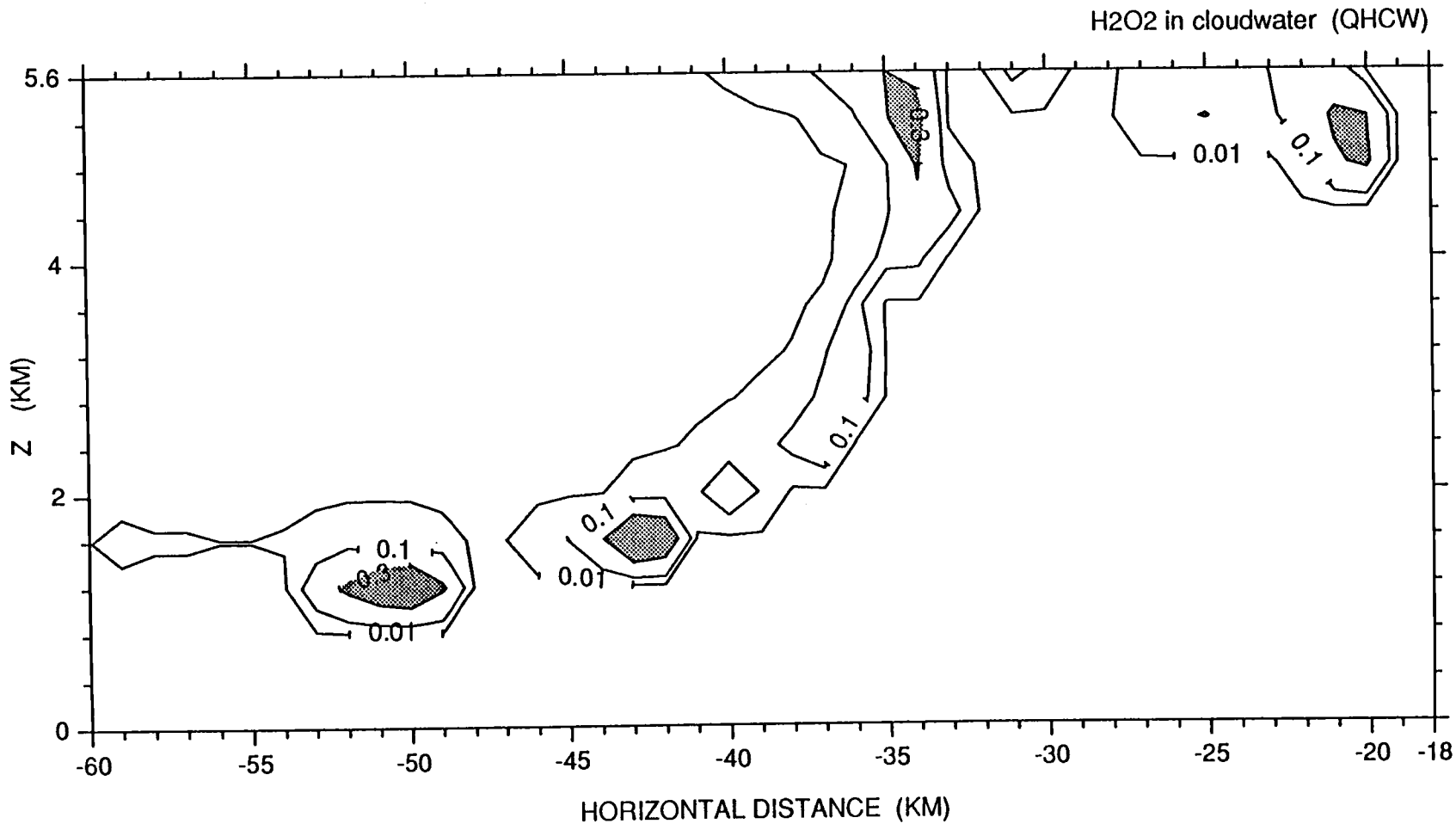

Fig. 5.11 Mixing ratio of H_2O_2-in-cloudwater for the background simulation. Units are 10^{-9} g g^{-1}.

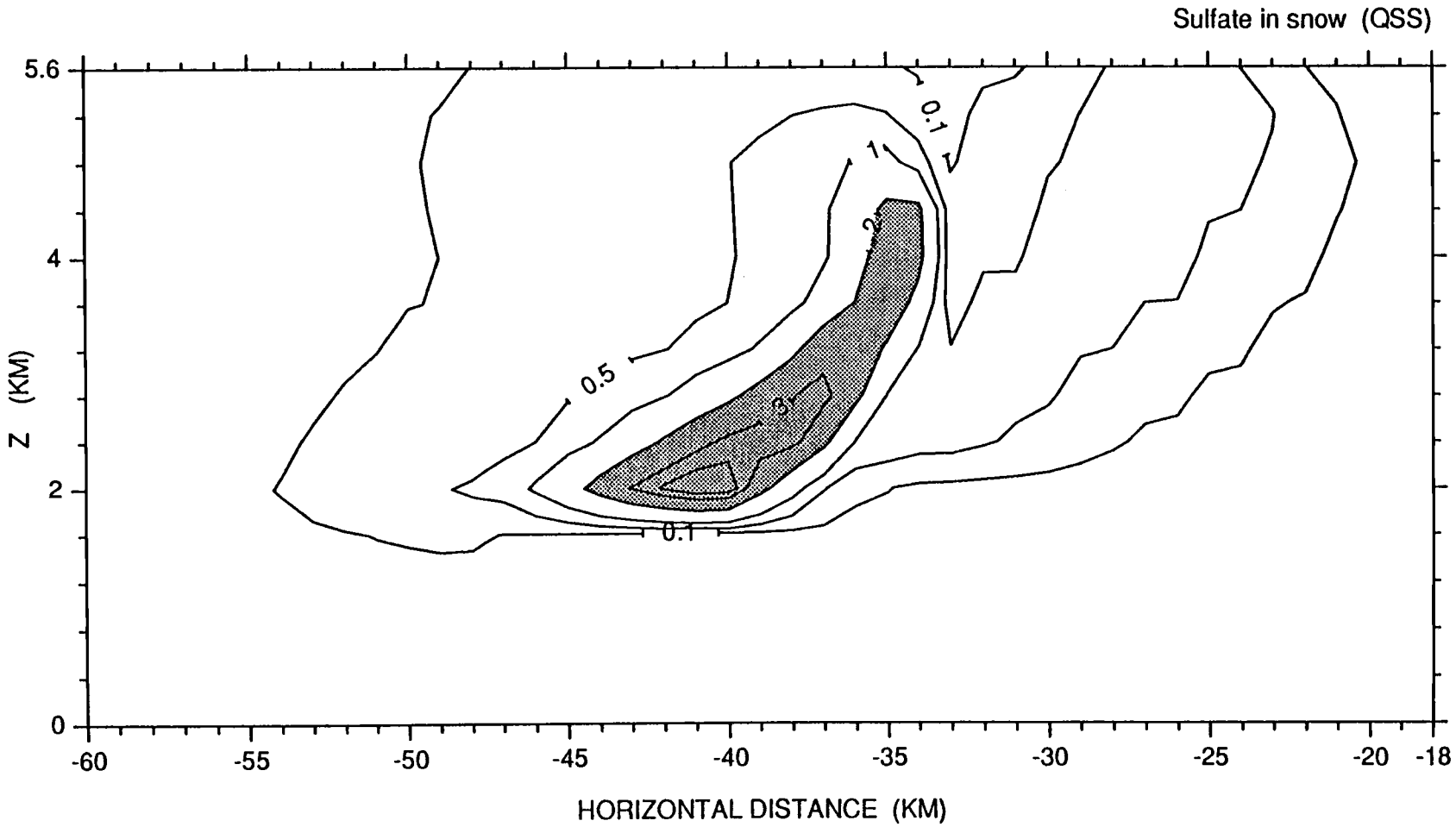

Fig. 5.12 Mixing ratio of sulfate-in-snow for the background simulation. Units are 10^{-9} g g^{-1}.

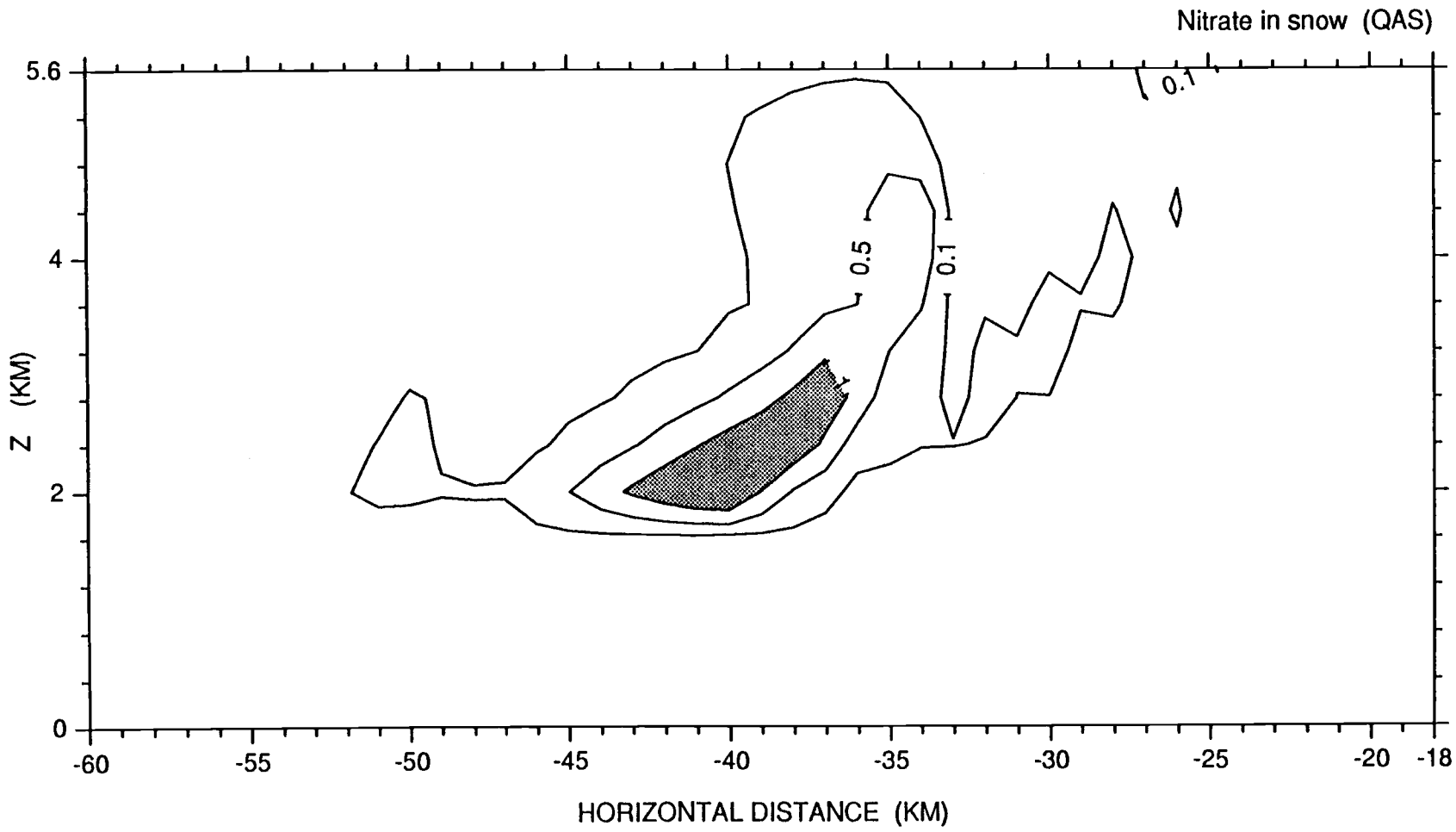

Fig. 5.13 Mixing ratio of nitrate-in-snow for the background simulation. Units are 10^{-10} g g^{-1}.

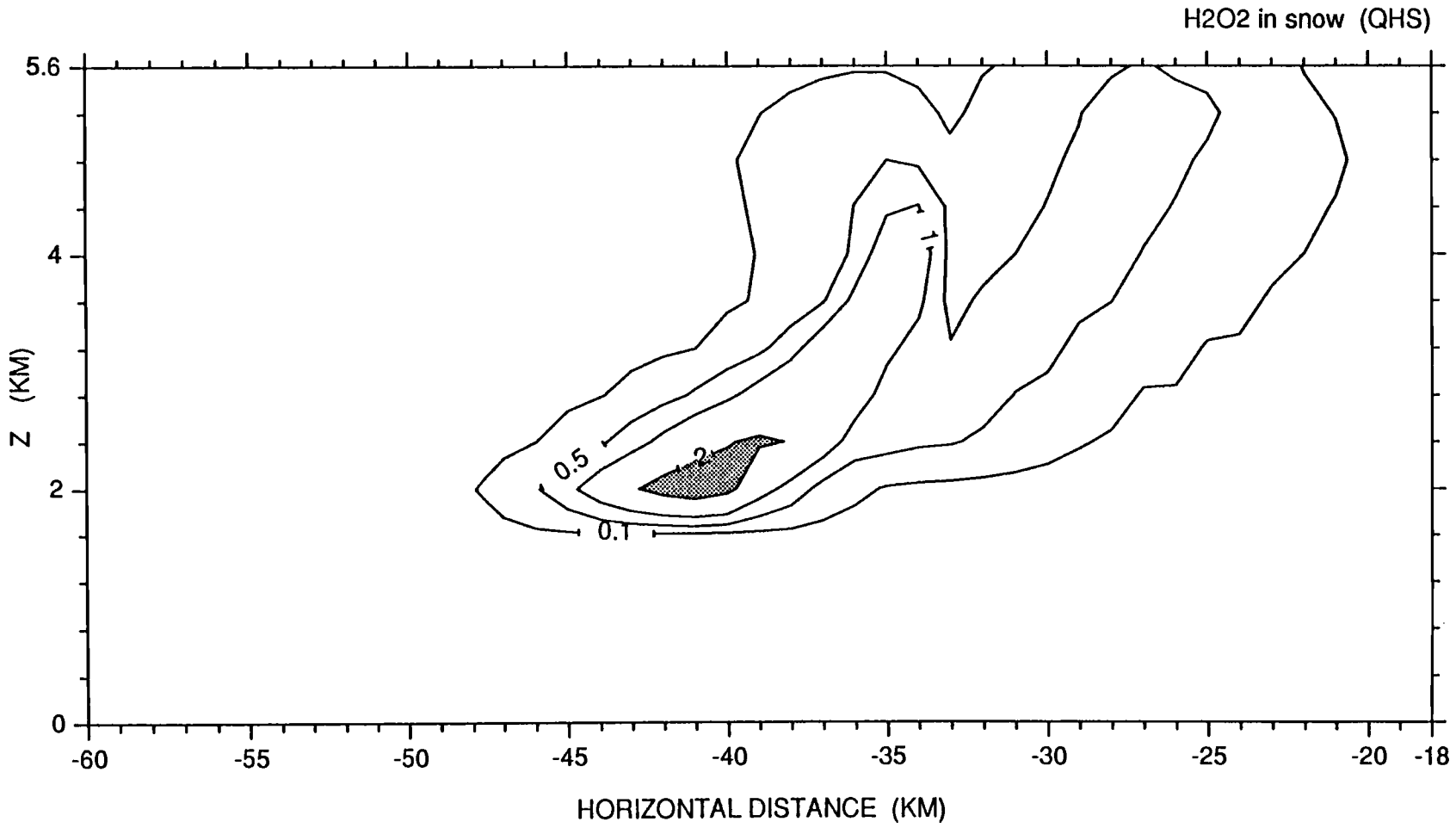

Fig. 5.14 Mixing ratio of H_2O_2-in-snow for the background simulation. Units are 10^{-9} g g^{-1}.

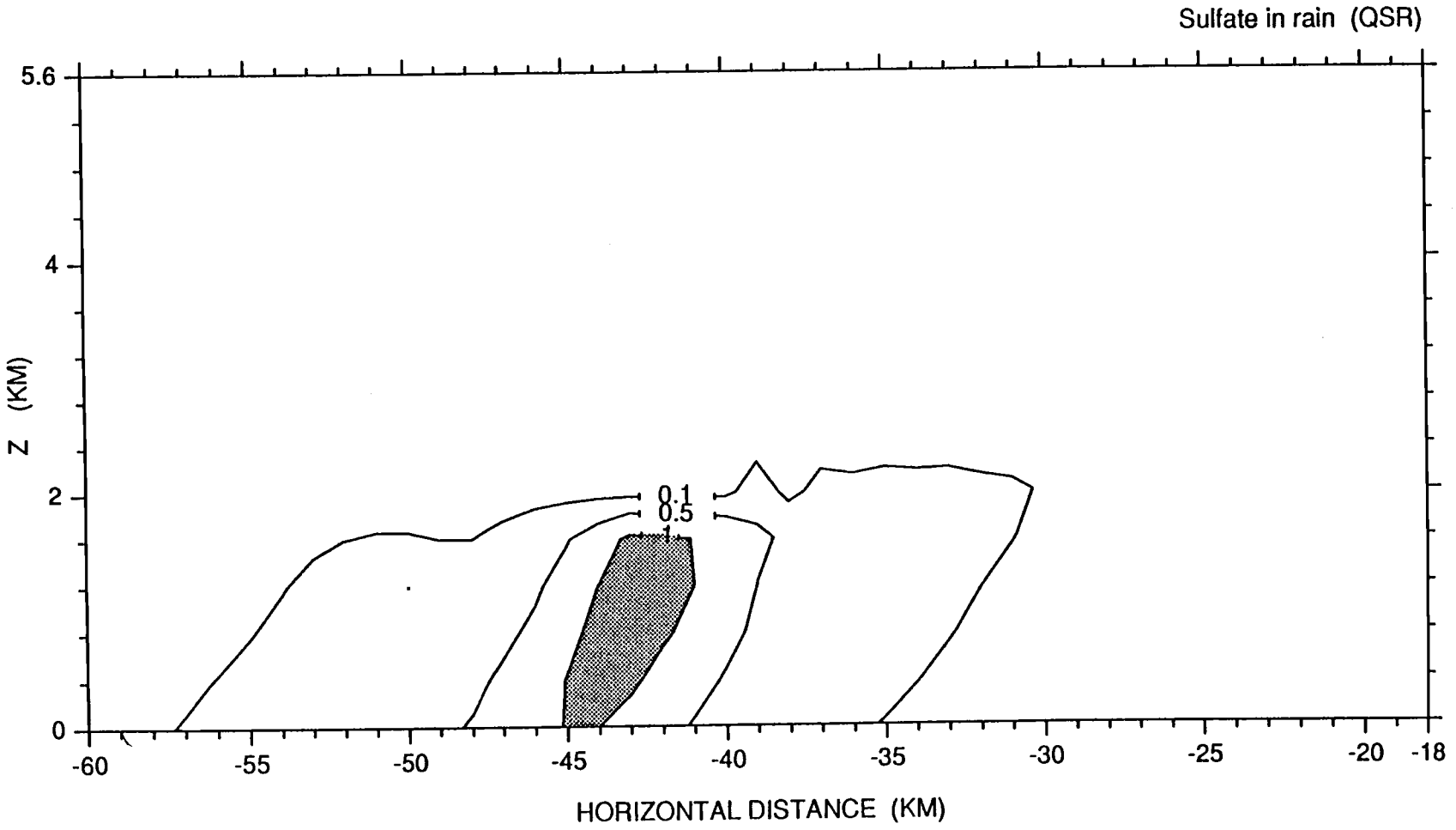

Fig. 5.15 Mixing ratio of sulfate-in-rain for the background simulation. Units are 10^{-9} g g^{-1}.

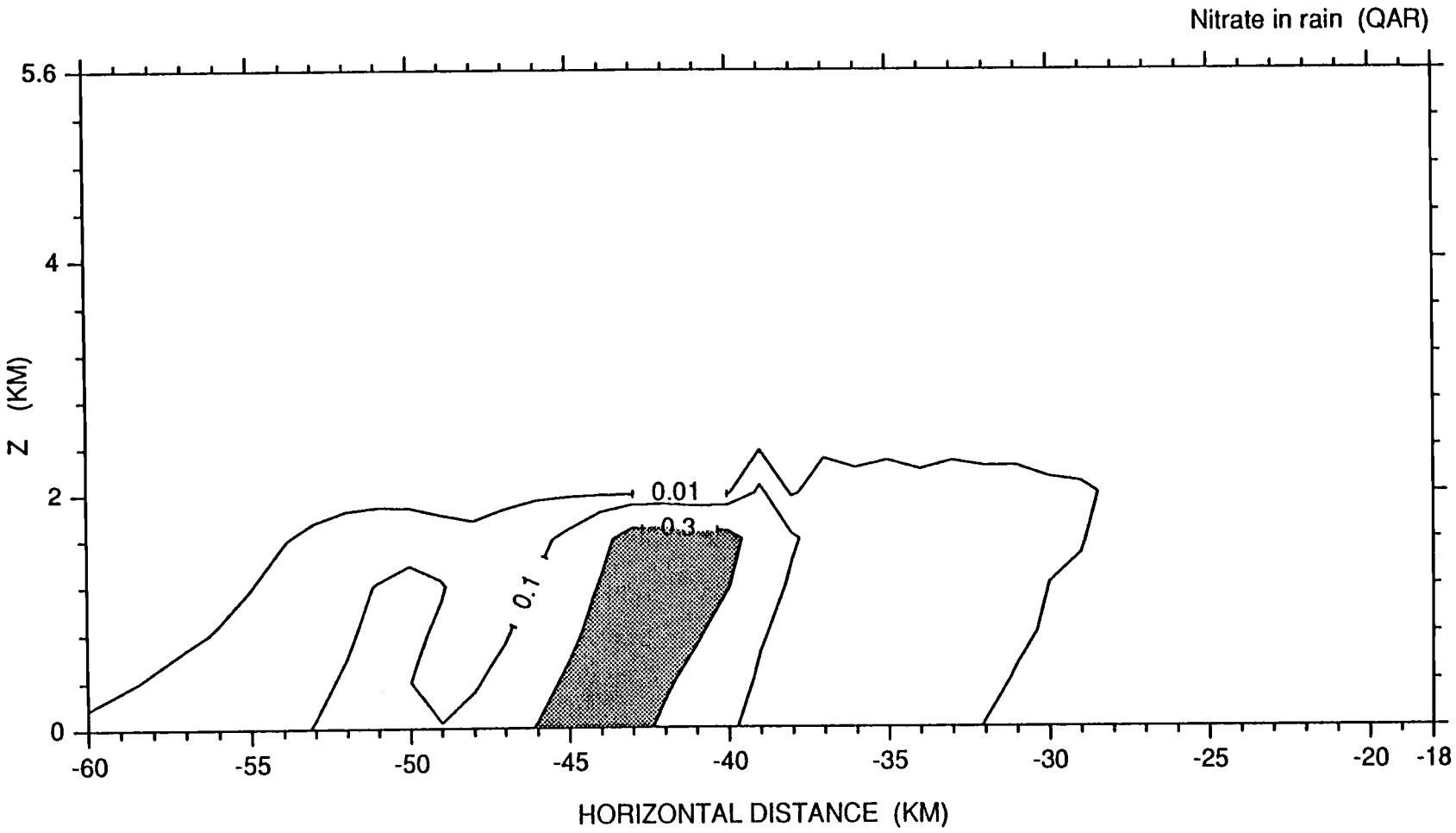

Fig. 5.16 Mixing ratio of nitrate-in-rain for the background simulation. Units are 10^{-10} g g^{-1}.

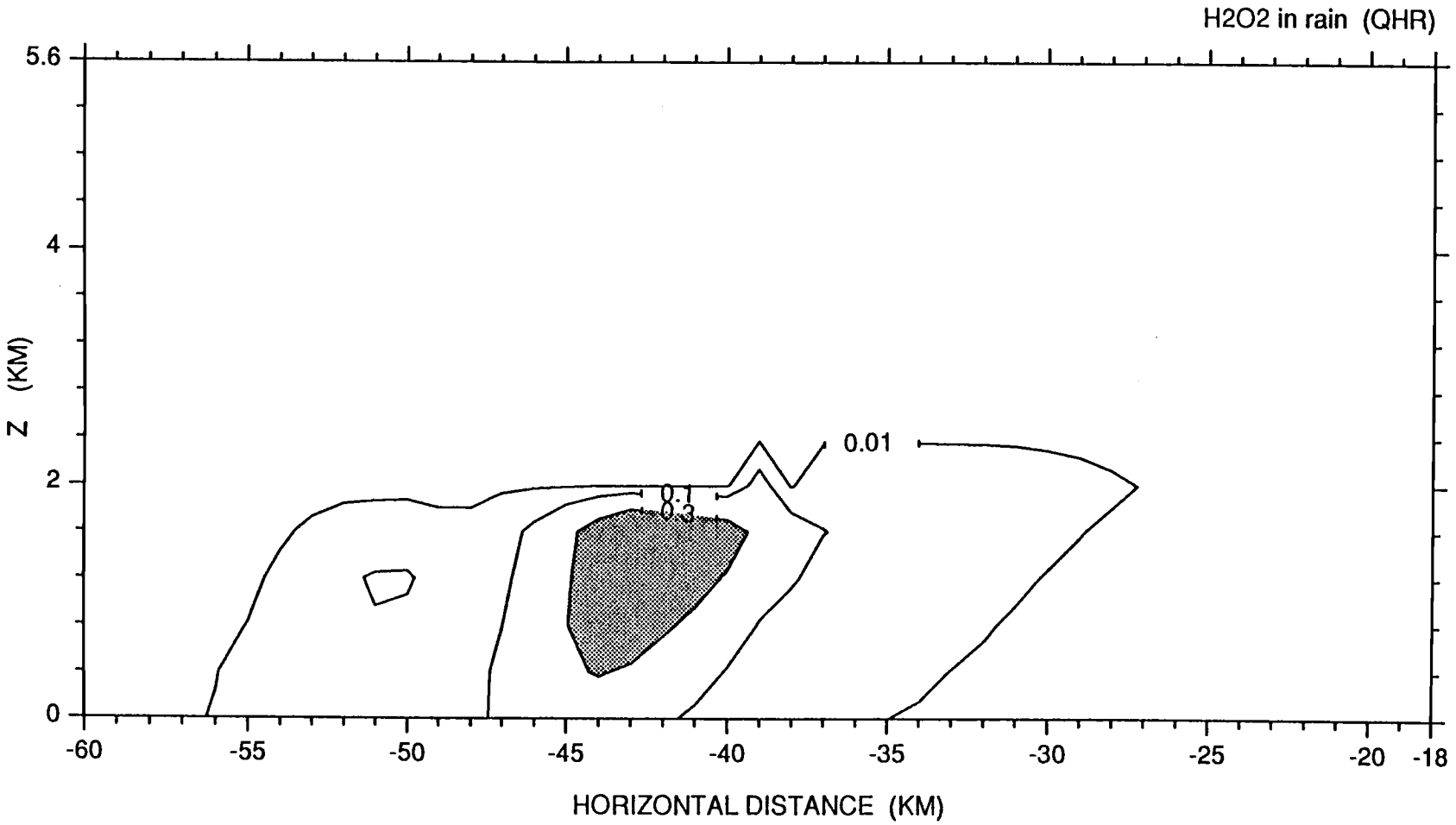

Fig. 5.17 Mixing ratio of H_2O_2-in-rain for the background simulation. Units are 10^{-9} g g^{-1}.

concentrations of the two regions of relatively large QS values. The chemical species-in-snow (sulfate, nitrate, and peroxide) are most concentrated in the low-level QS maximum where riming growth of snow is important. This represents the transfer from chemical species-in-cloudwater to chemical species-in-snow. Conversely, in the upper-level QS maximum, where depositional growth predominates, chemical mixing ratios are small. Impaction scavenging by snow is an inefficient process (compared to riming), therefore direct incorporation of the chemical species into snow from the particulate phase is not expected to contribute significantly to the chemical species-in-snow field. The chemical species-in-rain fields (Figs. 5.15-5.17) are only slightly different from the QR field and will be discussed later in relation to wet deposition rates.

5.2.2 Cloud acid generation

The acidity of the cloud is calculated by the standard method of hydrogen ion balance and is represented by the pH field shown in Fig. 5.18. Some important features of this figure include the surface minimum between -40 and -46. This corresponds to the maximum acid deposition area described below. Also noteworthy is the decrease in pH below 1.6 km prior to the precipitation maximum. This is due to oxidation of SO_2 in rainwater. The low-level increase in pH (decrease in acidity) near x=-47 is due to the lack of chemical species (and consequently hydrogen ions) in rain caused by previous scavenging. However at x=-50 there is a maximum of acidity due to renewed scavenging (cf.Figs. 5.9-5.11). This results from high cloudwater contents generated from the melting of snow. The evaporative effects mentioned earlier

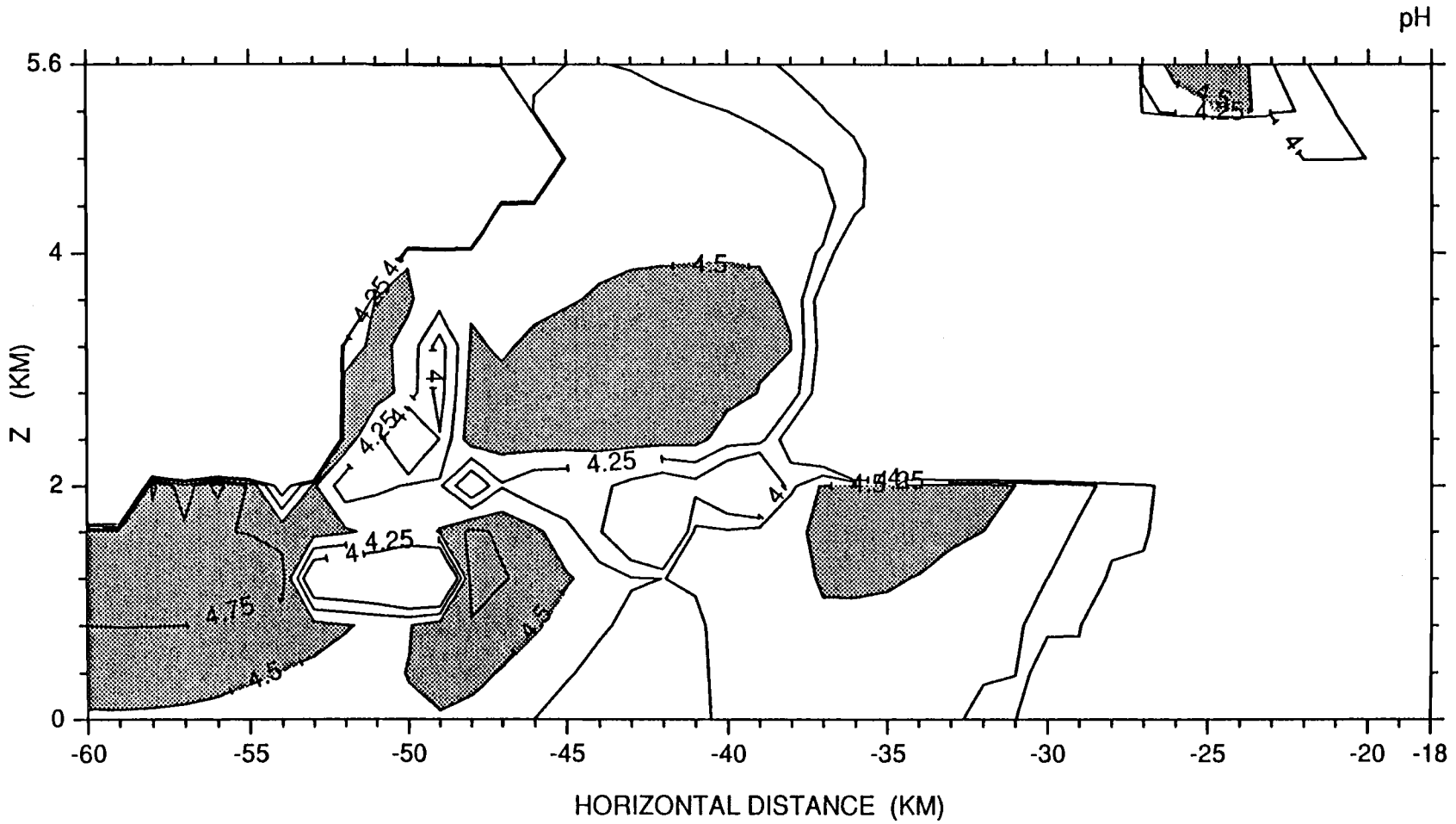

Fig. 5.18 pH of liquid hydrometeors for the background simulation. Shaded areas are pH greater than 4.5.

are responsible for maintaining the availability of chemical species in this region.

An integral part of sulfate deposition is the oxidation of SO_2 by both peroxide (H_2O_2) and ozone (O_3). The gas-phase field of SO_2 is shown in Fig. 5.19. It is characterized by depletion at low levels and an increase, or collection, in the middle and upper levels of the cloud. The fact that SO_2 is not depleted in the regions of cloudwater (a natural sink when oxidation is considered) is somewhat anomalous. This phenomenon will be clarified in light of the sensitivity studies of the next chapter. Evidence for the vertical transport of SO_2 by the band vertical motion field can be seen in Fig 5.19.

The equilibrium PAN field is shown in Fig. 5.20. Basically, only the effects of advection are present. The small amounts of cloudwater present prevented any significant dissolution of PAN into nitrate.

5.2.3 Deposition and transport

Much of the reason for studying interactions between pollutant and precipitating systems is to understand the mechanisms of deposition and transport operating within. Deposition rates for a particular species in the model can be estimated by taking the product of the chemical species-in-rain mixing ratio and the rainfall rate. This result, along with the rainfall rate, is shown in Fig. 5.21. All of the chemical species reach their peak deposition rate before the maximum precipitation rate. This is explained as follows. The chemical species are rapidly incorporated into the cloud at the leading edge of the cloudwater field and are transferred to snow at the onset of riming. This leaves a concentrated swath of chemical species at the front edge of the low-level snow

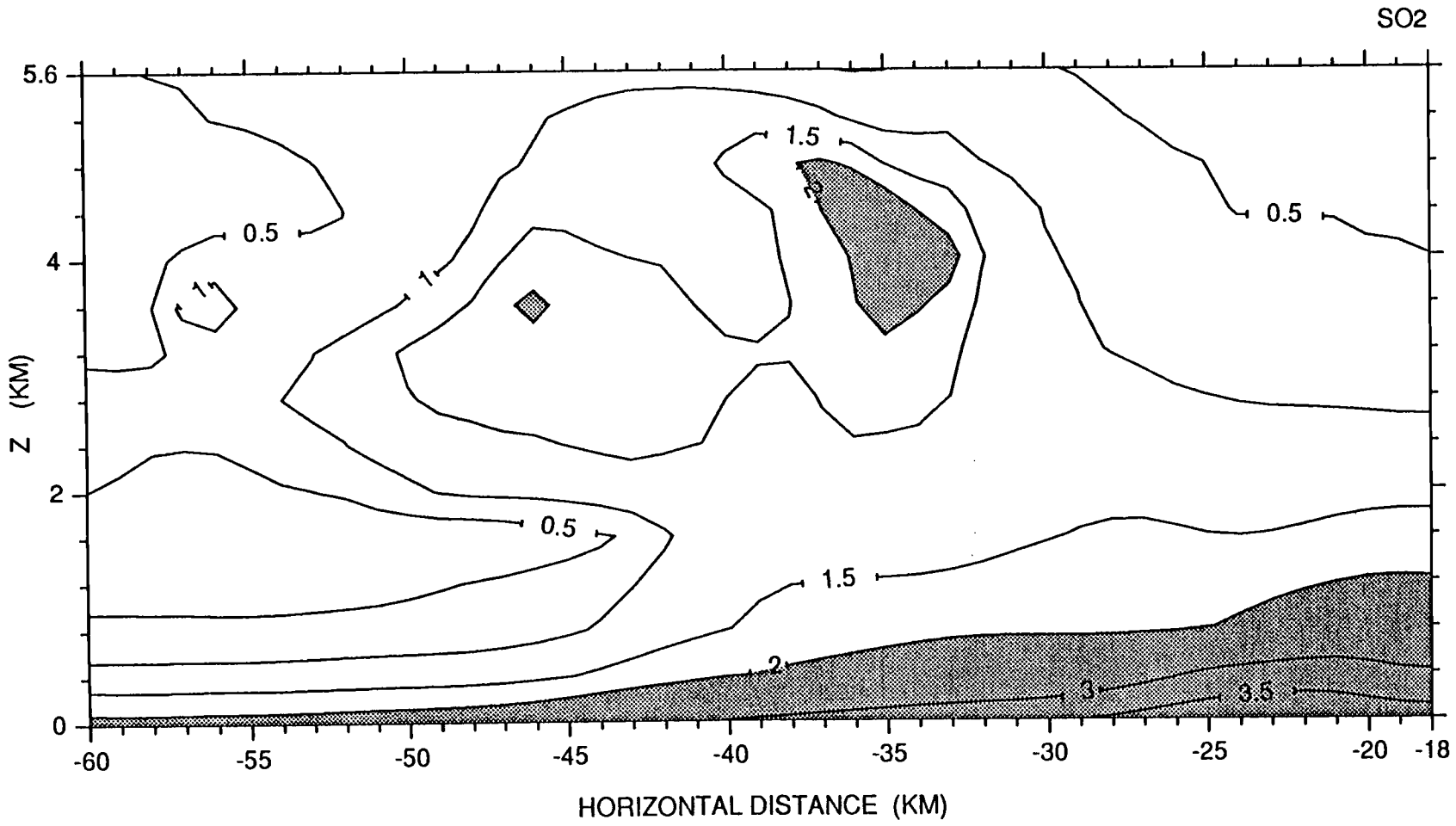

Fig. 5.19 Mixing ratio of SO_2 for the background simulation. Units are 10^{-9} g g^{-1}.

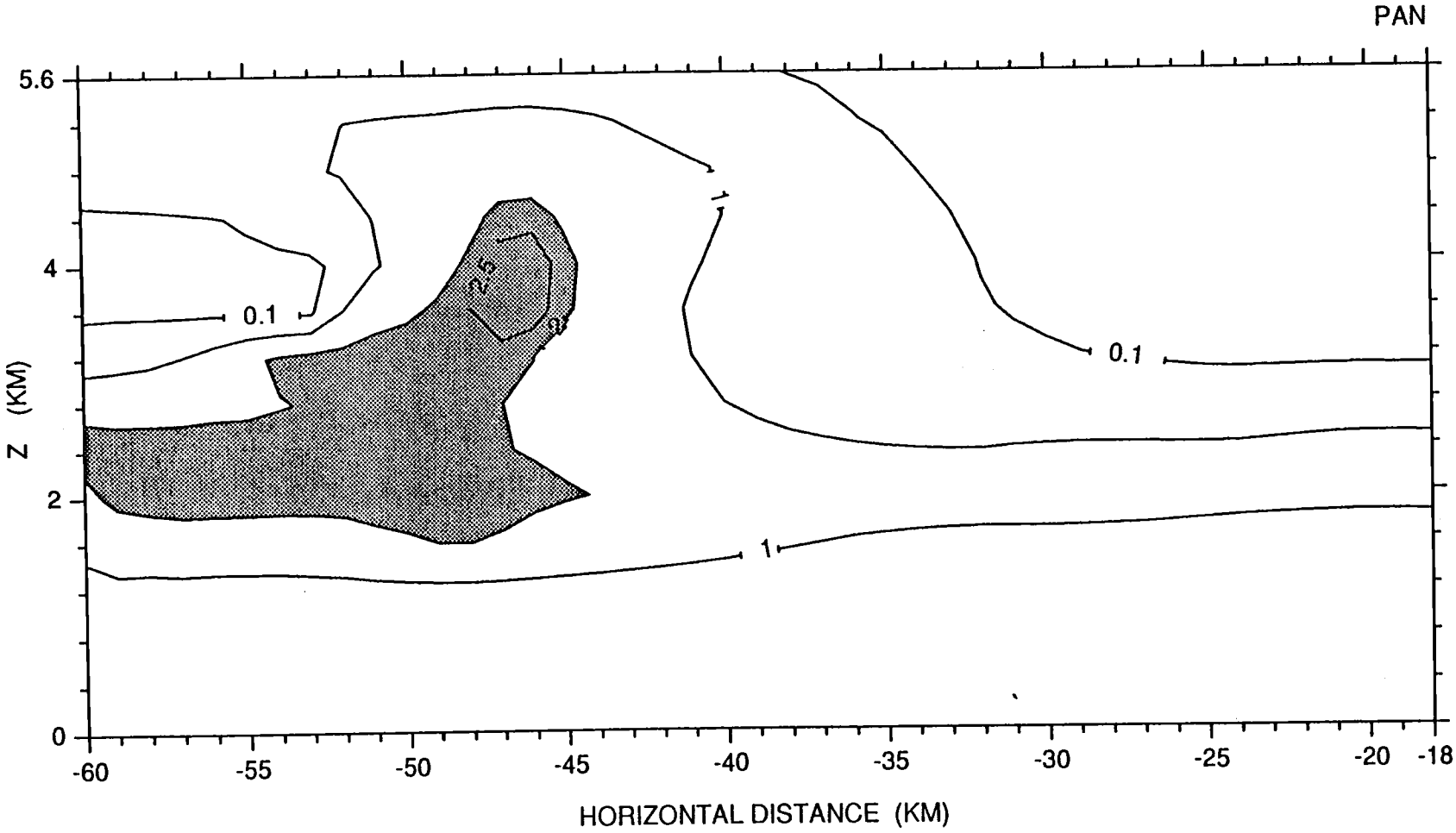

Fig. 5.20 Mixing ratio of PAN for the background simulation. Units are 10^{-10} g g^{-1}.

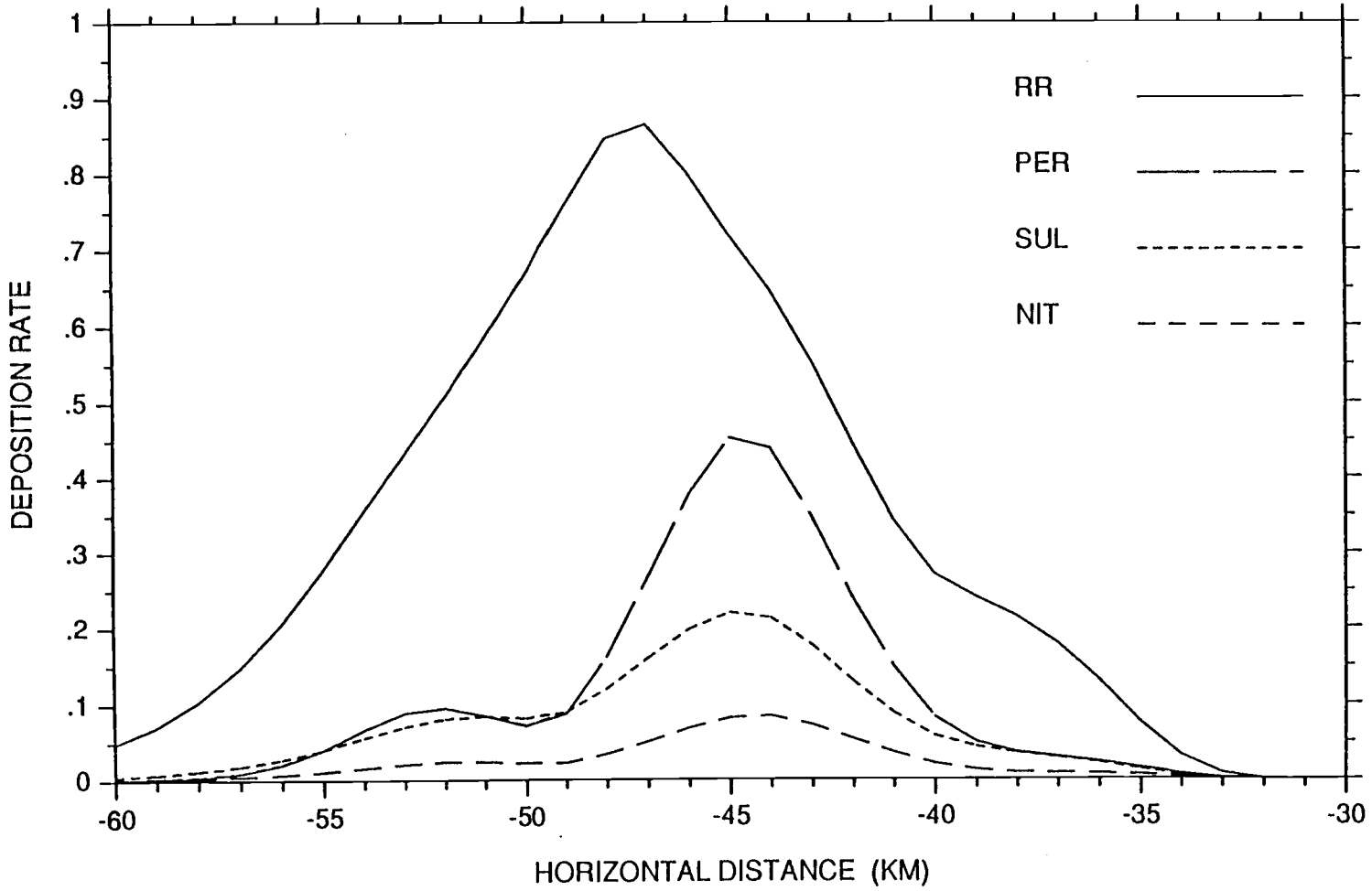

Fig. 5.21 Wet deposition rates for sulfate (SUL), nitrate (NIT), and H_2O_2 (PER) with the precipitation rate (RR) included. Units for sulfate, g hr^{-1} cm^{-1}(transverse to the direction of propagation); nitrate and H_2O_2,10^{-1} g hr^{-1} cm^{-1}. Precipitation rate is in cm hr^{-1}.

maximum (cf. Figs. 5.12-5.14). The precipitation maximum at the surface is associated with this low-level snow maximum, where the collection of cloudwater is a maximum (cf. Fig. 5.2). However, this cloudwater is more dilute than that at the leading edge of the second snow cell. Consequently, the peak deposition rate of the chemical species occurs before the precipitation maximum at the surface.

Another area of interest is the precipitation system's effect on vertical transport of the chemical species. This can be examined by comparing the initial profile of the chemical species to the domain-averaged equilibrium profile. Such comparitive profiles, for SO_2, particulate sulfate, particulate nitrate, and H_2O_2 are shown in Fig. 5.22 (A-D). Sulfur dioxide is seen to have net upward transport above 2 km because of vertical advection and the fact that scavenging of SO_2 by cloudwater was not effective. Particulate sulfate and nitrate show net upward transport above 3.2 km as a result of the stagnant area centered at x=-35. Sulfate also shows a significant increase below 2 km due to in-cloud production and subsequent evaporation. H_2O_2 has a more complex structure with net depletion occurring above 4.2 km and between 1.8 and 3.2 km. These depletions are the result of in-solution reactions with SO_2. The increase between 3.2 and 4.2 km corresponds to the stagnation area, whereas the increase below 1.8 km results from rainwater evaporation.

This concludes the summary of the background simulation. A more detailed look at the pollutant scavenging mechanisms operating in this simulation, for the sulfur chemistry in particular, will be undertaken in the next chapter.

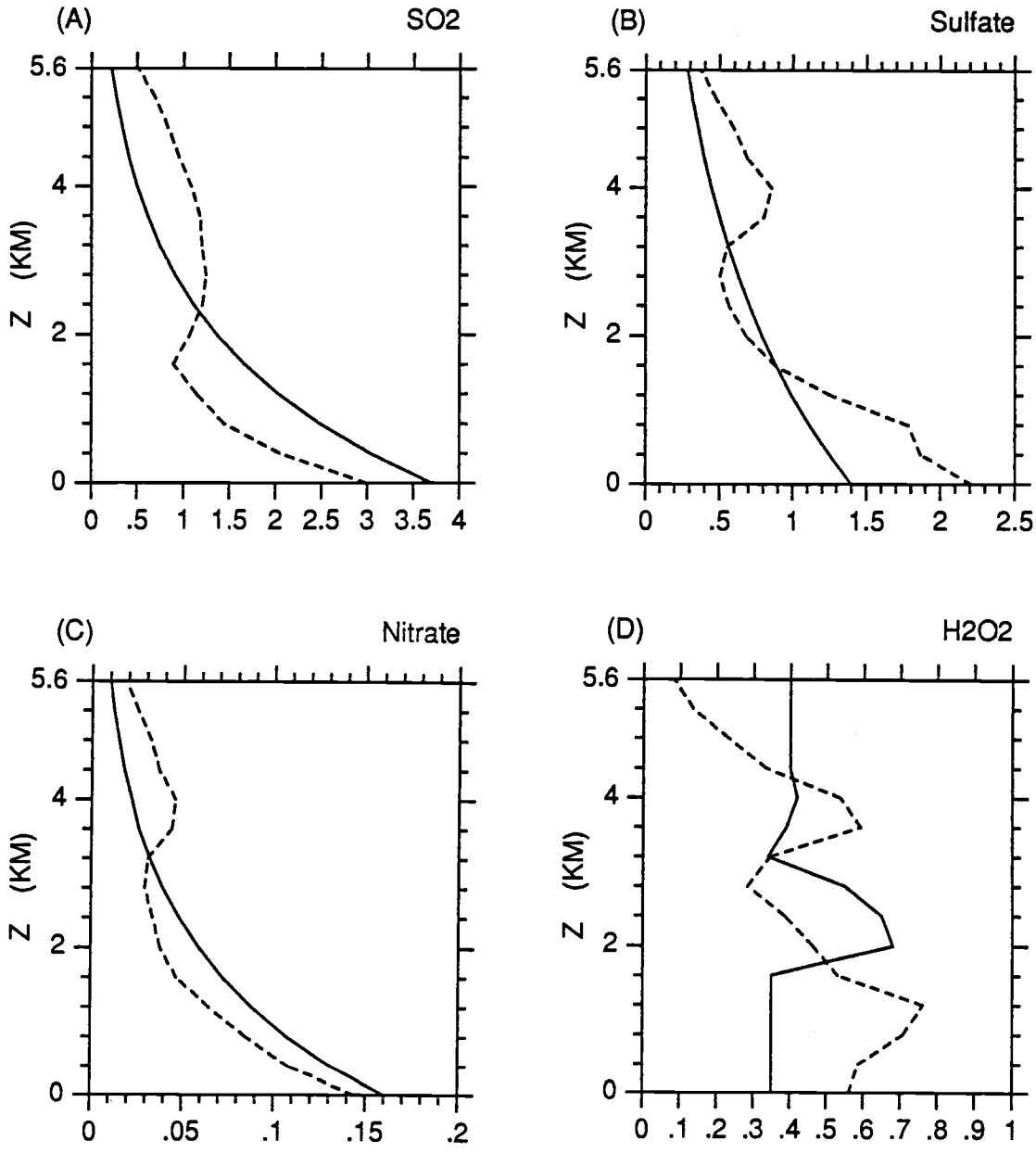

5.22 Vertical profiles of chemical species at initialization (solid line) and at equilibrium (dashed line) for the background simulation, a) SO_2, b) particulate sulfate, c) particulate nitrate, and d) H_2O_2. Units are 10^{-9} g g^{-1}.

6. SENSITIVITY STUDIES AND COMPARISONS WITH OBSERVATIONS

In the first section of this chapter the pollutant scavenging mechanisms active in the background simulation will be further investigated through the use of sensitivity studies (i.e. model simulations in which various scavenging mechanisms are selectively eliminated). The second section will compare the model results with available *in situ* observations.

6.1 Sensitivity Studies

The sensitivity studies investigated the roles of in-solution oxidation of SO_2 and nucleation scavenging of particulate sulfate to determine their relative contributions to the sulfur chemistry of the background simulation. Table 6.1 lists the various model simulations and the parameter changes made. These cases will be addressed individually at first and then collectively as they relate to the background simulation.

The fields of particulate sulfate and SO_2 for case 2 (ozone=0) are shown in Figs. 6.1 and 6.2, respectively. As these fields show, case 2 is very similar to the background simulation (case 1, cf. Figs. 5.6 and 5.19). The particulate sulfate field remains essentially unchanged. However, SO_2 for case 2 shows slight, but not insignificant, increases over case 1 SO_2 through most of the model domain, with one exception corresponding to the leading edge of the cloudwater field (cf. Fig. 5.1) where case 1 SO_2 concentrations are slightly higher. These differences imply that oxidation by ozone is most active (depletes most SO_2) in the main upper-level cloudwater mass, not at the leading edge. This is verified by comparing the sulfate-in-cloudwater fields of case 1 (cf Fig.5.9) and case 2 (shown in Fig. 6.3). With oxidation by ozone disabled, the

Table 6.1. Model simulations discussed in this paper

Case #	Changes
1	background
2	O_3=0
3	H_2O_2=0
4	O_3=H_2O_2=0
5	nuc. scav. =0

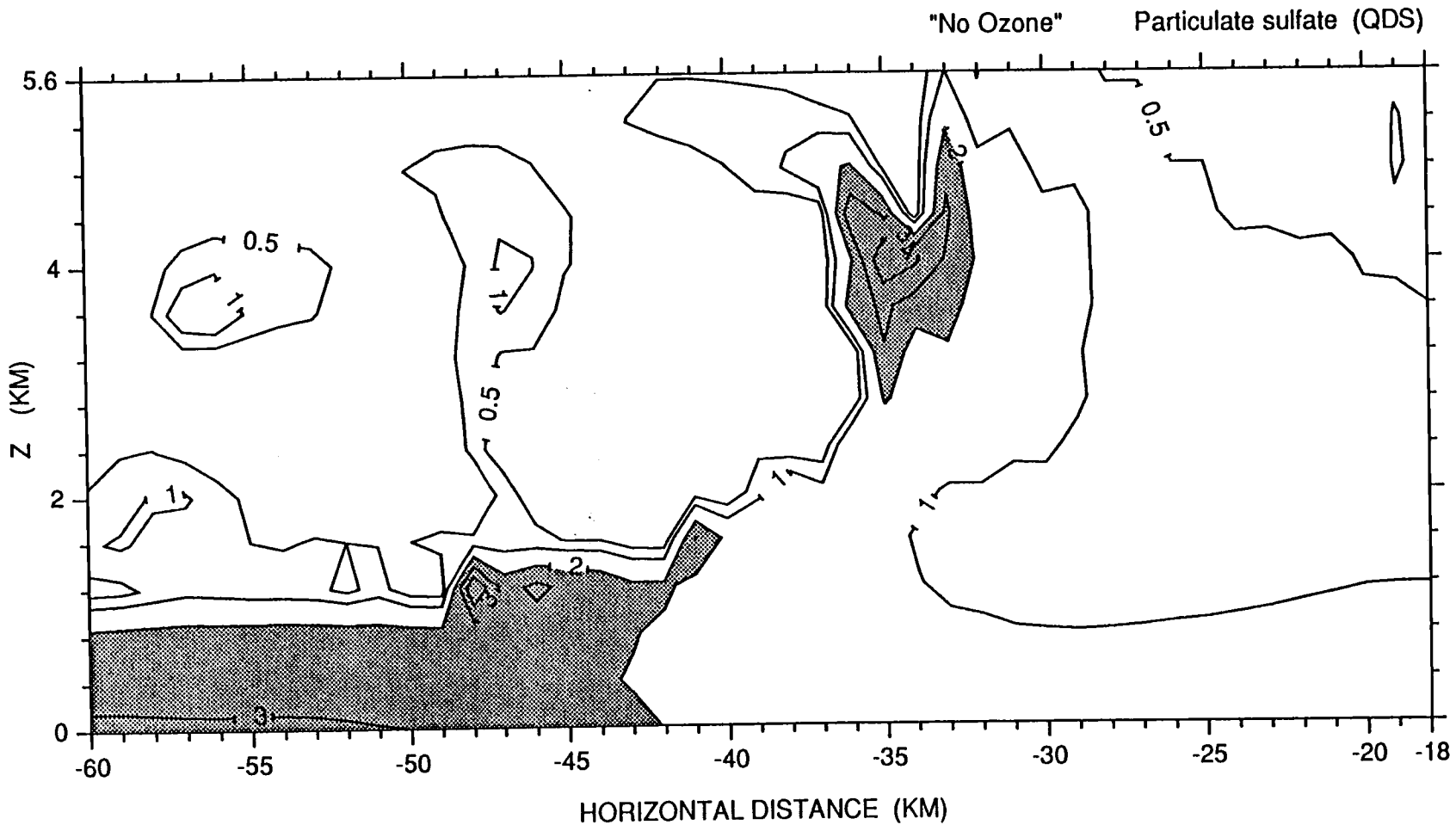

Fig. 6.1 Mixing ratio of particulate sulfate for the case 2 simulation. Units are 10^{-9}g g^{-1}.

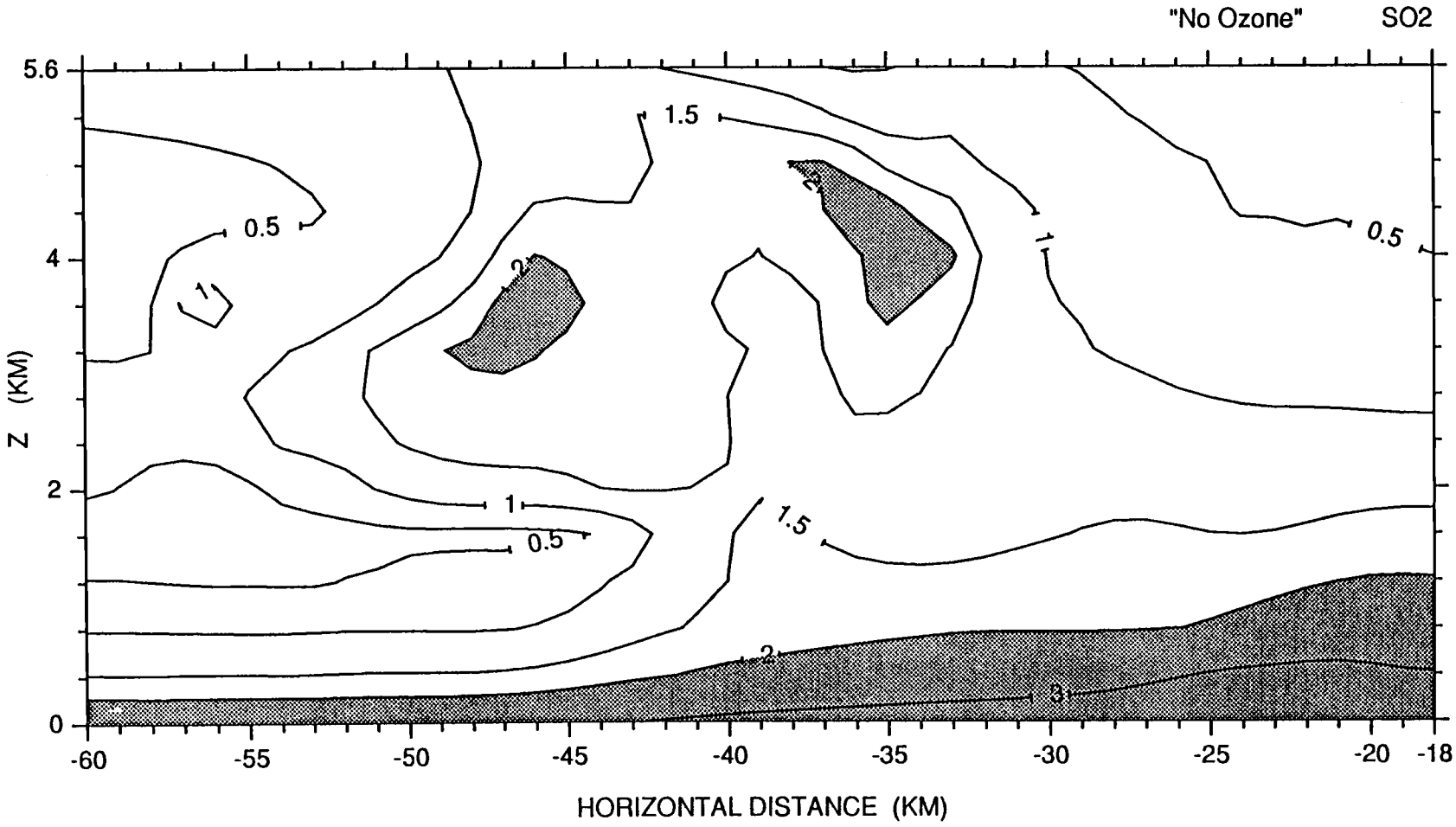

Fig. 6.2 Mixing ratio of SO_2 for the case 2 simulation. Units are 10^{-9}g g^{-1}.

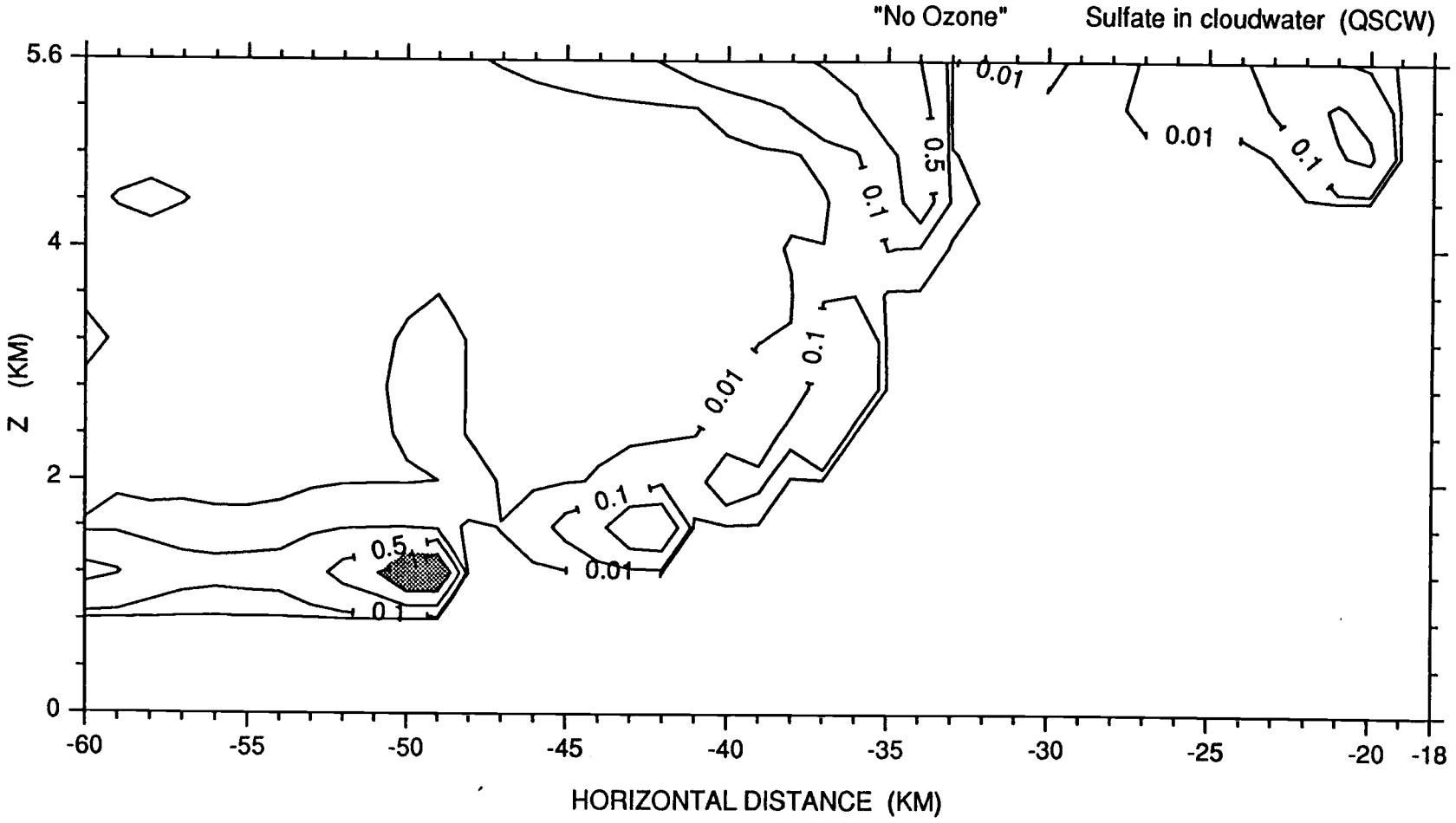

Fig. 6.3 Mixing ratio of sulfate-in-cloudwater for the case 2 simulation. Units are 10^{-9}g g^{-1}.

sulfate-in-cloudwater field is diminished in the region above 2 km between x=-39 and x=-47. The case 2 fields of sulfate-in-snow and sulfate-in-rain are shown in Figs. 6.4 and 6.5, respectively. In comparison with case 1 (cf. Figs. 5.13 and 5.16), Figs. 6.4 and 6.5 show the small, yet significant, effects of ozone oxidation.

The elimination of hydrogen peroxide oxidation has a much more profound effect on the sulfur chemistry. Fig. 6.6 shows the case 3 particulate sulfate field. To the right of x=-39 the structure is unchanged from case 1. At low levels, where evaporation is important, there is much less sulfate present. Obviously, there is less sulfate available to be evaporated because of lack of in-cloud production. Shown in Fig. 6.7 is the case 3 SO_2 field. This field is very flat with upper level values much lower than in the background simulation (cf. Fig. 5.19). This implies that dissolution of SO_2 is facilitated when oxidation by H_2O_2 is not present. To understand this apparent paradox the case 3 pH field (shown in Fig. 6.8) needs to be examined. At upper levels, the pH is higher (less acidic) than that of case 1 (cf Fig. 5.18). Dissolution of SO_2 into liquid hydrometeors is decreased as the acidity of these hydrometeors is increased. And because cloudwater contents are low, the cloud of case 1 acidifies more quickly (as compared with case 3), thereby preventing the absorption of SO_2 into the cloudwater mass. Consequently, the case 1 SO_2 field primarily represents advective processes.

The case 3 fields for sulfate-in-cloudwater, sulfate-in-snow, and sulfate-in-rain are shown in Figs. 6.9-6.11, respectively. Generally, they all show the same structure as their case 1 counterparts (this is to be expected given the interdependence of these fields with their parent hydrometeor fields),

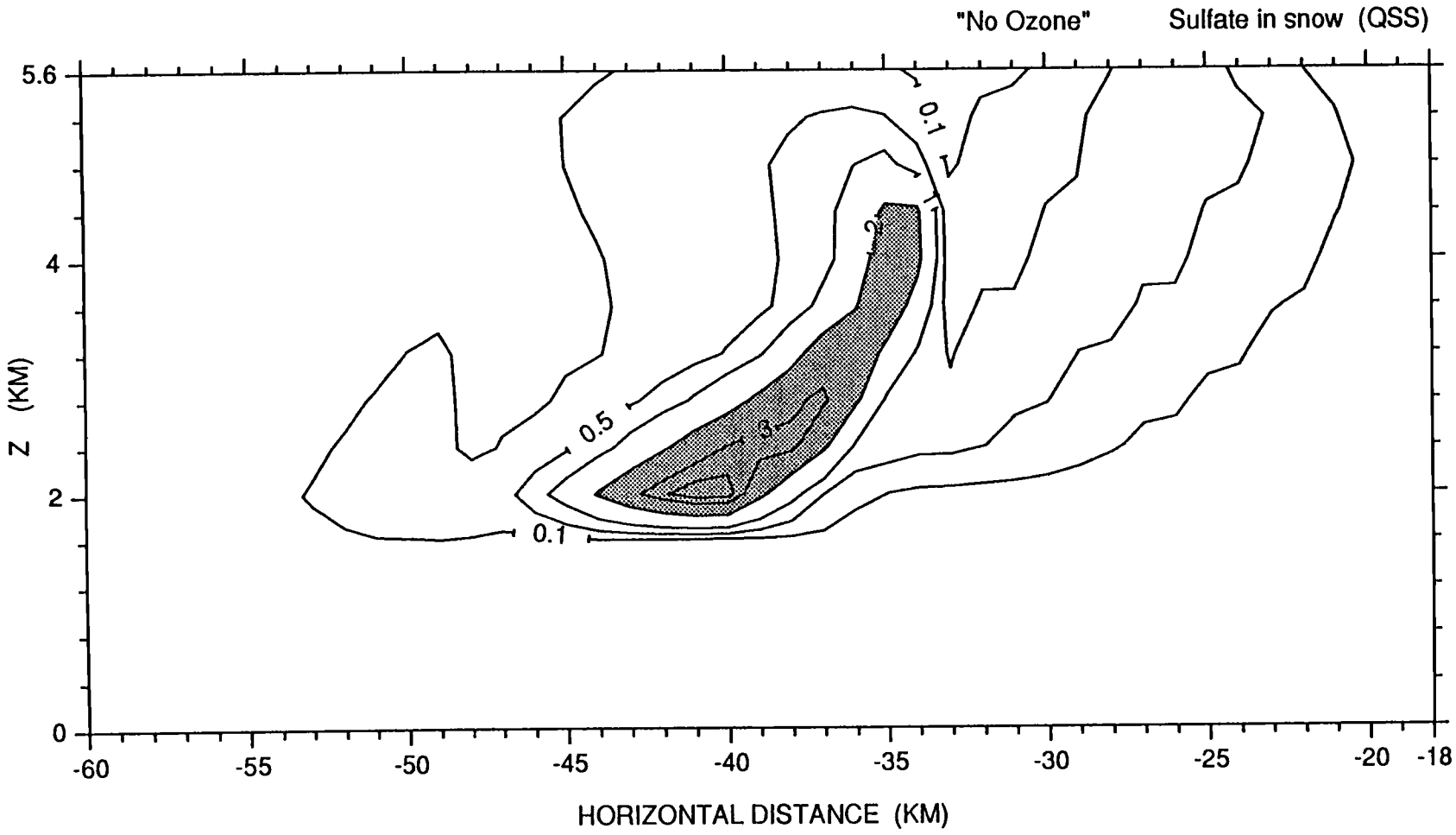

Fig. 6.4 Mixing ratio of sulfate-in-snow for the case 2 simulation. Units are 10^{-9}g g^{-1}.

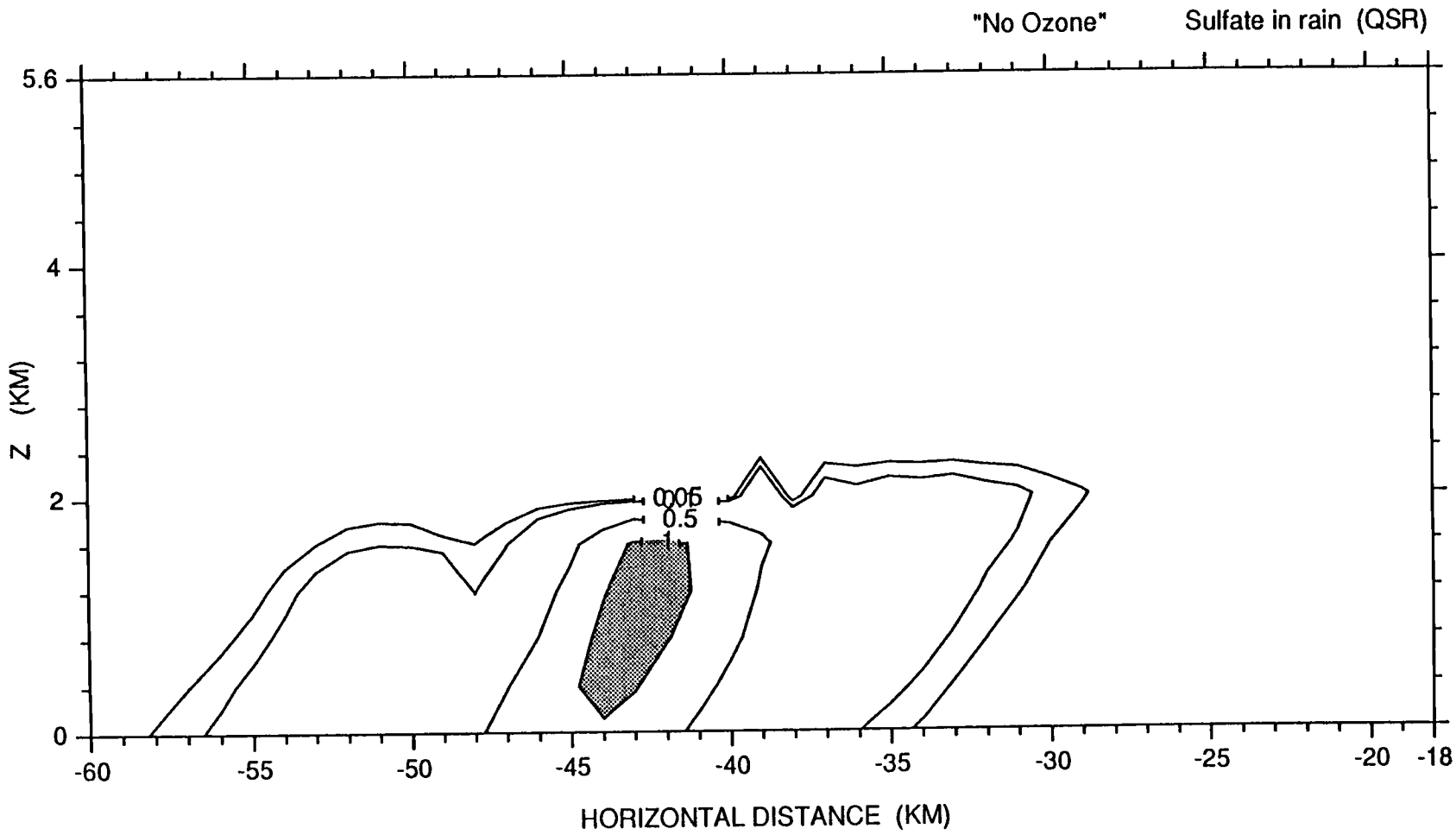

Fig. 6.5 Mixing ratio of sulfate-in-rain for the case 2 simulation. Units are 10^{-9}g g^{-1}.

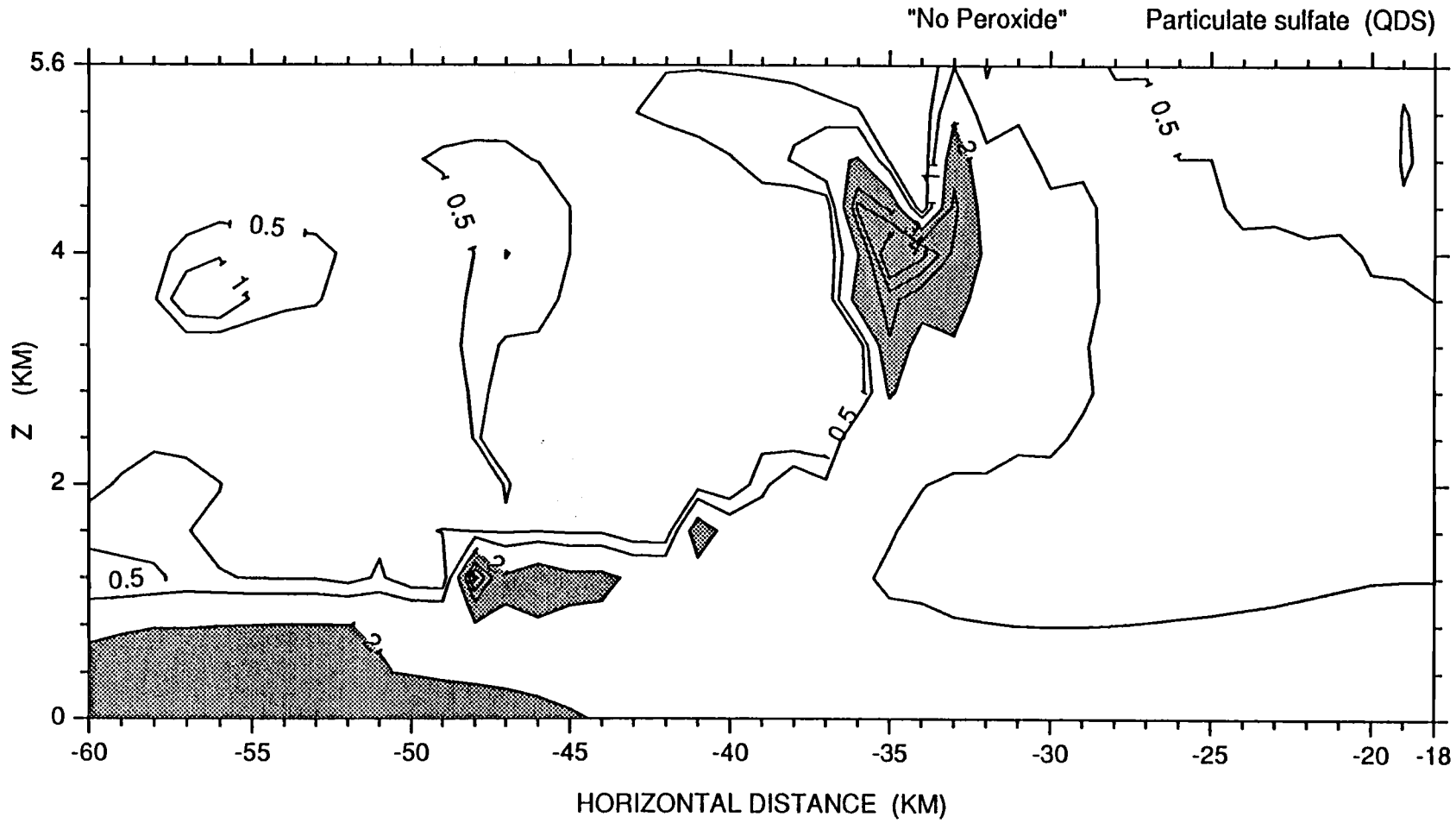

Fig. 6.6 Mixing ratio of particulate sulfate for the case 3 simulation. Units are 10^{-9}g g^{-1}.

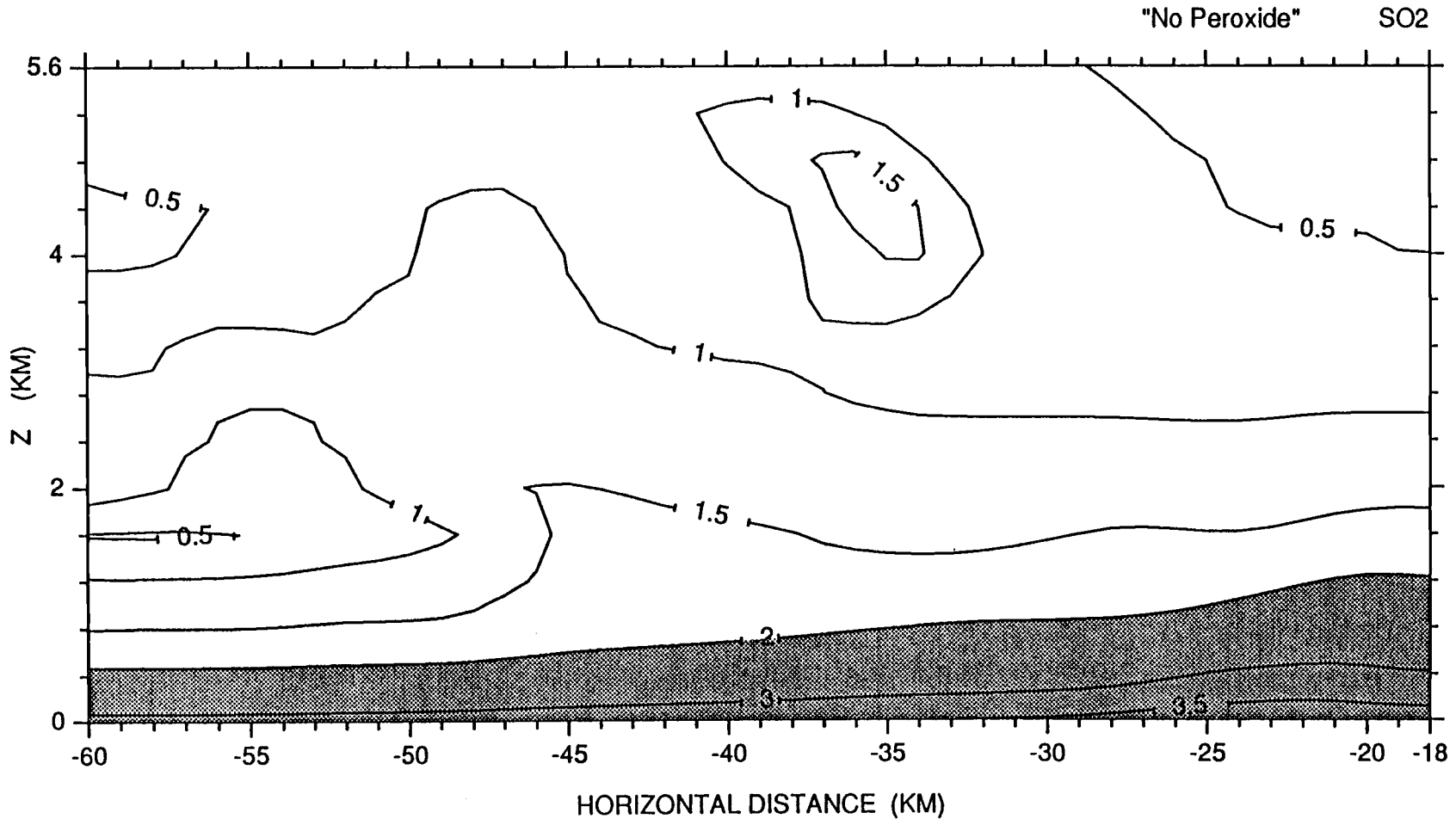

Fig. 6.7 Mixing ratio of SO_2 for the case 3 simulation. Units are 10^{-9}g g^{-1}.

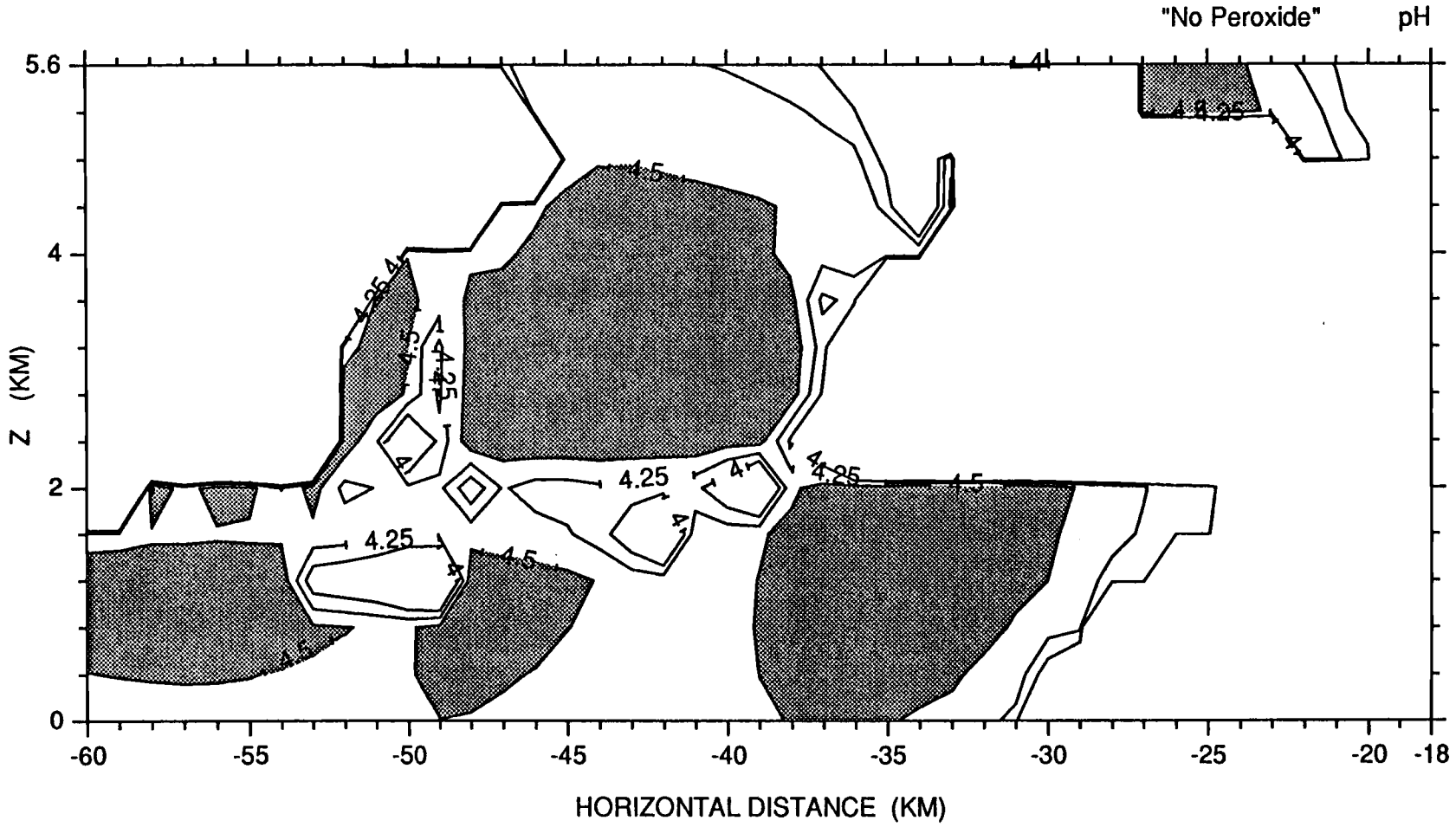

Fig. 6.8 pH for the case 3 simulation. Areas greater than 4.5 are shaded.

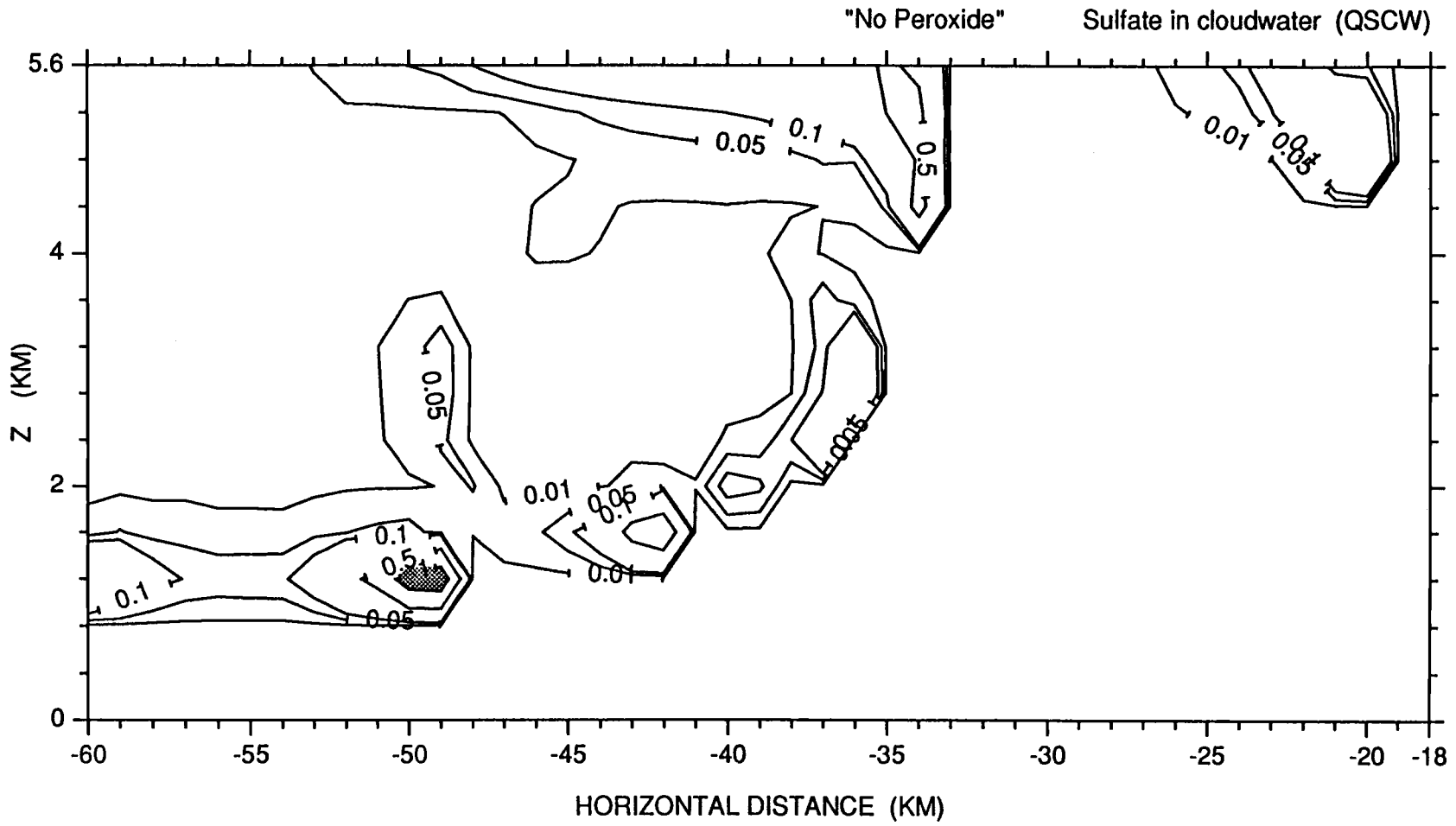

Fig. 6.9 Mixing ratio of sulfate-in-cloudwater for the case 3 simulation. Units are 10^{-9}g g^{-1}.

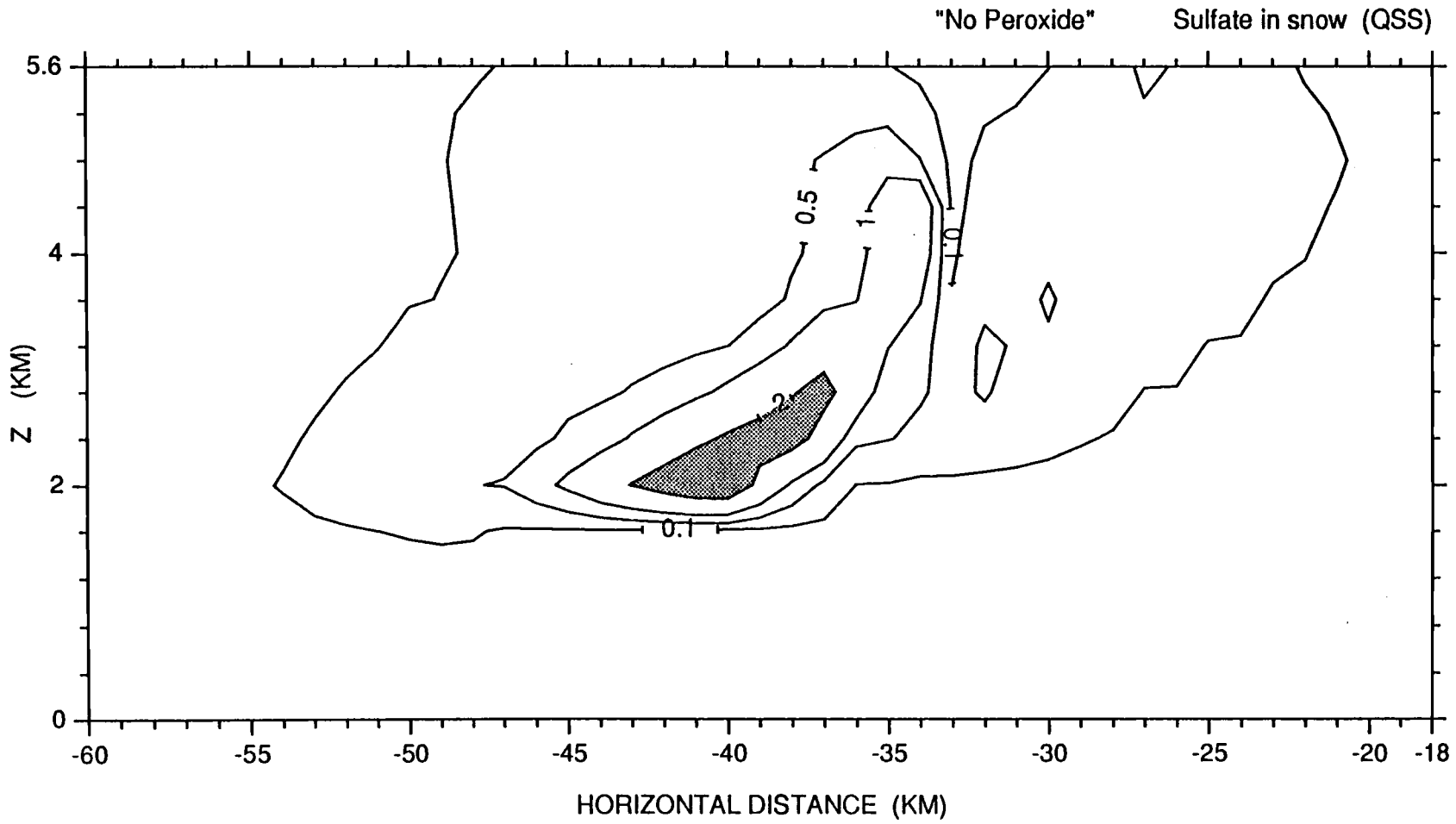

Fig. 6.10 Mixing ratio of sulfate-in-snow for the case 3 simulation. Units are 10^{-9}g g^{-1}.

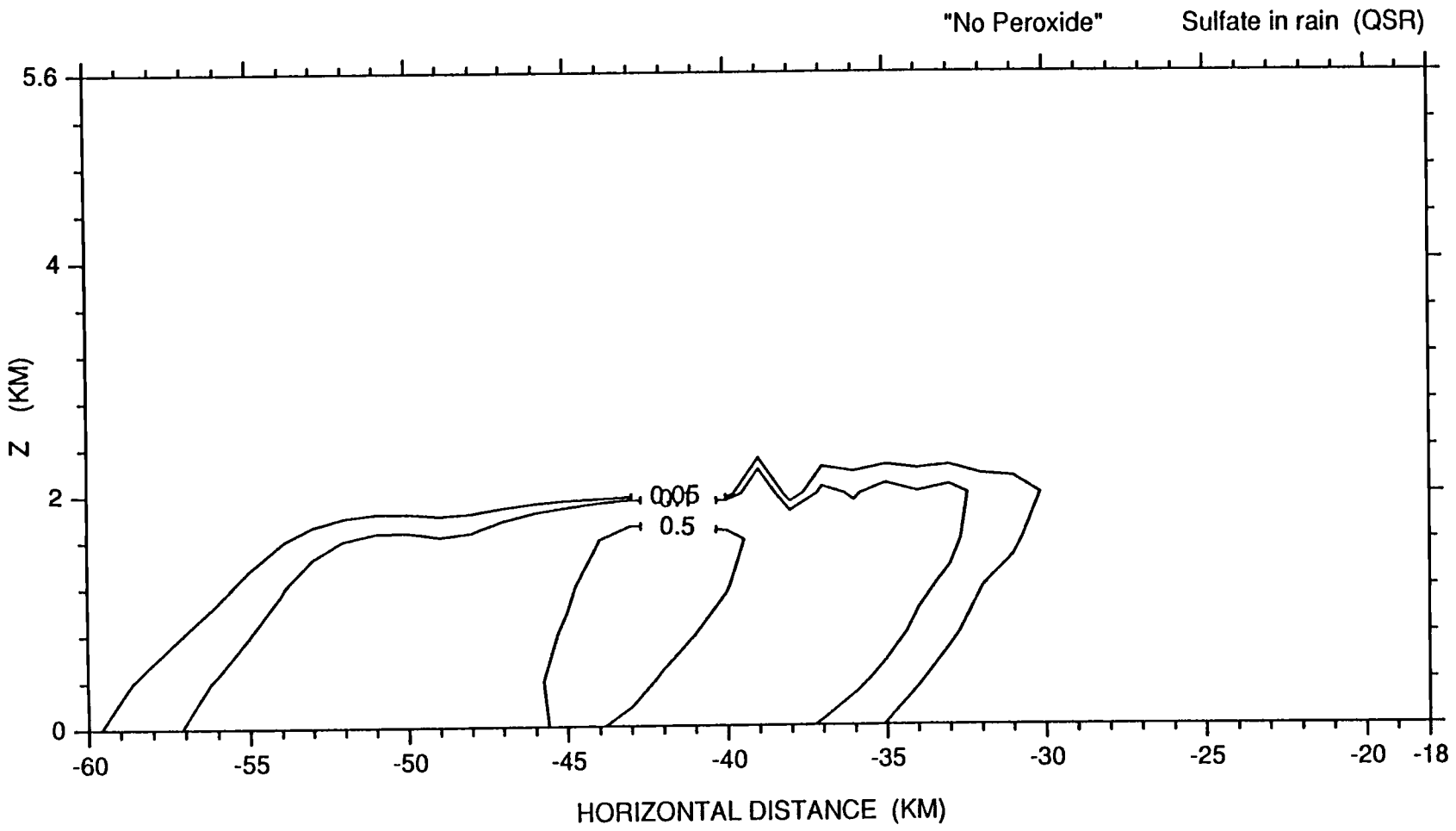

Fig. 6.11 Mixing ratio of sulfate-in-rain for the case 3 simulation. Units are 10^{-9}g g^{-1}.

but quantitatively, values of are much lower. Interestingly, the back portions of the sulfate-in-snow and the sulfate-in-rain fields remain virtually unchanged, as these areas correspond to the regions of ozone oxidation. (The rapid depletion of H_2O_2 resulting from reaction with SO_2 enables ozone to be the primary oxidant in the back portion of the liquid water fields).

The simulation with no oxidation is considered in case 4. Fig. 6.12 shows the particulate sulfate field and Fig. 6.13 shows the SO_2 field for case 4. Once again the particulate sulfate field remains unchanged to the right of x=-39. In the lower-level evaporative area there is very little sulfate, as a result of no in-cloud production. The case 4 SO_2 field shows little lower level depletion with upper levels values much less than the background simulation. Somewhat surprisingly, there is more SO_2 aloft than in case 3, where oxidation only by ozone was present. The explanation for this is that oxidation by ozone partially depleted the case 3 SO_2 field before the acidity levels in the cloudwater prohibited any further dissolution of SO_2.

The sulfate-in-cloudwater, sulfate-in-snow, and sulfate-in-rain fields for case 4 are shown in Figs. 6.14-6.16, respectively. Without any oxidation mechanisms present these fields represent the effects of nucleation scavenging alone (impaction scavenging is negligible). Perhaps the most interesting of these fields is that of sulfate-in-rain (Fig. 6.16). At the onset of the precipitation, the sulfate content is slightly irregular (i.e. discontinuous) and there is a notch at x=-48. The explanation for this is as follows. The leading edge of the precipitation is associated with the snow produced in the upper-level generating region. In this region the depositional growth of snow prevented the effects of both oxidation of SO_2 and nucleation scavenging. This relatively

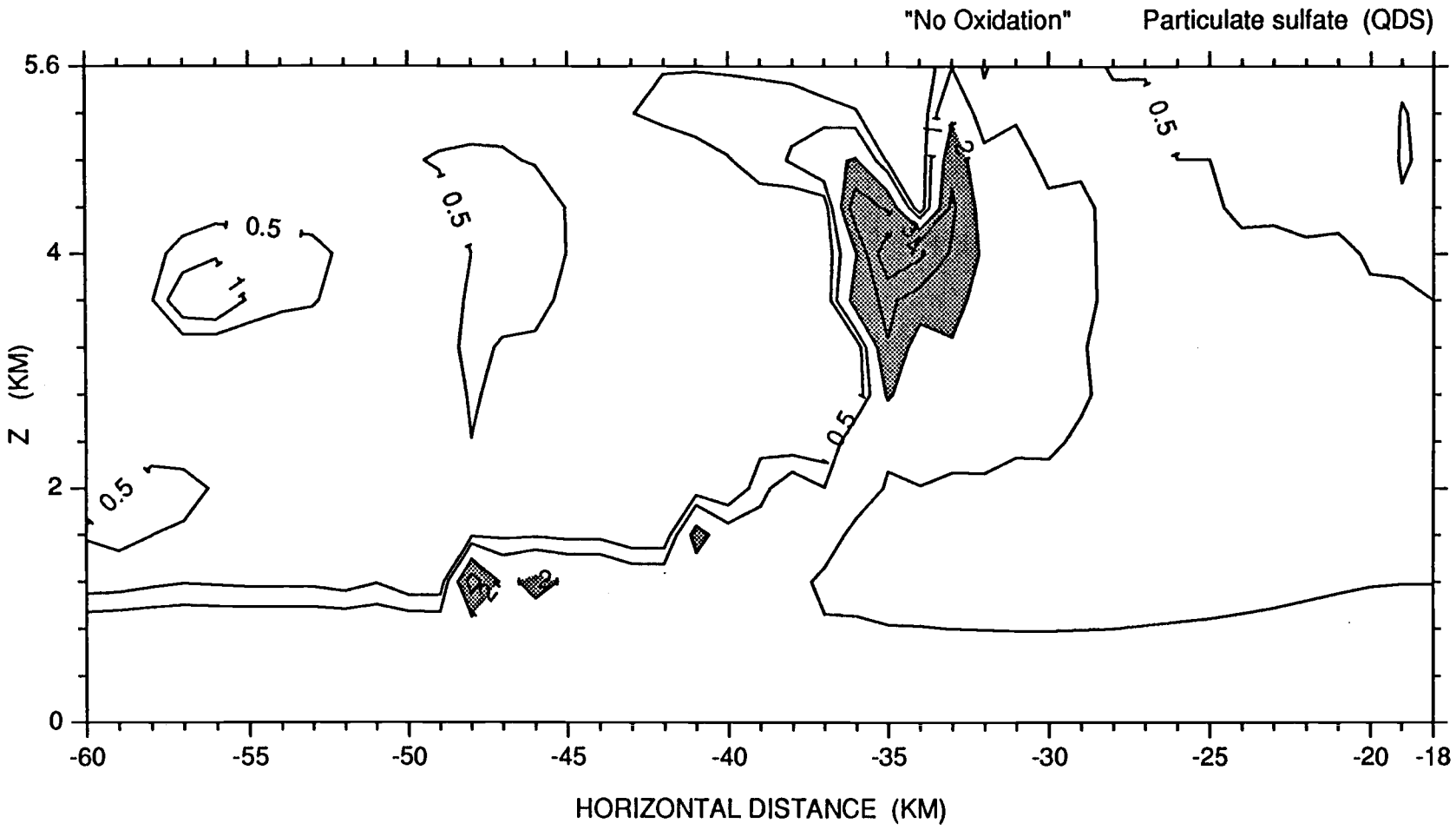

Fig. 6.12 Mixing ratio of particulate sulfate for the case 4 simulation. Units are 10^{-9}g g^{-1}.

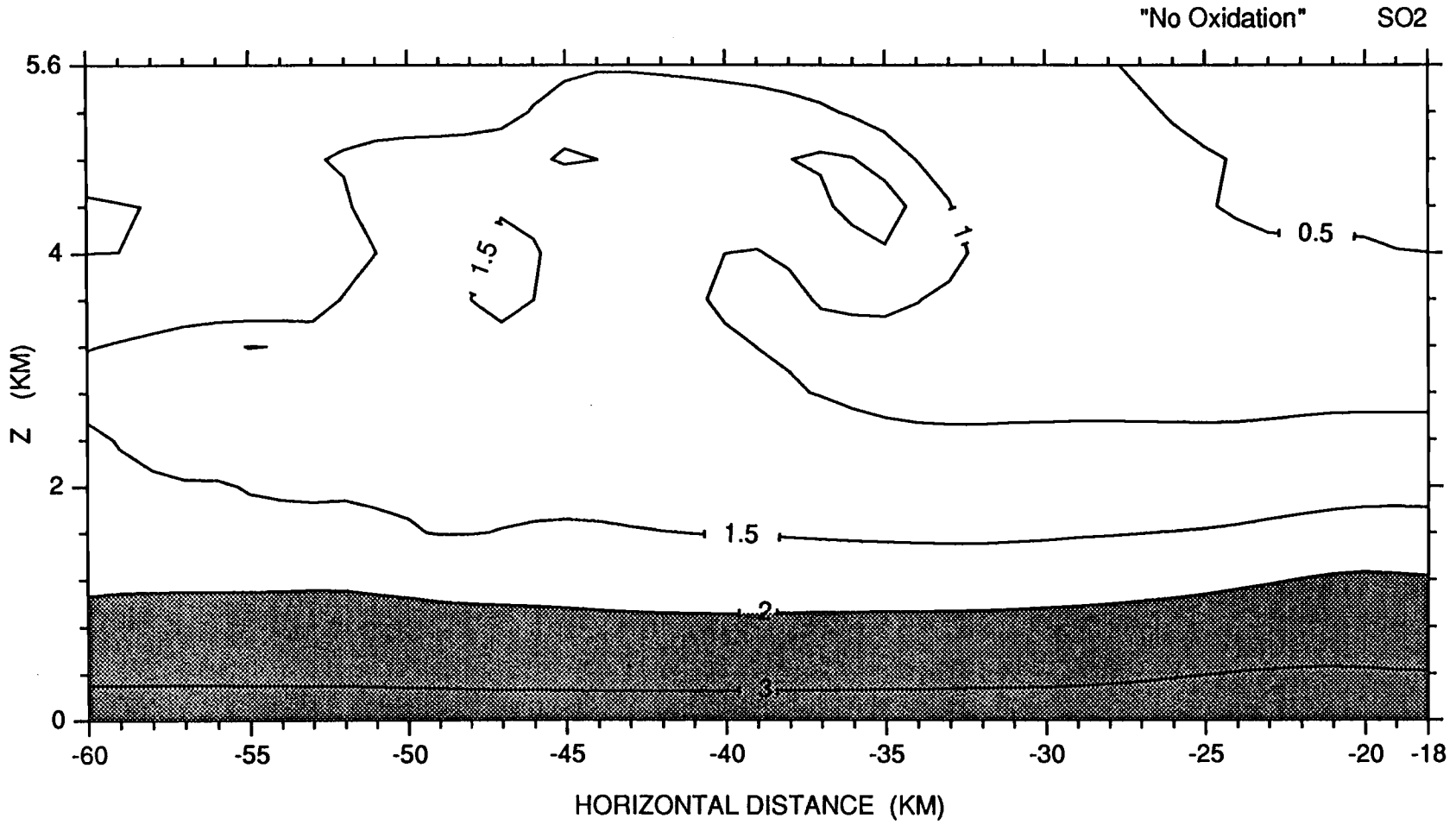

Fig. 6.13 Mixing ratio of SO_2 for the case 4 simulation. Units are 10^{-9}g g^{-1}.

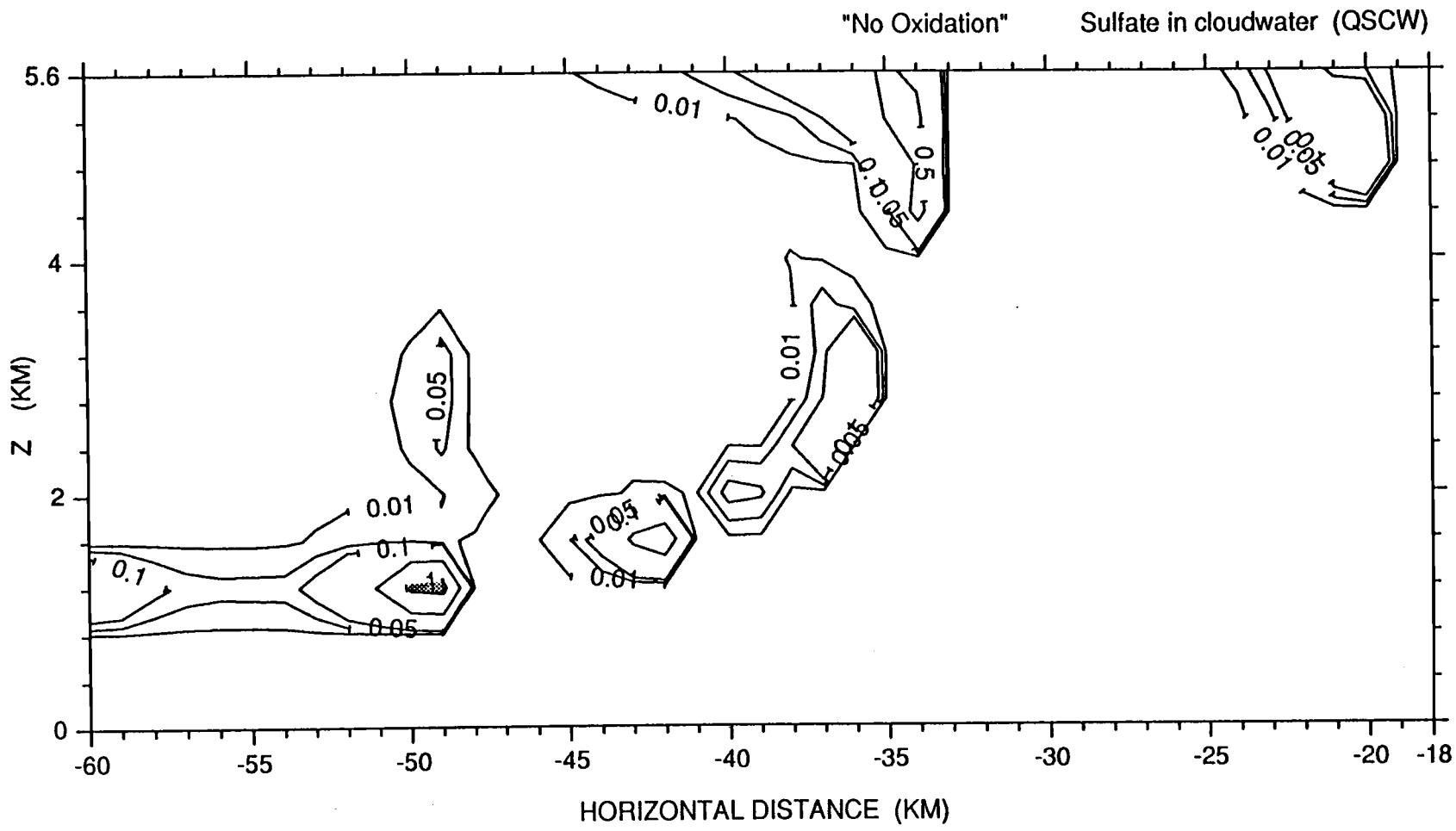

Fig. 6.14 Mixing ratio of sulfate-in-cloudwater for the case 4 simulation. Units are 10^{-9}g g^{-1}.

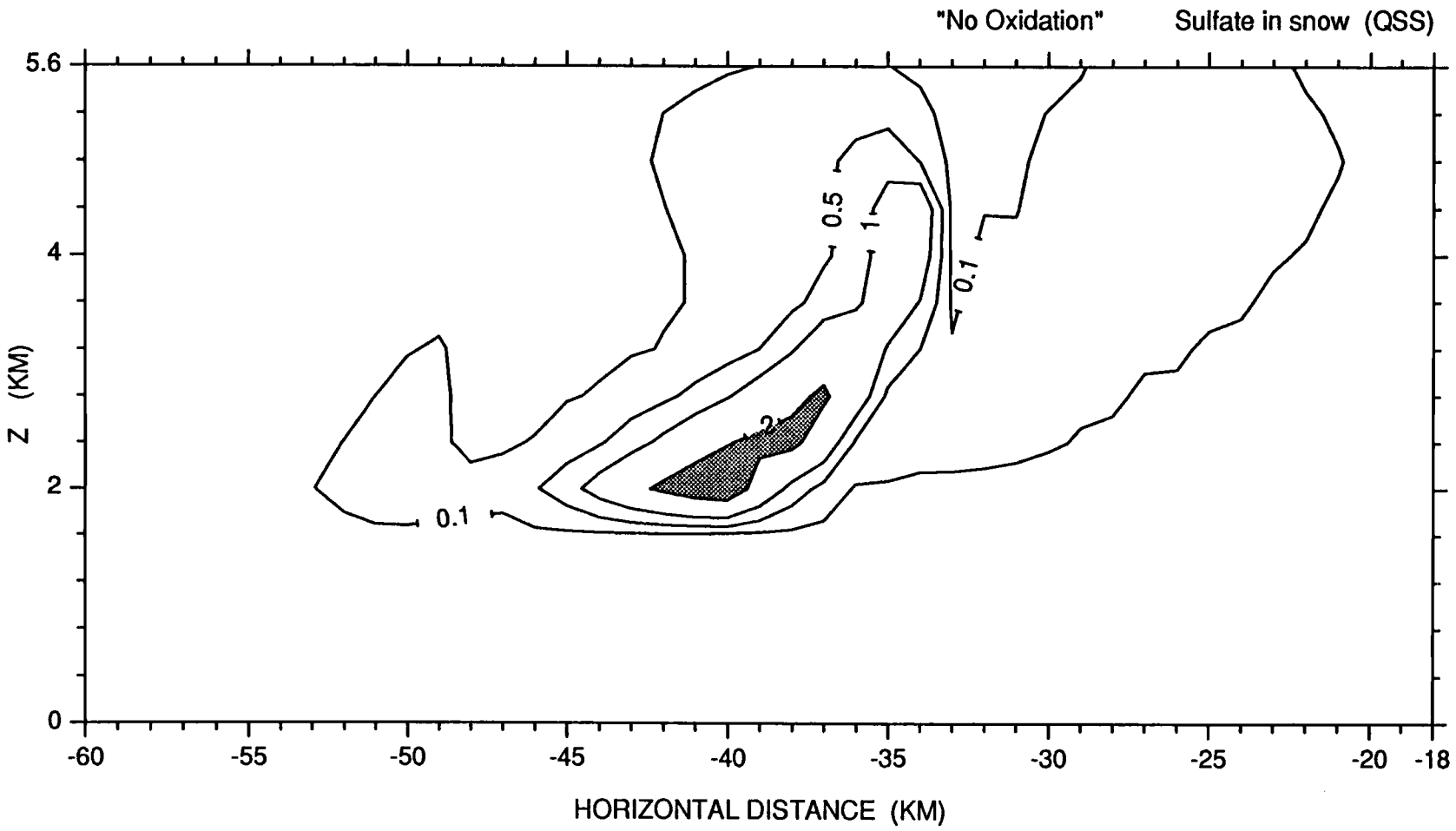

Fig. 6.15 Mixing ratio of sulfate-in-snow for the case 4 simulation. Units are 10^{-9}g g^{-1}.

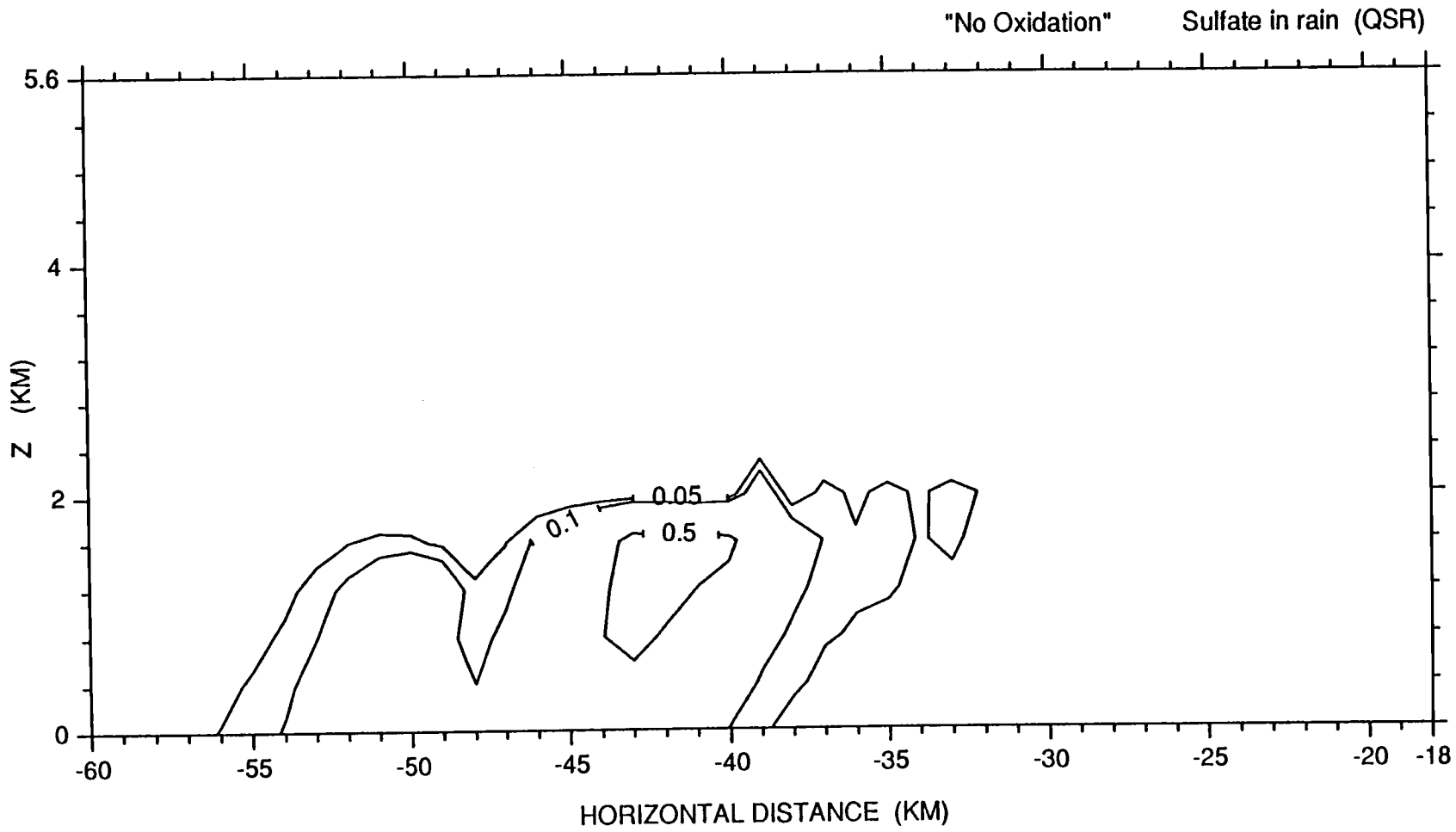

Fig. 6.16 Mixing ratio of sulfate-in-rain for the case 4 simulation. Units are 10^{-9}g g^{-1}.

unconcentrated snow melted and fell through a region of relatively high peroxide and SO_2 concentrations. Consequently, the sulfate in the leading edge of the precipitation resulted from oxidation of SO_2 in rain. The notch at x=-48 is a consequence of the fact that nucleation scavenging did not take place between x=-46 and x=-48. Therefore the sulfate-in-rain at the notch resulted from oxidation mechanisms.

The final sensitivity study (case 5) turned off nucleation scavenging. In order to get a better feel for the following results the nucleation scavenging field of the background simulation is given in Fig. 6.17. This field shows the rapidness of particulate chemical species incorporation into the cloud and its limited extent. The shape of the collection area aloft (cf Figs. 5.6, 5.7, 6.12 etc...), centered at x=-35, is readily understood in light of Fig. 6.17.

The fields of particulate sulfate and SO_2 for case 5 are shown in Figs. 6.18 and 6.19, respectively. There is a good deal of particulate sulfate in the lower left quadrant of Fig. 6.18 due to in-cloud production and subsequent evaporation. The only significant incorporation mechanism for particulate sulfate is nucleation scavenging, consequently the upper level structure of Fig. 6.18 is a result of advection. Fig. 6.19 indicates that the SO_2 field is virtually unaffected by the elimination of nucleation scavenging (cf. Fig. 5.19). The fields of sulfate-in-cloudwater, sulfate-in-snow, and sulfate-in-rain for case 5 are shown in Figs. 6.20-6.22, respectively. Interestingly, the values of sulfate-in-cloudwater and sulfate-in-snow are the lowest of any of the simulations. This will be discussed in more detail below.

Now that these sensitivity studies have been individually compared to the background simulation a composite examination is warranted. Most

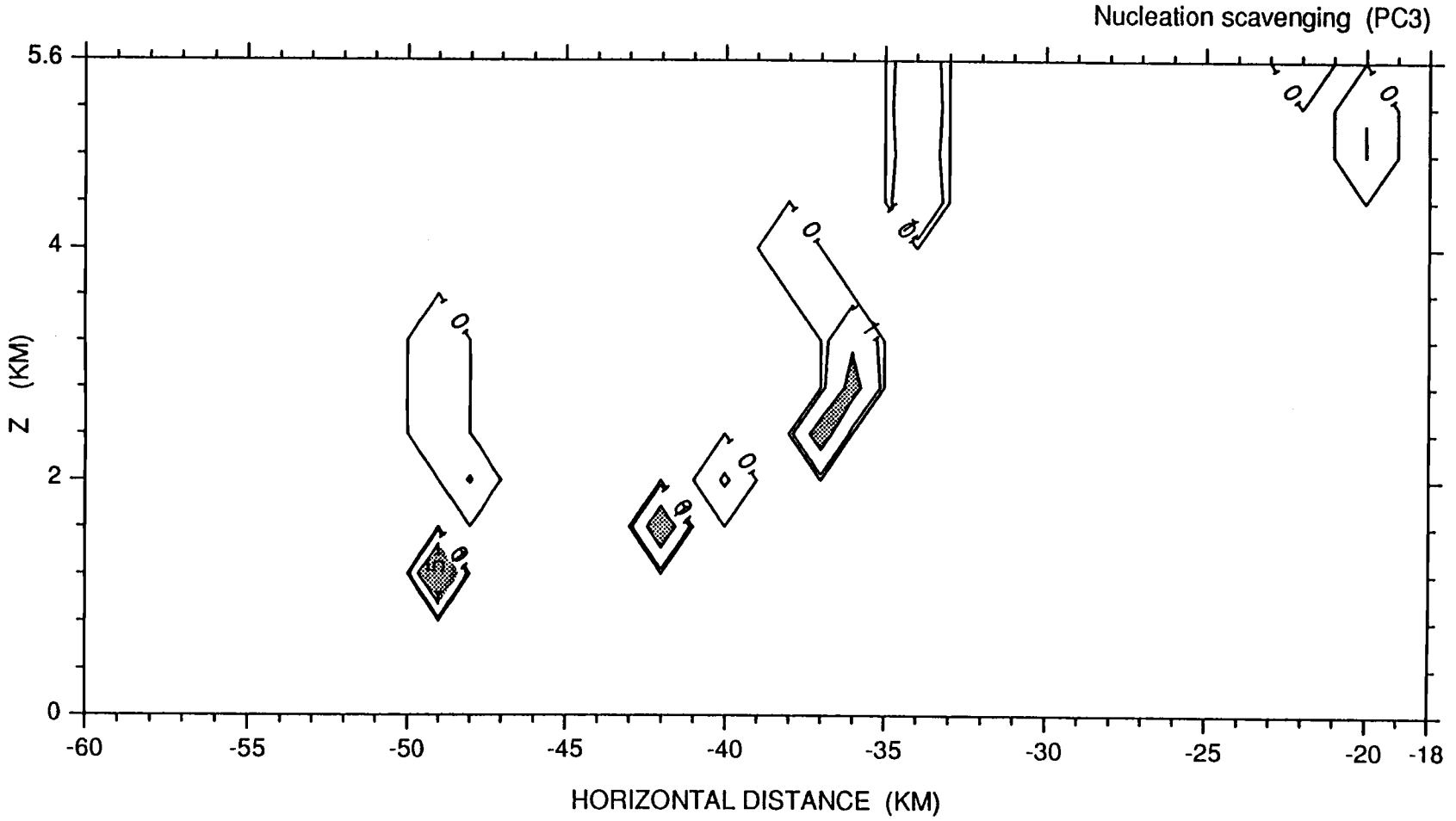

Fig. 6.17 Nucleation scavenging in the background simulation. Units are 10^{-12}g g^{-1}s^{-1}.

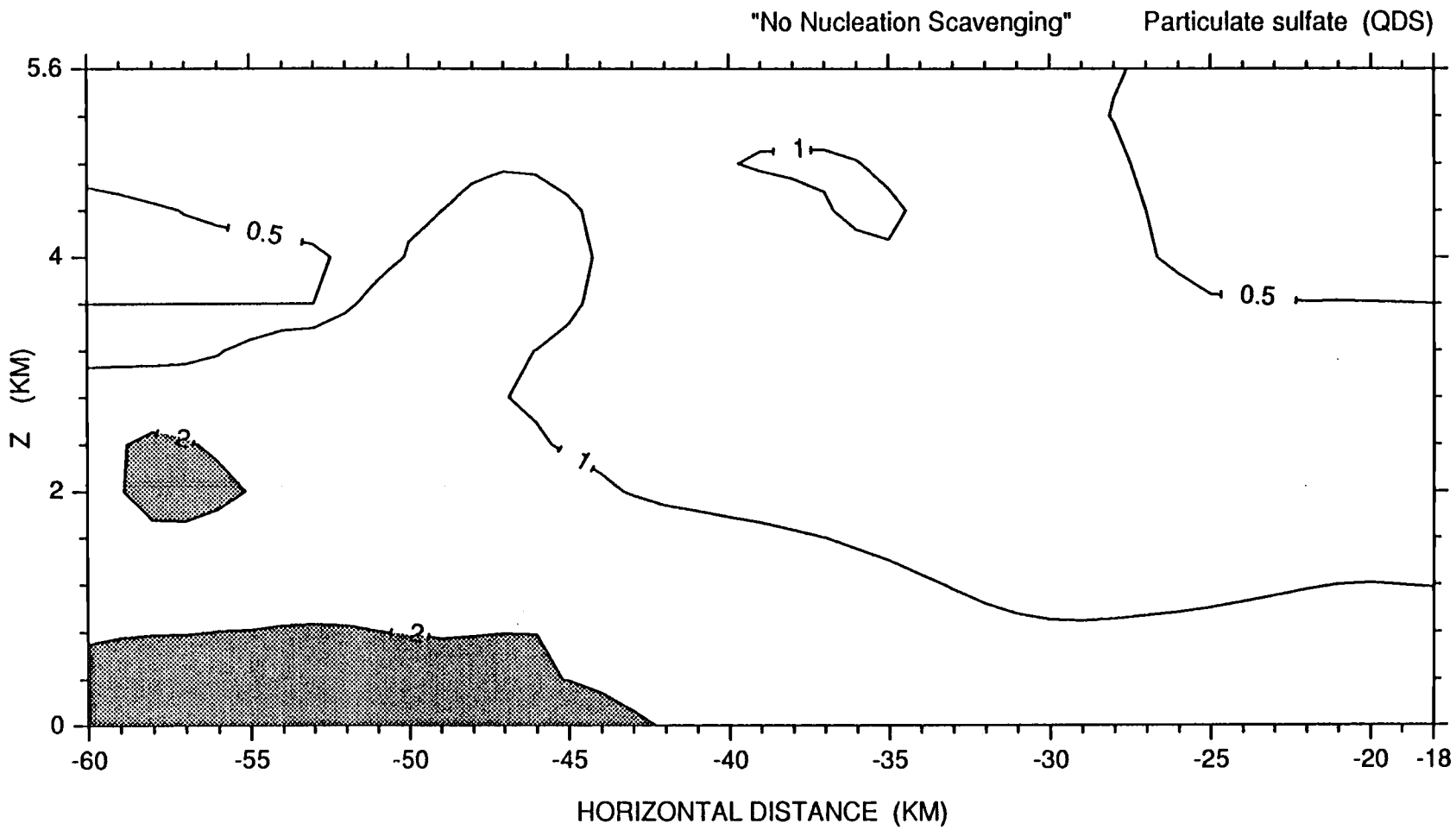

Fig. 6.18 Mixing ratio of particulate sulfate for the case 5 simulation. Units are 10^{-9}g g^{-1}.

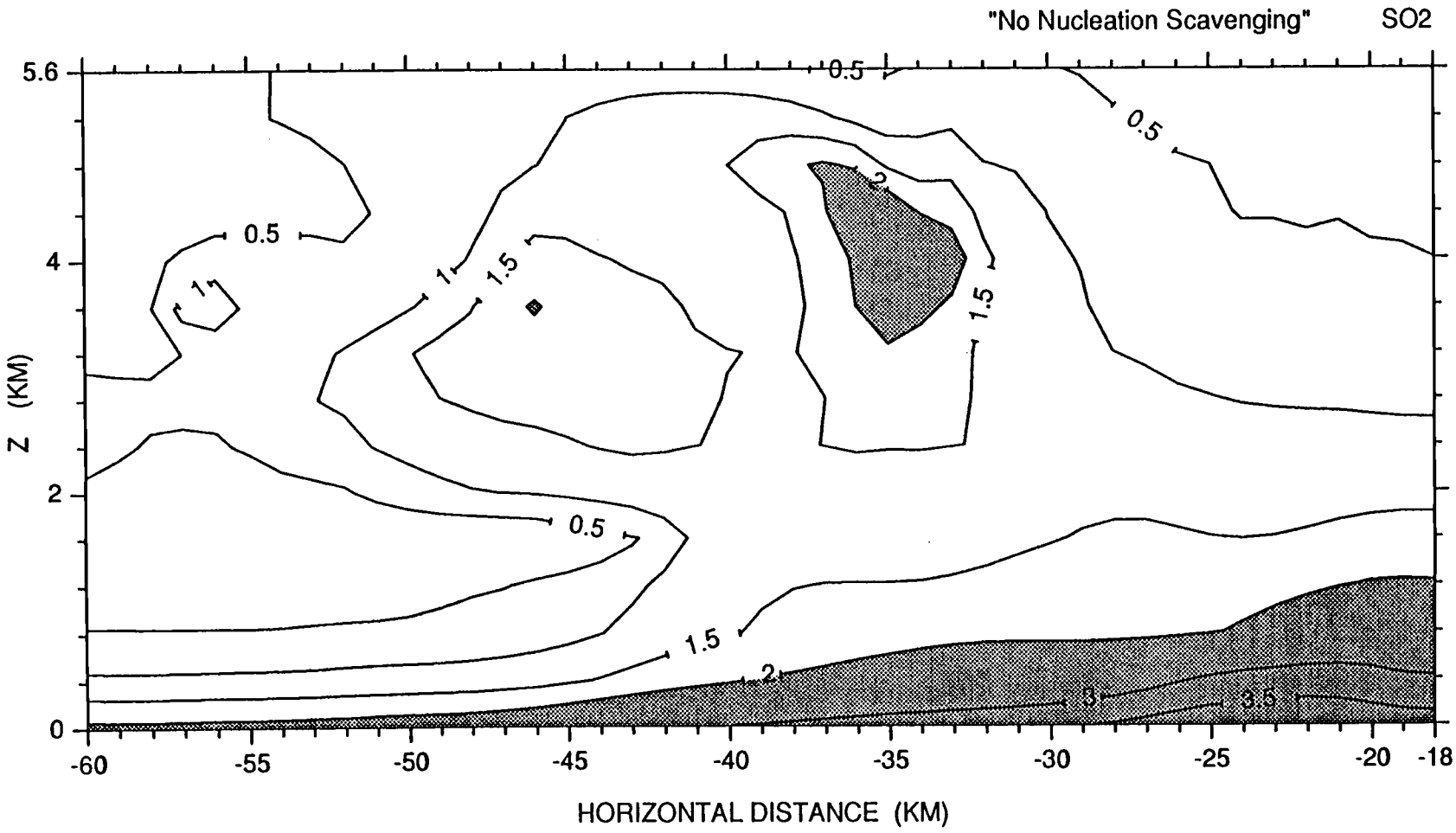

Fig. 6.19 Mixing ratio of SO_2 for the case 5 simulation. Units are 10^{-9}g g^{-1}.

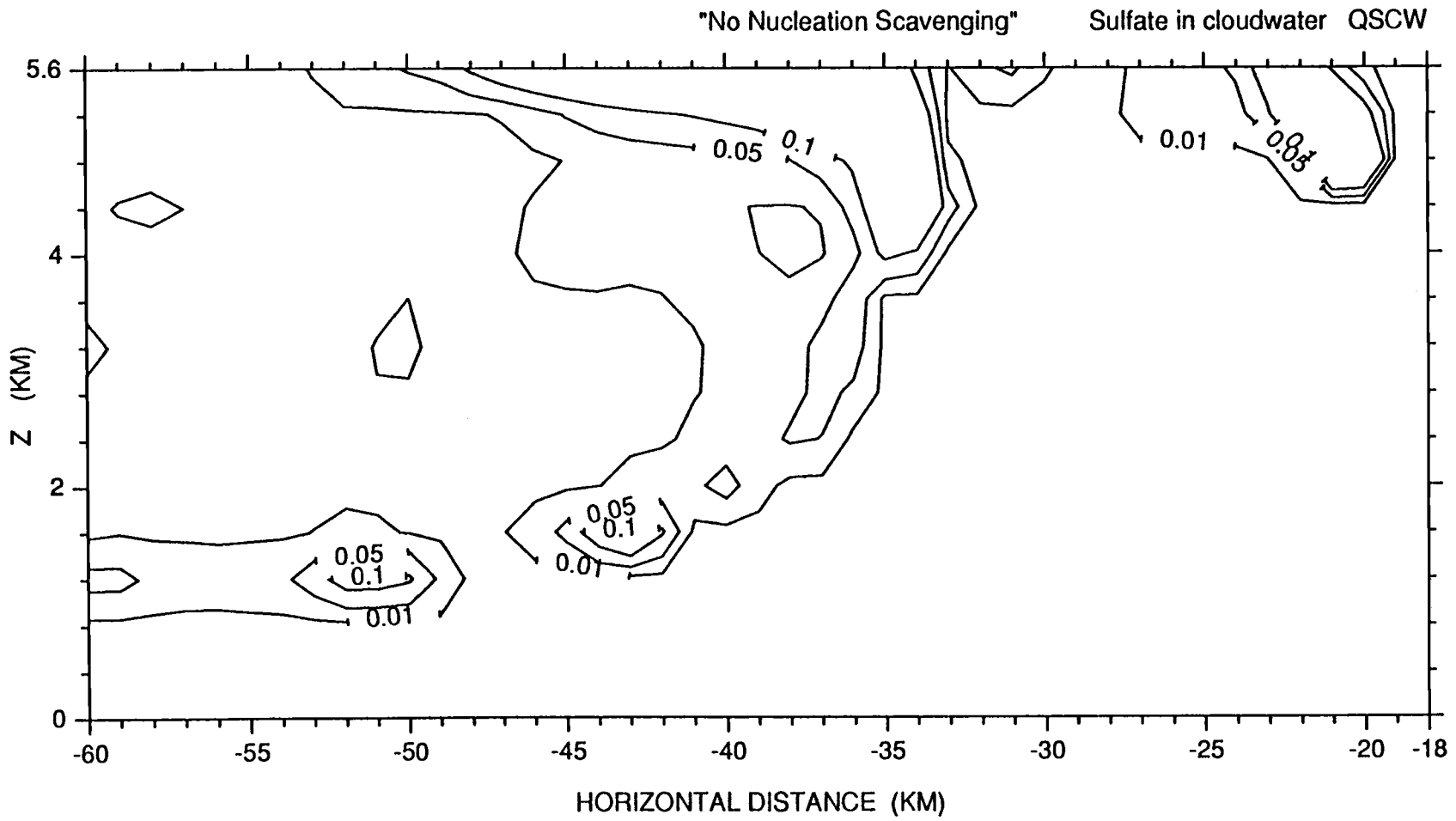

Fig. 6.20 Mixing ratio of sulfate-in-cloudwater for the case 5 simulation. Units are 10^{-9}g g^{-1}.

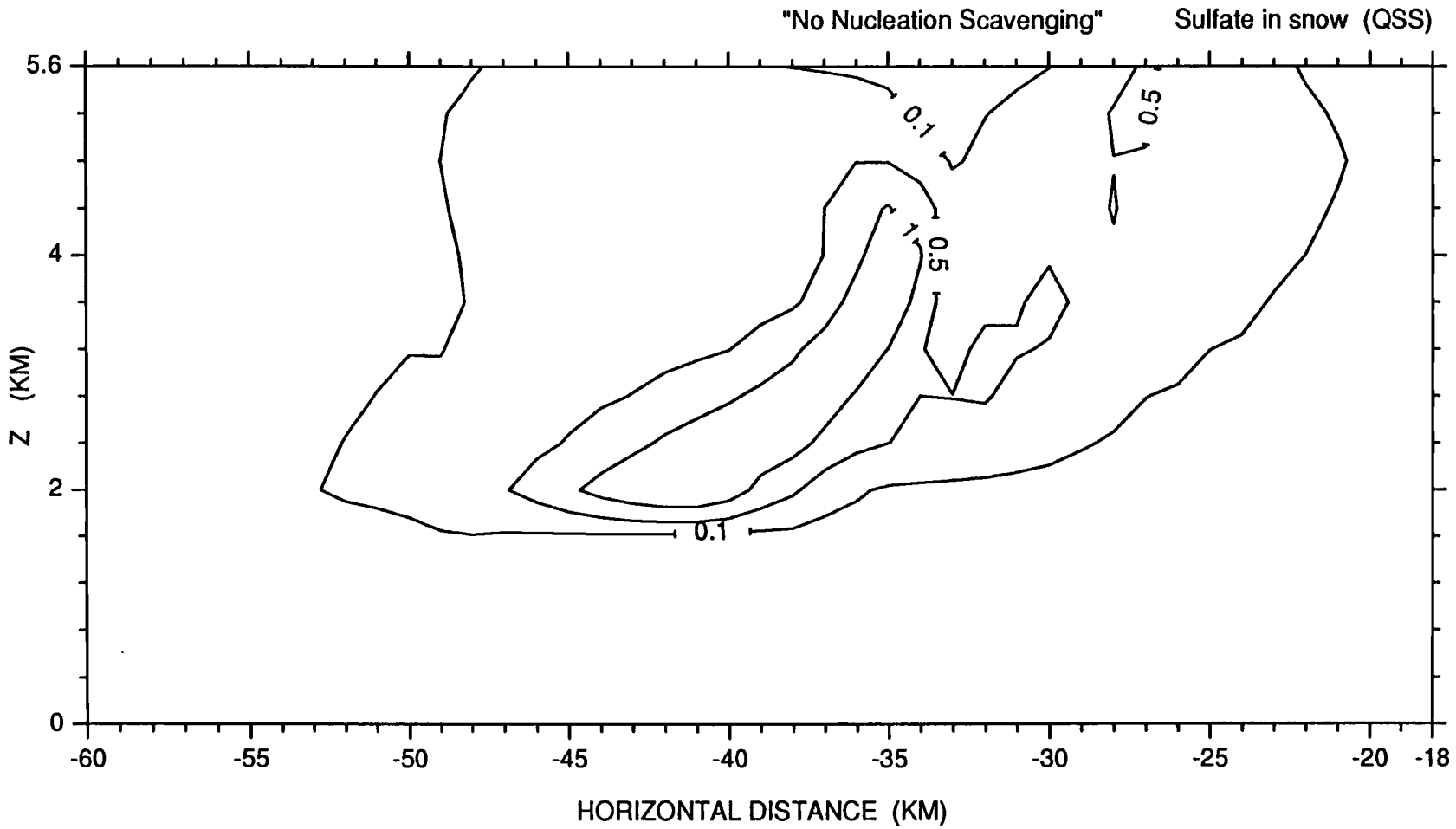

Fig. 6.21 Mixing ratio of sulfate-in-snow for the case 5 simulation. Units are 10^{-9}g g^{-1}.

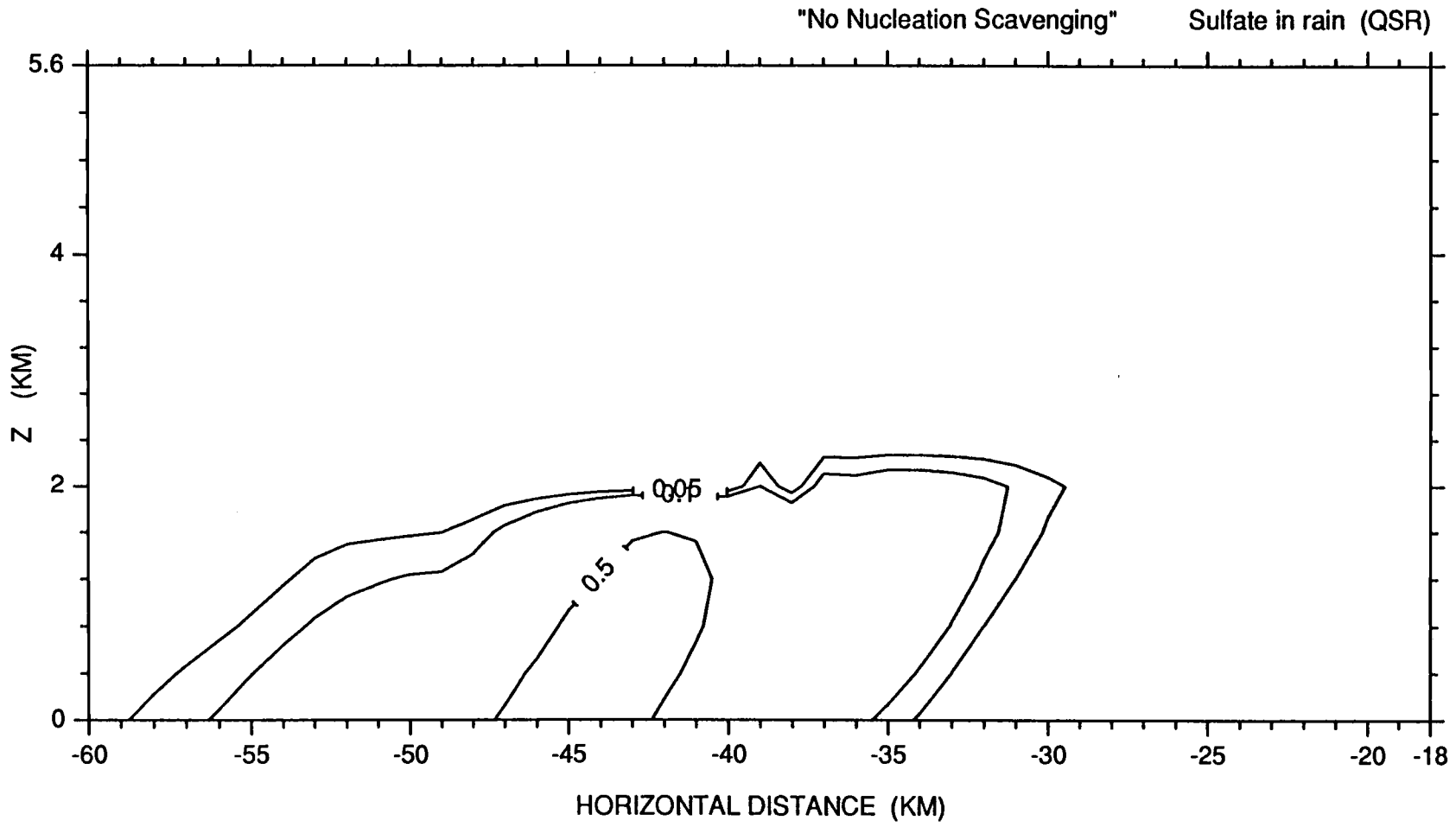

Fig. 6.22 Mixing ratio of sulfate-in-rain for the case 5 simulation. Units are 10^{-9}g g^{-1}.

important are the changes each of the cases has on sulfate deposition rates. These are calculated as before and the results for all 5 simulations are shown in Fig. 6.23. Oxidation, primarily by H_2O_2, is seen to have the greatest effect on sulfate deposition. While these rates are not strictly additive (i.e. case 4 + case 5 ≠ case 1), they are close enough (within 4%) for computational purposes. (Nor should they be expected to be additive, i.e. nucleation scavenging introduces greater acidity into the cloud thereby limiting oxidation which takes place in its absence).

An average deposition rate was calculated for each case to determine the net effect on total sulfate deposition. Nucleation scavenging was responsible for ~33% of the total sulfate deposition. This leaves ~67% of the sulfate deposition to oxidation, which was partitioned into ~53% due to H_2O_2 oxidation and ~14% due to oxidation by ozone. The surprising aspect of this result is that the sulfate-in-snow and sulfate-in-cloudwater were lowest for the case 5 study (in which nucleation scavenging was turned off). The rainfall at the surface was largely generated by the melting of snow, hence the expectation that nucleation scavenging would be more important in terms of total sulfate deposition. However, the oxidation of SO_2 that occurred in rain was more substantial than that in cloudwater (by virtue of the low cloudwater contents). This result runs contrary to previous studies (e.g. Chamberlain *et al.* 1985) in which oxidation in rain is of little significance because the fallspeeds of the raindrops prevent extended reaction time prior to deposition.

These sensitivity studies have shown that in-solution oxidation of SO_2 by H_2O_2 was the major factor influencing the deposition of sulfate. The net upward vertical redistribution of SO_2 is attributable to both oxidation and

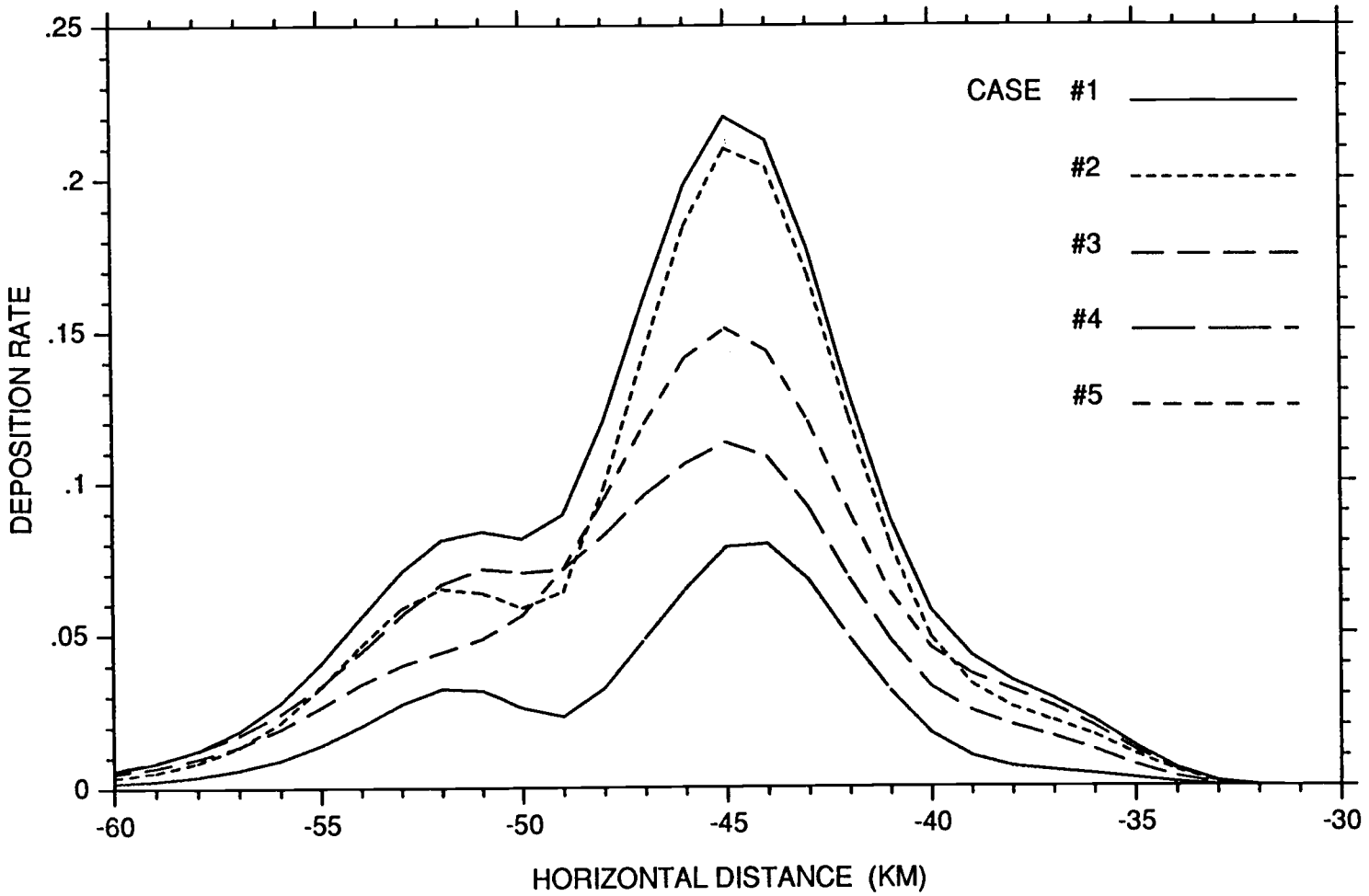

Fig. 6.23 Sulfate deposition rates for the 5 simulations. Units are g $cm^{-1}hr^{-1}$.

nucleation scavenging, which kept the cloudwater pH too low to allow further absorption of SO_2. Another insight the sensitivity studies give, albeit indirectly, was the effect of the low cloudwater contents. If cloudwater contents were an order of magnitude larger (not unreasonable) oxidation of SO_2 would substantially increase (because the cloudwater would not acidify as quickly) and nucleation scavenging would take place more uniformly along the leading edge of the cloudwater field. This scenario will be discussed further in the next section.

6.2 Comparison of model results to observations

Comparison of model results to observations have been delayed in order to discuss the limitations of both the model and the GALE project. Ideally this study would have been able to make direct, one-to-one comparisons of model outputs to field observations; thus validating, and/or exposing the inaccuracies of the model output, so that further refinement of the chemical and microphysical parameterizations could be made. The reality of the situation is, alas, quite different. In keeping with the rest of this thesis, comparisons to observations of the microphysical model outputs will be made first, followed by comparisons of the model-generated chemical fields to the observations.

6.2.1 Microphysical comparisons

The model output precipitation rate at the surface of 3.4 mm hr^{-1} (averaged over 30 km) corresponded well to the available surface measurements. One location reported a one hour average of 2.8 mm hr^{-1}. Another site reported a peak 15 minute average of 3.8 mm hr^{-1} ; this

corresponds to 13.5 km of model rainfall in which the average precipitation rate was 5.8 mm hr^{-1}. Although the model predicted rainfall is greater than the observations it is easily within reason. Of more concern, however, is the location of the precipitation as determined by comparing the model output reflectivity (cf. Fig. 5.5) and the observed reflectivity (cf. Fig. 4.3). The bright band from the model is located at a height of 2 km and centered between x=-47 and x=-39. The observed reflectivity shows the bright band at the 1.6 km level between x=-34 and x=-26. These discrepancies can be explained as follows. First of all, the Wilmington sounding may not have been an accurate representation of the pre-band environment in that the freezing level was 400 m higher than Fig. 4.3 indicates. Also, accompanying the upper-level cold front was drier air, which affected the precipitation growth mechanisms, but was not included in the model simulation. As to the precipitation difference, by examining Fig. 4.3 it is obvious that there is ice and snow generation prior to the leading edge of the model domain. This suggests that the upper-level generating cell in the model (cf. Fig. 5.2) may not mark the leading edge of the snow production region. If this is the case, an obvious shift in the precipitation maximum would occur. The model generated reflectivites have much higher values due to the excessive snow quantities. This is a result of the fact that the first generating cell was located very near to the CP-3 radar. For dual-Doppler analysis to be effective the observation area must be at least 20 km away from both radars. There are indications that the updrafts in the first cell (which was in an area of poor data converge) are much too strong. The model results discussed in Chapter 5 show very little cloudwater due to the strong ice-particle growth associated with the first cell. The University of Washington's C131

aircraft measurements of cloudwater are on the order of .5 to 1.2 g kg^{-1}, an order of magnitude higher than model predictions. Another important aspect of the rainband was its strongly three-dimensional structure; precipitation at the surface was highly variable in both intensity and quantity, and radar echoes indicated localized convective activity within the rainband. The assumption of two-dimensionality, valid for wide cold-frontal and stratiform precipitation, appears not to be entirely accurate.

Certainly, the gross features of the rainband were simulated properly, especially in terms of condensate produced (although partitioned disproportionally in cloudwater and snow), but the ideal of direct comparisons with *in situ* observations is, unfortunately, not available.

6.2.2 Chemistry comparisons

The chemistry data obtained in this experiment was limited to that collected by the University of Washington's C131 aircraft. The flight path covered approximately 10 km in width, located between x=-51 and x=-41 on the horizontal axis, and 3 km in height with the lowest measurements taken at 1 km above the surface.

Shown in Fig. 6.24 is the comparison of measured and model-predicted SO_2. The lowest measurement is that of the pre-band environment and it determined the initial profile used in the simulation. The middle measurements are slightly lower than predicted by the model, due to the low cloudwater contents of the simulation which slowed dissolution. However, the model results are within the experimental error of the measurements. The model average between x=-41 and x=-51 (broadly dashed line) gives a better

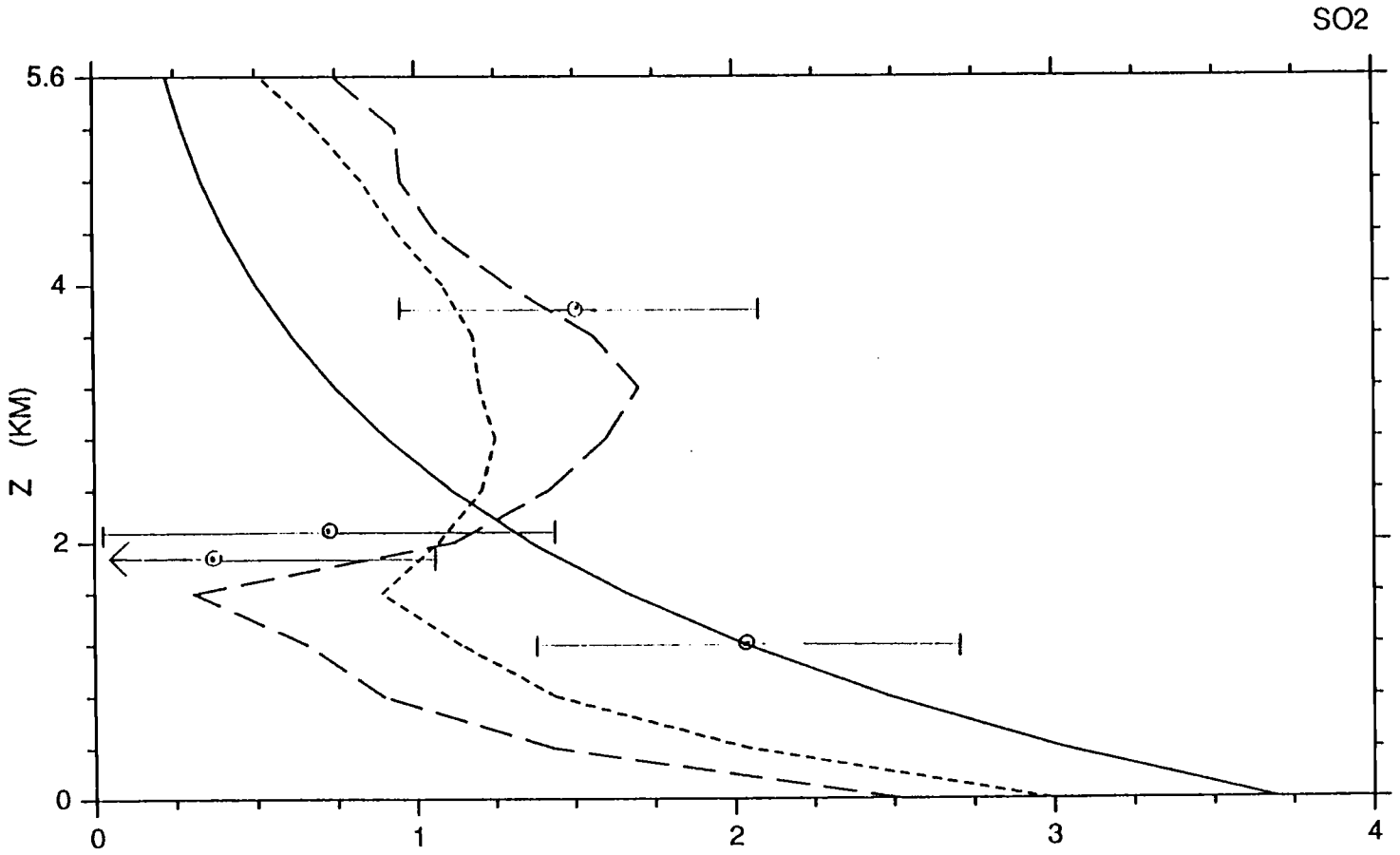

Fig. 6.24 Comparison of *in situ* measurements of SO_2 to model results. Solid line is the initial SO_2 profile, thinly dashed line is model domain average, broadly dashed line is the model 10 km average. Measurements are denoted with circles and error bars. Units are 10^{-9}g g^{-1}.

agreement than the entire model domain average. The upper-level measurement compares favorably with the model result. Fig. 6.25 shows the comparison of measured and model-predicted sulfate. The model's 10 km average predictions are in very good agreement with observations. The fact that the 10 km average does consistently better than the entire domain average is encouraging. However, because the cloud microphysics may be inaccurate, the favorable comparisons are viewed with guarded optimism.The similar measured vs. model-predicted comparison for nitrate is shown in Fig. 6.26. Here the model seriously underpredicts the nitrate concentrations. This is a result of the lack of nitrate production in the model. However, another factor may be partially responsible, that of no initial HNO_3 in the pre-band environment. There is concern that the air sampled prior to the band had already been affected by the band to some extent (perhaps associated with upper level subsidence extending downward from upper-levels of the band's leading edge). HNO_3 is very rapidly incorporated into all hydrometeors, and by its absence a potentially significant source of nitrate may have been missing from the simulation.

These shortcomings are emphasized not to vindicate the model results but to demonstrate the enormous complexity of coordinating and executing such a field experiment. The most important goal of this study (from the modeler's standpoint) was to validate the chemical and microphysical parameterizations of the model. For modeling studies of this type to be useful such validation is mandatory. Ideally, the data set for this type of study would have measurements (both chemical and microphysical) from several aircraft that made simultaneous cloud penetrations at varying heights through the

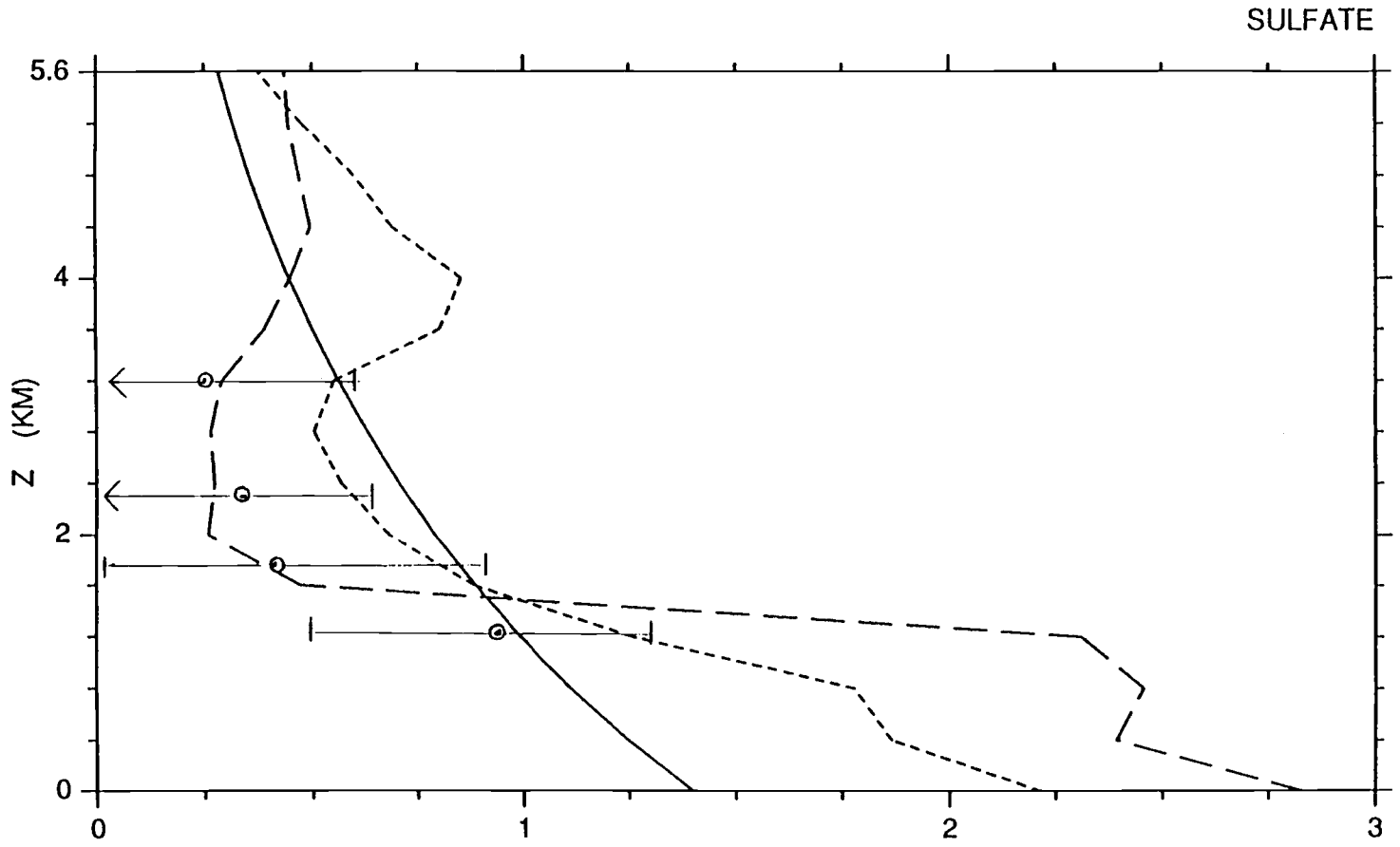

Fig. 6.25 Comparison of *in situ* measurements of sulfate to model results. Solid line is the initial sulfate profile, thinly dashed line is model domain average, broadly dashed line is the model 10 km average. Measurements are denoted with circles and error bars. Units are 10^{-9}g g^{-1}.

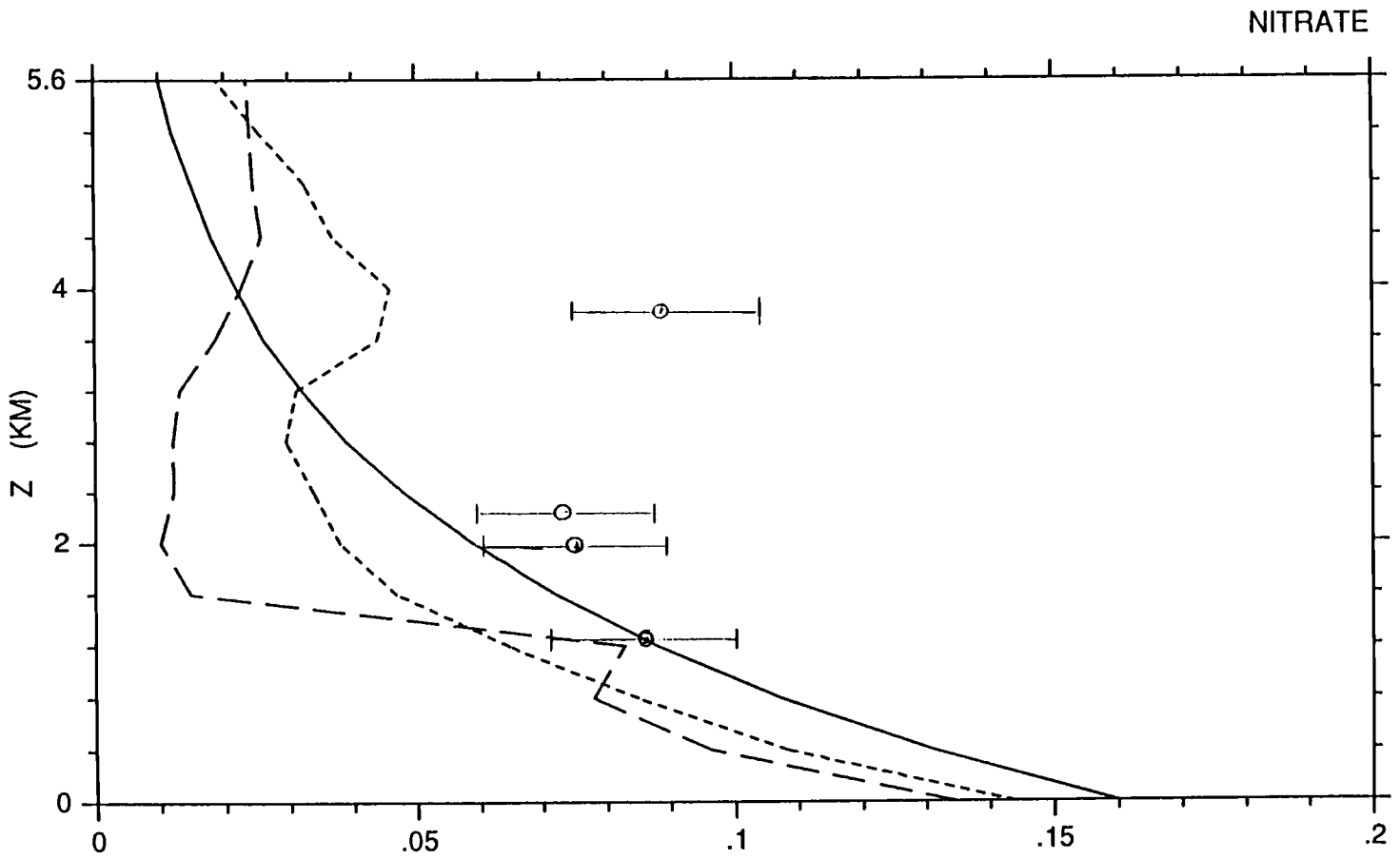

Fig. 6.26 Comparison of *in situ* measurements of nitrate to model results. Solid line is the initial nitrate profile, thinly dashed line is model domain average, broadly dashed line is the model 10 km average. Measurements are denoted with circles and error bars. Units are 10^{-9}g g^{-1}.

pre-band, in-band, and post-band environments.

7. CONCLUSIONS

7.1 Conclusions and Model Evaluation

In this thesis a diagnostic modeling study of the cloud and cloud chemistry processes in a wide cold-frontal rainband, observed during the GALE project on 6 March 1986, has been described.

The precipitation growth mechanism was similar to the seeder-feeder process except that the feeder zone was not well defined. Strong ice particle generation aloft was responsible for the large snow content produced by the model. Snow grew primarily by vapor deposition, but riming growth was also important. The melting of snow produced an average rainfall rate at the surface of 3.4 mm h^{-1}, which corresponded well to available observations. The low cloudwater contents (~.01-.1g kg^{-1}) of the simulation were a result of the excessive generation of ice particles.

The model results indicate that oxidation of SO_2 by H_2O_2 was responsible for ~53% of the total sulfate deposition. Nucleation scavenging contributed ~33% and oxidation of SO_2 by ozone produced ~14% of the total sulfate deposited. Ozone oxidation was important in regions of the cloud where peroxide had been previously removed (through absorbtion into the liquid water fields and oxidation of SO_2). The small amounts of cloudwater enabled rain to be the dominant hydrometeor in which oxidation of SO_2 occurred. Nitrate was only affected by microphysical processes as a result of insignificant dissolution of PAN and the lack of initial gas-phase HNO_3.

Because of the discrepancies between observations and model inputs, the model results cannot be unequivocably compared with *in situ* and surface measurements. The model's underprediction of cloudwater, perhaps not

significant in terms of surface precipitation, had a profound impact on the cloud chemistry. The limited cloudwater produced acidified rapidly, thereby preventing further dissolution of SO_2. The model's 10 km average profiles (corresponding to the C131 aircraft's data acquisition area) of SO_2 and sulfate agreed well with the *in situ* measurements. However, because of the inaccuracies in the microphysical simulation (a consequence of the model inputs and not the model itself), the agreements between model results and observations may be fortuitous. In total, definitive verification of the model parameterizations is not possible.

This summary shows that conducting a cloud chemistry field experiment as a piggyback project may not provide enough chemistry data. The spatial and temporal changes of microphysical and chemical variables that can occur during a precipitation event prevent only one aircraft from acquiring sufficient *in situ* measurements. The result is an incomplete data set which, when used for comparative purposes, can lead to ambiguous conclusions. For this experiment, surface chemistry data is not available (at this time), which could be very useful for verifying the chemical species deposition rates calculated by the model.

7.2 Suggestions for further research

The most obvious need for the chemistry component of the model is an in-cloud nitrate production mechansim. The most likely production mechansim involves the reaction of gaseous NO_2 with ozone in the interstitial air. This reaction forms highly soluble N_2O_5 which is rapidly converted to nitric acid in cloudwater (Heikes and Thompson, 1983). Another improvement for the

chemistry would be to include the size spectra for particulate sulfate and nitrate. Nucleation scavenging would be better represented in such an instance.

Related to the idea of using the size spectra for sulfate and nitrate is to convert the model to include explicit microphysics. The individual size catagories in an explicit model would more accurately simulate both the chemistry and microphysics of the cloud. However, if parameterized microphysics are to be retained stochastic processes could be introduced to more accurately represent precipitation growth.

REFERENCES

Barrie, L.A., 1985: Scavenging ratios, wet deposition, and in-cloud oxidation: An application to the oxides of sulfur and nitrogen. *J. Geophys. Res.*, **90**, 5789-5799.

Browning, K.A., F.F. Hill, and C.W. Pardoe, 1974: Structure and mechanism of precipitation and the effect of orography in a wintertime warm sector. *Quart. J. Roy. Meteor. Soc.*, **100**, 309-330.

Browning, K.A., and G.A. Monk, 1982: A simple model for the synoptic analysis of cold fronts. *Quart. J. Roy. Meteor. Soc.*, **108**, 435-452.

Chamberlain, J., H. Foley, D. Hammer, G. MacDonald, S. Matarazza, O. Rothaus, and M. Ruderman, 1985. *Acid Deposition.* Jason, 452 pp.

Chaumerliac, N., E. Richard, J.-P. Pinty, and E.C. Nickerson, 1987: Sulfur scavenging in a mesoscale model with quasi-spectral microphysics: Two-dimensional results for continental and maritime clouds. *J. Geophys. Res.*, **92**, 3114-3126.

Chang, T.Y., 1984: Rain and snow scavenging of HNO_3 vapor in the atmosphere. *Atmos. Environ.*, **18**, 191-197.

Daum, P.H., T.J. Kelly, S.E. Schwartz, and L. Newman, 1984: Measurements of the chemical composition of stratiform clouds. *Atmos. Environ.*, **18**, 2671-2684.

GALE Project Office 1985, *Genesis of Atlantic Lows Experiment (GALE): Experimental Design*, NCAR Boulder, CO, USA.

Hegg, D.A., P.V. Hobbs, and L.F. Radke, 1984a: Measurements of the scavenging of sulfate and nitrate in clouds. *Atmos. Environ.*, **18**, 1939-1946.

Hegg, D.A., S.A. Rutledge, and P.V. Hobbs, 1984b: A numerical model for sulfur chemistry in warm-frontal rainbands. *J. Geophys. Res.*, **89**, 7133-7147.

Hegg, D.A., S.A. Rutledge, and P.V. Hobbs, 1986: A numerical model for sulfur and nitrogen scavenging in narrow cold-frontal rainbands, 2, Discussion of chemical fields. *J. Geophys. Res.*, **91**, 14,403-14,416.

Heikes, B.G., and A.M. Thompson, 1983: Effects of heterogeneous processes on NO_3, HONO, and HNO_3 chemistry in the troposphere. *J. Geophys. Res.*, **88**, 10,883-10,895.

Herzegh, P.H., and P.V. Hobbs, 1980: The mesoscale and microscale structure and organization of clouds and precipitation in extratropical cyclones. II: Warm-frontal clouds. *J. Atmos. Sci.*, **37**, 597-611.

Herzegh, P.H., and P.V. Hobbs, 1980: The mesoscale and microscale structure and organization of clouds and precipitation in extratropical cyclones. IV: Vertical air motions and microphysical structures of prefrontal surge clouds and cold-frontal clouds. *J. Atmos. Sci.*, **38**, 1771-1784.

Hobbs, P.V., 1987: An illustrative example of the nowcasting challenge. *Proceedings of Symposium on* "Mesoscale Analysis and Forecasting", XIX General Assembly IUGG, Vancouver, Canada.

Hobbs, P.V., T.J. Matejka, P.H. Herzegh, J.D. Locatelli and R.A. Houze, Jr., 1980: The mesoscale and microscale structure and organization of clouds and precipitation in mid-latitude cyclones. Part I: A case study of a cold front. *J. Atmos. Sci.*, **37**, 568-596.

Holdren, M.W., C.W. Spicer, and J.M. Hales, 1984: Peroxyacetyl nitrate solubility and decomposition rate in acidic water. *Atmos. Environ.*, **18**, 1171-1173.

Houze, R.A., Jr., and P.V. Hobbs, 1982: Organization and structure of precipitating cloud systems. *Adv. in Geophys.*, **24**, 225-315.

Houze, R.A., Jr., S.A. Rutledge, T.J. Matejka, and P.V. Hobbs, 1981: The mesoscale and microscale structure and organization of clouds and precipitation in extratropical cyclones. III: Air motions and precipitation growth in a warm-frontal rainband. *J. Atmos. Sci.*, **38**, 639-649.

Huebert, B.J., and A.L. Lazrus, 1980: Tropospheric gas-phase and particulate nitrate measurements. *J. Geophys. Res.*, **85**, 7322-7328.

Huebert, B.J., F.C. Fehsenfeld, R.B. Norton, and D. Albritton, 1983: The scavenging of nitric acid vapor by snow. *Precipitation Scavenging, Dry-Deposition and Resuspension.* H.R. Pruppacher, R.G. Semonin and W.G.N. Slinn, editors., Elsevier, 293-300.

Lee, I.Y., and J.D. Shannon, 1985: Indications of nonlinearities in processes of wet deposition. *Atmos. Environ.*, **19**, 143-149.

Levine, S.Z., and S.E. Schwartz, 1982: In-cloud and below-cloud scavenging of nitric acid vapor. *Atmos. Environ.*, **16**, 1725-1734.

Locatelli, J.D., J.M. Sienkiewicz, and P.V. Hobbs, 1987: The organization and structure of clouds and precipitation in winter on the mid-Atlantic coast of the United States, I: An occluded system. *J. Atmos. Sci.*, (to be submitted).

Marshall, J.S., and W.M. Palmer, 1948: The distribution of raindrop with size. *J. Meteor.*, **5**, 165-166.

Martin, L.R., and D.E. Damschen, 1981: Aqueous oxidation of sulfur dioxide by hydrogen peroxide at low pH. *Atmos. Environ.*, **15**, 1615-1621.

Matejka, T.J., R.A. Houze, Jr., and P.V. Hobbs, 1980: Microphysics and dynamics of clouds associated with mesoscale rainbands in extratropical cyclones. *Quart. J. Meteor. Soc.*, **106**, 29-56.

Radke, L.F., P.V. Hobbs, and M.W. Eltgroth, 1980: Scavenging of aerosol particles by precipitation. *J. Appl. Meteor.*, **19**, 715-722.

Rutledge, S.A., 1983: A Numerical Model of Cloud and Precipitation Processes in Mesoscale Rainbands. Ph.D. Thesis, University of Washington, 220 pp.

Rutledge, S.A., and P.V. Hobbs, 1983: The mesoscale and microscale structure and organization of clouds and precipitation in midlatitude cyclones. VIII: A model for "seeder-feeder" process in warm-frontal rainbands. *J. Atmos. Sci.*, **40**, 1185-1206.

Rutledge, S.A., and P.V. Hobbs, 1984: The mesoscale and microscale structure and organization of clouds and precipitation in midlatitude cyclones. XII: A diagnostic modeling study of precipitation development in narrow cold-frontal rainbands. *J. Atmos. Sci.*, **41**, 2942-2972.

Rutledge, S.A., D.A. Hegg, and P.V. Hobbs, 1986: A numerical model for sulfur and nitrogen scavenging in narrow cold-frontal rainbands, 1, Model description and discussion of microphysical fields. *J. Geophys. Res.*, **91**, 14,385-14,402.

Scott, B.C., 1978: Parameterization of sulfate removal by precipitation. *J. Appl. Meteor.*, **17**, 1375-1389.

Scott, B.C., 1982: Predictions of in-cloud conversion rates of SO_2 to SO_4 based upon a simple chemical and kinematic storm model. *Atmos. Environ.*, **16**, 1735-1752.

Sperber, K.R., and S. Hameed, 1986: Rate of precipitation scavenging of nitrates on Central Long Island. *J. Geo. Res.*, **91**, 11,833-11,839.

Tremblay, A., and H. Leighton, 1985: A three-dimensional cloud chemistry model. *J. Climate Appl. Meteor.*, **25**, 652-671.

Tremblay, A., and H. Leighton, 1984: The influence of cloud dynamics upon the redistribution and transformation of atmospheric SO_2 -- A numerical simulation. *Atmos. Environ.*, **18**, 1885-1894.